

UC Davis

UC Davis Electronic Theses and Dissertations

Title

An Investigation of Rotational and Vibrational Spectra of Radicals Using Ab Initio Quantum Mechanical Methods and Chirped-Pulse Fourier Transform Microwave Spectroscopy

Permalink

<https://escholarship.org/uc/item/80f7469x>

Author

Meyer, Kelly Suzanne

Publication Date

2022

Peer reviewed|Thesis/dissertation

An Investigation of Rotational and Vibrational Spectra of Radicals Using
Ab Initio Quantum Mechanical Methods and Chirped-Pulse Fourier
Transform Microwave Spectroscopy

By

KELLY SUZANNE MEYER
DISSERTATION

Submitted in partial satisfaction of the requirements for the degree of

DOCTOR OF PHILOSOPHY

in

Chemistry

in the

OFFICE OF GRADUATE STUDIES

of the

UNIVERSITY OF CALIFORNIA

DAVIS

Approved:

Kyle N. Crabtree, Chair

Dean J. Tantillo

Matthew Augustine

Committee in Charge

2022

Copyright © 2022 by
Kelly Suzanne Meyer
All rights reserved.

CONTENTS

List of Figures	v
List of Tables	vii
Abstract	viii
Acknowledgments	x
1 Introduction	1
1.1 Astrochemistry	1
1.1.1 The Interstellar Medium	1
1.1.2 Radical-Driven Chemistry in the Interstellar Medium	2
1.1.3 Unidentified Infrared (UIR) Emission Bands	5
1.1.4 Meteorites	5
1.2 Ab Initio Quantum Chemical Methods for High-Resolution Spectroscopy . .	6
1.3 Experimental Rotational Spectroscopy	8
2 Spectroscopic Characterization of Radicals Using Ab Initio Methods	10
2.1 Introduction	10
2.2 The Molecular Hamiltonian	11
2.3 Coupled Cluster Method	13
2.4 Watson's Nuclear Hamiltonian	15
2.4.1 The Rigid Rotor Hamiltonian	20
2.4.2 Rotational Selection Rules	22
2.4.3 Centrifugal Distortion	22
2.4.4 Angular Momentum Coupling	24
2.4.4.1 Hyperfine Interactions	25
2.4.4.1.1 Nuclear Quadrupole Interaction	25
2.4.4.1.2 Electron Nuclear Spin-Spin Interactions and Fermi Contact Terms	25

2.4.4.2	Spin-Rotation Interaction	26
2.5	Vibrational Energy Levels	26
2.6	Conclusion	29
3	Rotational and Vibrational Spectra of the Pyridyl Radicals: A Coupled-Cluster Study	31
3.1	Abstract	31
3.2	Introduction	33
3.3	Methods	35
3.4	Results and Discussion	36
3.4.1	Ground State Energies and Optimized Geometries	36
3.4.2	Spectroscopic Parameters	37
3.4.2.1	Rotational Constants and Vibration-Rotation Interactions	37
3.4.2.2	Spectroscopic Parameters for Rotational and Rovibrational Spectroscopy	37
3.5	Simulated Rotational Spectra	42
3.6	Vibrational Analysis	45
3.7	Conclusion	55
3.8	Supporting Information	56
4	Chirped-pulse Fourier Transform Microwave Spectroscopy (CP-FTMW)	57
4.1	Chirp Generation	57
4.2	Polarization of Molecular Sample and FID Collection	58
4.3	FID Detection	60
4.4	Molecular Sample	61
4.5	Sources of Spectral Line Broadening	62
4.5.1	Natural Linewidth	62
4.5.2	Pressure Broadening	64
4.5.3	Doppler Broadening	64

4.6	Conclusion	65
5	Segmented CP-FTMW Spectroscopy with Direct Digital Synthesis (DDS) Technology	67
5.1	Introduction	67
5.2	Technical Specifications	68
5.3	Results	72
5.4	Conclusion	73
6	Optimization of a Custom Built Ka-band Chirped-Pulse Fourier Transform Microwave (CP-FTMW) Spectrometer	74
6.1	Introduction	74
6.2	Ka-band CP-FTMW Spectrometer	75
6.3	Experimental Setup	77
6.3.1	Sample Preparation	77
6.3.1.1	Pyridine	77
6.3.1.2	Acrylonitrile	77
6.3.2	Piezoelectric Pulsed Valve	77
6.3.3	Plasma Discharge Chemistry	79
6.4	Signal Intensity Levels	82
6.5	Results	83
6.6	Conclusion	87
A	Rotational and Vibrational Spectra of the Pyridyl Radicals: A Coupled-Cluster Study Supporting Information	89

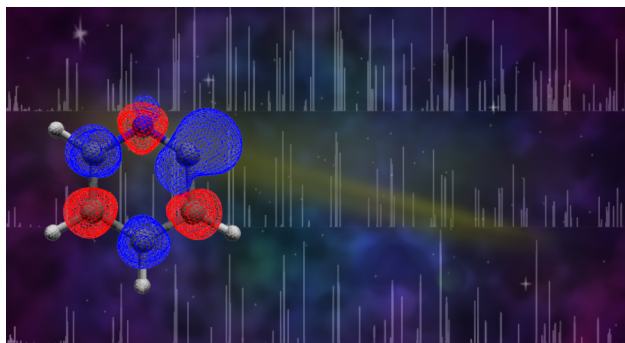
LIST OF FIGURES

1.1	Calculated Barrierless Reaction	4
1.2	Molecular Detections on the Murchison Meteorite	6
1.3	Known Rotational Transition Frequencies from Splatalogue	7
2.1	Coupled-cluster Excitation Diagram	14
2.2	Eckart Frame	16
2.3	Principal Axis System	18
2.4	Fundamental Rotational Transitions Ladder Diagram	23
2.5	Angular Momentum Coupling Cartoon	24
2.6	VPT2 and VPT2+K Comparison Plots for Pyridyl	30
3.1	Simulated Rotational Spectra for 2-, 3-, and 4-pyridyl	44
3.2	Simulated Fundamental Transitions for 2-, 3-, and 4-pyridyl	45
3.3	Simulated Hyperfine Structure for 2-, 3-, and 4-pyridyl	46
3.4	Simulated VPT2+K IR Spectra for 2-, 3-, and 4-pyridyl	51
3.5	VPT2+K Comparisons for 2-, 3-, and 4-pyridyl	52
4.1	CP-FTMW Spectrometer Schematic	58
4.2	T_2 Relaxation Process Diagram	59
4.3	Gaussian and Lorentzian Lineshape Functions	63
5.1	Segmented CP-FTMW Spectrometer Schematic	68
5.2	DDS Triggering Timings	70
5.3	Block Diagram of DDS	70
5.4	1 GHz Chirp from DDS Circuit	71
5.5	Phase Instability of Chirp	72
5.6	Chirp Power from 9-10 GHz	73

6.1	Ka-band CP-FTMW Spectrometer Schematic	75
6.2	Time and Frequency Domain Plots for Microwave Chirp	76
6.3	Piezoelectric Pulsed Valve	78
6.4	AWG Trigger Timing Relative to Gas Pulse	78
6.5	Discharge Stack Apparatus	79
6.6	Acrylonitrile Discharge Spectrum	80
6.7	Pyridine Discharge Spectrum	81
6.8	Discharge Voltage Comparisons	81
6.9	Chirp Power	82
6.10	Gas Pulse Width Comparisons: Acrylonitrile	83
6.11	Ka-band CP-FTMW Spectrum of Pyridine and Acrylonitrile	84
6.12	Pyridine Discharge Spectra	84
A.1	Hyperfine Structure for 2-pyridyl – a-type spectrum	100
A.2	Hyperfine Structure for 2-pyridyl – b-type spectrum	101
A.3	Hyperfine Structure for 3-pyridyl – a-type spectrum	102
A.4	Hyperfine Structure for 3-pyridyl – b-type spectrum	103
A.5	Hyperfine Structure for 4-pyridyl – b-type spectrum	104

LIST OF TABLES

2.1	Selection Rules	22
3.1	Equilibrium Geometries for 2-, 3-, and 4-pyridyl	38
3.2	Equilibrium Parameters for 2-, 3-, and 4-pyridyl	39
3.3	Ground State Parameters for 2-, 3-, and 4-pyridyl	40
3.4	Fermi Contact Terms for 2-, 3-, and 4-pyridyl	41
3.5	Spin Densities for 2-, 3-, and 4-pyridyl	42
3.6	Vibrational Frequencies and Intensities for 2-pyridyl	48
3.7	Vibrational Frequencies and Intensities for 3-pyridyl	49
3.8	Vibrational Frequencies and Intensities for 4-pyridyl	50
5.1	DDS Registers	71
6.1	Pyridine Rotational Transitions	85
6.2	Pyridine Discharge Rotational Transitions	86
6.3	Spectroscopic Parameters for Pyridine	87
A.1	Output Files	90
A.2	Output Files	91
A.3	Spin-Spin Tensors	92
A.4	Nitrogen Quadrupole Tensors	93
A.5	Spin-Rotation Tensors	93
A.6	Harmonic Vibrational Frequencies: 2-pyridyl	94
A.7	Harmonic Vibrational Frequencies: 3-pyridyl	95
A.8	Harmonic Vibrational Frequencies: 4-pyridyl	96
A.9	Combination & Overtone Bands: 2-pyridyl	97
A.10	Combination & Overtone Bands: 3-pyridyl	98
A.11	Combination & Overtone Bands: 4-pyridyl	99



ABSTRACT

Astrochemistry relies heavily on rotational and vibrational spectroscopy to study the chemical kinetics and dynamics of reactions in space and to determine the exact structure of astrochemically relevant molecules. Recent advances in spectroscopic tools, along with technological breakthroughs from powerful radio telescopes around the world, have enabled a deeper understanding of the complex chemistry of space. Even though interstellar space appears to be dark and empty, it contains a wide variety of molecular species; however, the mechanisms involved in producing these species remain unclear.

There have been approximately 270 unique molecular detections in the interstellar medium (ISM) and approximately 20% are radicals. It has been suggested that radical-neutral reactions play an important role in the formation of molecules in the ISM. These types of reactions are sometimes associated with gas-phase barrierless reaction pathways, which are suited for low temperature regions of the ISM (e.g., cold molecular clouds like TMC-1). Several polycyclic aromatic hydrocarbons and their nitrogen substituted derivatives (PAH/PANH) have been detected in chondritic meteorites and their synthesis may have origins in the low temperature regions of space via radical-mediated gas-grain reactions before accretion to the meteorite parent body. Based on the molecule's non-terrestrial isotopic ratios, they are thought to have extraterrestrial origins, yet their formation mechanism is unknown. Our understanding of how complex chemical reactions operate in space is improving, and the likelihood of radicals being involved is high, but it still remains unclear how these reactions are carried out.

To improve chemical models of astronomical environments, experimental data, including accurate rate constants, branching ratios, and structural information, is essential. It is generally possible to determine the input parameters for these astrochemical models by using experimental rotational/vibrational spectroscopic methods in conjunction with theory. Chapter 2 of this dissertation describes the coupled-cluster method, along with a detailed discussion of the calculations necessary for rotational and vibrational spectroscopy. Chapter 3 applies this theoretical method to the pyridyl radicals, which are of interest due to their structural similarity to prebiotic molecules and their possible role as precursors to PANHs.

High-level computational results also assist experimental studies. Two instruments capable of measuring microwave spectra of radicals were custom-built and tested: a segmented chirped-pulse Fourier transform microwave (CP-FTMW) spectrometer and a Ka-band CP-FTMW spectrometer. An overview of the instrumentation theory is presented in Chapter 4, and the optimizations/preliminary results for both instruments are presented in Chapters 5 and 6, respectively. It is expected that future developments will include the measurement of more radicals, thus broadening the chemical applications of these instruments.

ACKNOWLEDGMENTS

To my husband, Dr. David, for his love and support. There is no doubt that graduate school can take its toll on anyone. The fact that I could come home after a long day in the lab to a home-cooked dinner and a movie made all the difference. And the countless hours we spent working on our little whiteboard solving scientific/mathematical problems made all the difference. We have such an exciting future ahead of us because we are absolute bad-asses. I love you! And to Cleo, my queen, I'll always miss you. And to Jed and Penny, you make life so much more fun.

To my parents, Bill and Carol Meyer, thank you both for supporting my seemingly random career choices and continuously keeping me on my toes with questions about science and education. However, you know me too well and know that I will make this career into something very unique! During these past 5 years, I'm grateful for your patience and constant encouragement, especially when I resisted. The example you've set for me and the confidence you have in me will last a lifetime in my heart. I am sorry/not sorry that I've developed a foul mouth over the years—I guess graduate school can do that to you. :)

To my brother, Will Meyer, a fellow gamer! Thank you for your steadfast Discord messaging that got me through one-too-many difficult moments while I was troubleshooting something in the lab or frustrated over coding. You are a true artist, and while I've been pursuing science, I have been inspired by you to remain true to my artistic side as well. Being a musician is just part of your blood and I'm grateful for all of our conversations about music, Broadway, gaming, and being an artist. I see a collaboration in our future!

To my sister, Tracy Meyer, you have been both the angel and devil on my shoulders and I thank you for that. Seriously, THANK YOU. I needed that often. You are killing it in life and I'm just in awe of that. Throughout my life, you have been my cheerleader, propping me up and encouraging me to push forward despite the challenges—giving me insight and perspective into everything that I pursued. And whoa, were there challenges! I have some time now to pursue those projects we've discussed, so are you ready to get to work?

To my sister, Dr. Robin Atkinson, you inspire me to never compromise in life! I am in awe of your ability to be a kick-ass mom and doctor, who still watches silly rom-coms like we used to growing up. I really do look up to you because you are an inspiration. Thank you for always taking my call when I needed medical advice during the hardest 5 years of my life. Thank you for always supporting me!

To my lab members...I really do thank you for always having my back and rooting me on. We've had moments of celebration as well as times of great difficulty, but you all helped me get through to the other side. And I have to say that our petty differences on Slack really brightened my days. Each of you, in your own way, contributed to my completing this degree and I can't thank you all enough.

And to my PI, Kyle Crabtree, group theory is not beautiful, but I understand why you may regard it as such. I'm grateful for all of the lessons you gave me on coding and experimental work, even when I was having great difficulty with the former and frustrated over the latter! Graduate school was very difficult, but you made a little bit easier. Thanks for your support these 5 years.

Chapter 1

Introduction

Rotational and vibrational spectroscopy are important tools for astronomy and astrochemistry. Since these techniques can identify molecules based on their geometrical differences, they can provide valuable insight into the composition of space. Astronomical surveys from facilities like the Atacama Large Millimeter/sub-millimeter Array contain a number of unknown/unidentified (U) molecules, and in order to decode this information, both theoretical and experimental approaches must be considered. Ab initio quantum chemical calculations are commonly used to accurately predict and simulate spectra that can be used to guide astronomical investigations (e.g., via rotational spectroscopy). Much of this dissertation involves spectroscopic and computational investigations of radicals of astrochemical interest.

1.1 Astrochemistry

1.1.1 The Interstellar Medium

There is a rich and diverse chemistry in the space between stars despite the outward appearance that it is black and empty. This region is called the interstellar medium (ISM). Ejected mass from dying stars (e.g., carbon stars) flows into the ISM, forming diffuse/dense/dark cold molecular clouds of varying densities ($10^0 - 10^4 \text{ cm}^{-3}$) and kinetic temperatures ($T < 100 \text{ K}$).^[1] A prestellar core develops in a cloud's interior as gas and dust accumulate, increasing the density ($> 10^4 \text{ cm}^{-3}$) and lowering the kinetic temperature to as low as 6 K.^[2] At

these low temperatures, gas condenses into icy-grain mantles on the surfaces of dust grains. Further gravitational collapse provides sufficient energy to begin a warm-up phase around the core ($T > 100$ K), forming protostellar envelopes and protoplanetary discs, ushering the development of planetary bodies over time.[3]

Approximately 270 molecules have been detected in the ISM to date, primarily from rotational transitions in the centimeter, millimeter, and sub-millimeter frequency ranges.[2, 4]. The molecular composition is diverse, consisting of hydrocarbon carbon chains, aromatic molecules, metal-bearing species, ions, and of primary interest to this dissertation, radicals, all primarily composed of carbon, hydrogen, nitrogen, oxygen, and sulfur.[4] In fact, $\approx 20\%$ of the molecular detections are radicals, which are generally detected equally in carbon stars (e.g., IRC+10216) and dark infrared clouds (e.g., TMC-1), with fewer detections in diffuse clouds and star forming regions. The first molecule detected in the ISM was methylidyne (CH^\bullet), a radical carbyne.[5] It was identified in 1932 from the electronic transition, $^2\Delta \leftarrow ^2\Pi$, with radio observations reinforcing this identification much later in the 1970s.[6] As the decades passed, additional radicals were added to the growing list of detections (e.g., OH, NH, HC_7O , C_8H , MgC_4H , and so on).[7–11]. Radicals seem to be involved in much of the chemistry in the ISM. Radicals are difficult to study in the laboratory under astrophysical conditions, and due to the lack of experimental data, information regarding their chemical reactivity in the ISM remains limited.

1.1.2 Radical-Driven Chemistry in the Interstellar Medium

Complex organic molecules (COMs, carbon-bearing molecules with at least six atoms[12]) are commonly detected in a wide variety of interstellar environments.[13–15] The mechanism for COM formation, however, is still unclear. Gas-grain chemistry models (regarded as a prominent route for COM formation) require temperatures of $T > 30$ K to ensure that radicals in interstellar ice are sufficiently mobile to initiate the production of COMs.[16–18] Under this hypothesis, it is thought that COMs can not form prior to this warm-up phase of star-forming cores, but various COMs – namely dimethyl ether (CH_3OCH_3), methyl formate (CH_3OCHO), acetaldehyde (CH_3CHO), and ketene (CH_2CO) – have been detected in prestellar cores with

temperatures of < 10 K.[19, 20]. Since gas-phase COMs have been detected in these cold environments, the gas-grain model alone does not explain their presence.[19]

For gas-phase mechanisms in cold environments, radical-neutral reactions have been proposed to play an important role in the formation of COMs because those types of reaction can proceed without an activation barrier.[21–23] In some scenarios, the rates of radical-neutral reactions increase rapidly as the temperature lowers resulting in large rate coefficients even at temperatures as low as 10 K.[24, 25] Astrochemical models are lacking low temperature experimental rate coefficients/branching ratios that could help answer questions about the formation pathways for COMs in the ISM. As a result of their potential role in the synthesis of COMs, radical-driven chemistry in space has gained considerable attention over the past few decades.[26–28]

In addition to the astronomical detections discussed previously, polycyclic aromatic hydrocarbons (PAHs) and their nitrogen containing analogues (PANHs) make up 20 – 30 % of the carbon budget in the ISM.[29–32] Benzene (c-C₆H₆) (a building block to PAHs), as well as larger aromatic systems such as indene (C₉H₈) and the cyanonaphthalene (C₁₀H₇CN) isomers have been detected in cold molecular clouds and carbon-rich protoplanetary nebulae of the ISM.[33–35] However, the formation mechanism of PAHs/PANHs in the ISM remains elusive to date. Current speculation regarding the possible origin of PAH/PANHs involve a series of radical-mediated cyclization reactions (with radicals and unsaturated molecules) in the circumstellar envelope of dying carbon stars.[28, 36, 37] Radical-neutral reactions are often modeled using rate coefficients from combustion models determined at high temperatures ($T > 1500$ K). [38, 39] Many of the combustion pathways involve reactions with significant entrance barriers of about 20-30 kJ mol⁻¹, which cannot be overcome in cold environments like cold molecular clouds or prestellar cores.[40–42] However, crossed molecular beam studies complemented by electronic structure calculations have shown compelling evidence of benzene formation from single collision, barrierless radical-neutral reactions of ethynyl radicals (C₂H) with 1,3-butadiene (H₂CCHCHCH₂),



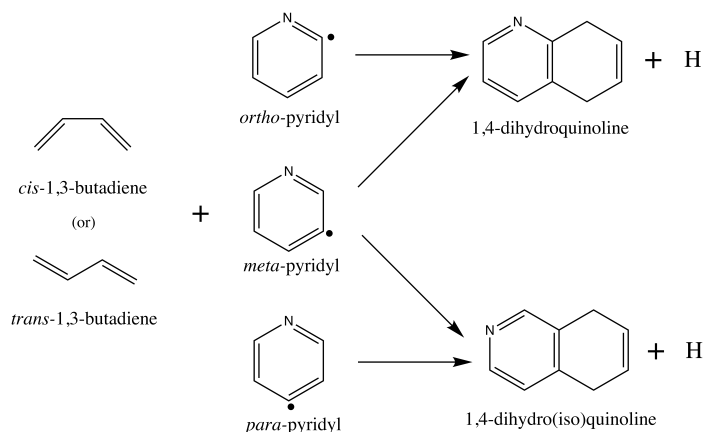


Figure 1.1: Reaction schemes for quinoline derivative formation from pyridyl radicals and 1,3-butadiene.

as well as the formation of the dihydro(*iso*)quinoline isomers (plus H) from barrierless reactions involving the pyridyl radicals (C_5H_4N) and 1,3-butadiene (Figure 1.1).[21, 43] Barrierless reactions such as these can lead to PAHs/PANHs present in the ISM. Since the pyridyl radicals are simple, prototypical nitrogen heterocycle radicals, and the rotational spectra have never been measured, they are a major target of interest for the work described in this dissertation.

The analysis of Titan's atmosphere (one of Saturn's moons) has long been regarded as a unique opportunity for studying the chemical diversity and abundance in space.[44–46] *In situ* measurements from the Cassini-Huygens orbiter mission and land-based observations indicate the atmospheric composition to be a haze layer (N_2 , CH_4 , hydrocarbons and aromatics), and therefore similar to Earth.[45, 47–50] To try and understand the photodissociation mechanism applicable to Titan's atmosphere, laboratory experiments have detected the HCN and HCCN radicals from ultraviolet-vacuum ultraviolet irradiation of a N_2/CH_4 gas mixture at 60 and 82.5 nm, respectively.[51] The formation of these types of radicals are likely suggesting that these molecules could be involved in radical-neutral reactions forming larger nitrogen-containing organic aerosols and other stable products in the low temperature regions of Titan's atmosphere.[21–23, 28, 46] In this way, it may be possible to find answers as to how molecules of prebiotic interest are formed under similar environmental conditions

to early Earth.

1.1.3 Unidentified Infrared (UIR) Emission Bands

Unidentified Infrared (UIR) emission collected from interstellar/circumstellar environments have been attributed to PAHs/PANHs and other organics.[30, 52] The strong UIR signatures that are linked to neutral and ionized PAH/PANHs are located at the wavelengths 3.3, 6.2, 7.7, 8.6, and 11.2 μm , and tend to be independent of source.[2, 29, 32, 53, 54] Although these signatures are indicative of the presence of aromatic CC stretching and CC bending modes, no definitive detection of an individual molecule has been made based solely on UIR emission features. Shifts in peak positions between 6.2 and 6.3 μm appear to be the result of nitrogen substitution embedded further into the inner part of the aromatic ring.[31, 55–57] In addition to PAHs, PANHs are thought to be ubiquitous in the ISM ($\approx 1\text{--}2\%$ of cosmic nitrogen is thought to be present in PANHs) however, as of yet, no PANH has been detected in space.[31, 58, 59]

1.1.4 Meteorites

Chemical analysis of meteorites (e.g., Murchison, Tagish Lake, Murray, etc.) provides insight into prebiotic systems that may have played a significant role in the evolution of life on Earth.[60–62] Extraterrestrial meteorites come in many forms based on their composition and level of alteration (i.e., thermal/aqueous changes) since breaking from the meteorite parent body, ultimately influencing the chemical composition of the meteorite. The degree of alteration can be used to predict its original local environment: for example, aqueous alteration indicates low-temperature reactions with water.[63] Of the various types of meteorites that crash to Earth, the majority are chondritic meteorites that have not been altered from the meteorite parent body and are rich in soluble organic molecules.[61] Among the chondrites, carbonaceous chondrites are most similar in composition to that of the solar photosphere (lowest layer of the solar atmosphere), and the contents of these meteorites are thought to be formed in the ISM.[64, 65] Isotopic ratio analysis of meteorites via high-resolution analytical methods (e.g., GC-MS, ^{13}C NMR, chromatographic separation) have determined the

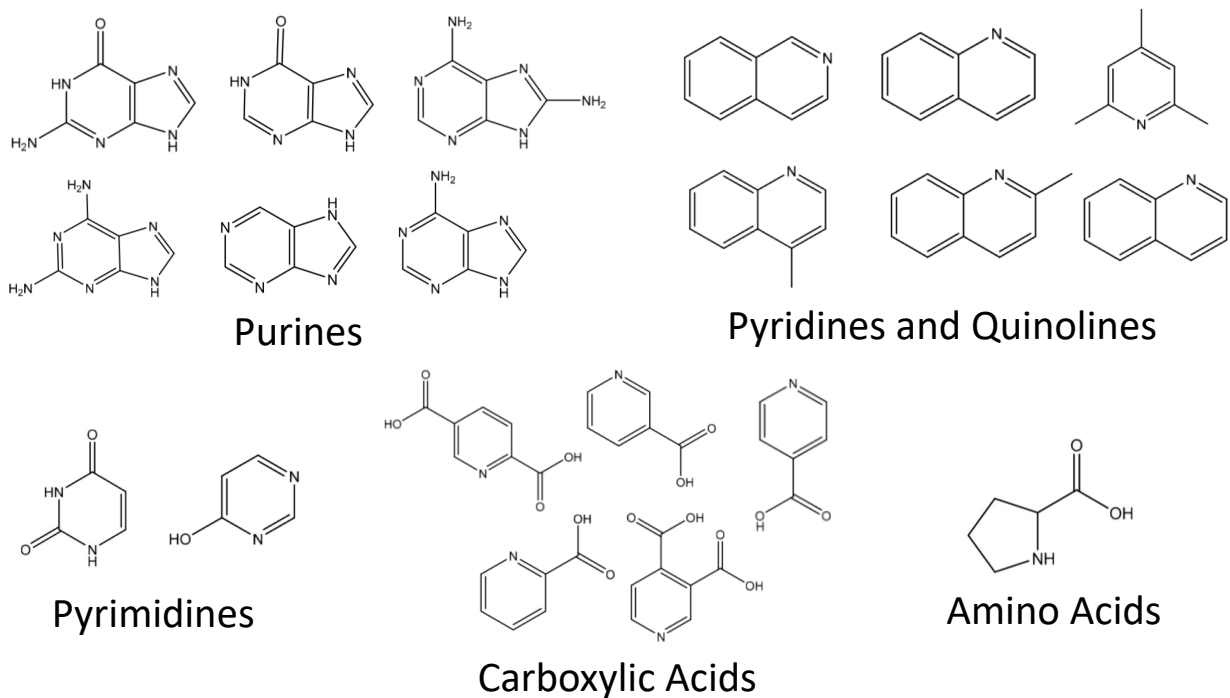


Figure 1.2: Example molecular detections on the Murchison meteorite, a carbonaceous chondrite.

chemical compositions to be chemically diverse (see Figure 1.2) and extraterrestrial in origin (supported by D, ^{13}C , and ^{15}N enrichment).[66–71] As a result of advances in laboratory analytical techniques which allow direct analysis of the composition of meteorites, potential synthetic pathways have been suggested for the formation of COMs during the evolution of the Solar System.[62, 72–74]

1.2 Ab Initio Quantum Chemical Methods for High-Resolution Spectroscopy

Astronomers use rotationally-resolved spectral data to detect molecules in interstellar space.[19, 75, 76] Data collected from land-based and aerial observations can be difficult to interpret, as there is a forest of spectral lines to analyze. To identify and quantify a species' abundance, it is essential to know the rotational transition frequencies. To that end, experimentally determined values are necessary and theoretical values alone is rarely sufficient. To illustrate spectral density in the microwave region, the NRAO Spectral Line Catalog (Splatalogue)

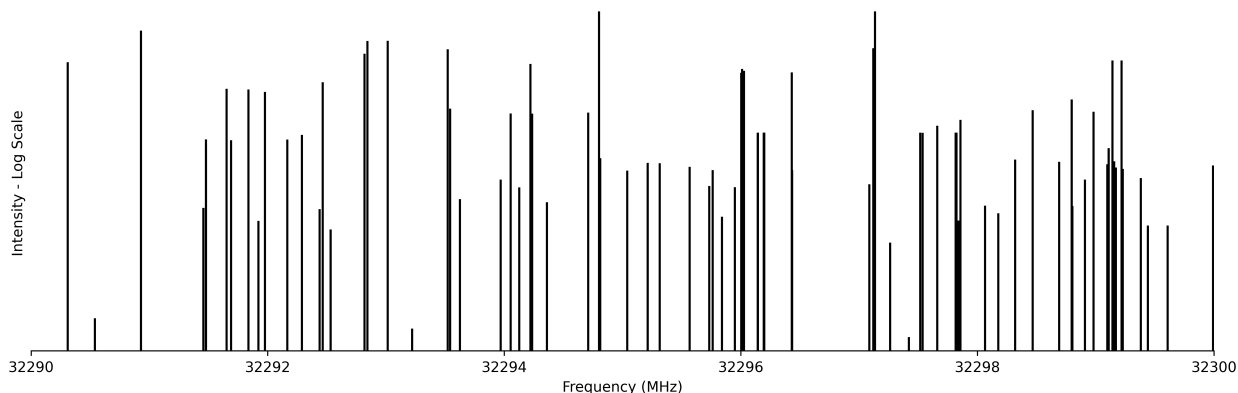


Figure 1.3: Simulated rotational spectrum from 32290 – 32300 MHz using transition frequencies and intensities from Splatalogue.

was used to illustrate the number of astrochemically known molecules in a random 10 MHz frequency bandwidth.[77] Figure 1.3 shows the calculated rotational transition frequencies of 35 molecules from a snippet of data between 32290 – 32300 MHz. The Boltzmann-weighted logarithmic intensities of the rotational transitions are also depicted. In this 10 MHz simulation, there are 105 unique rotational transitions. In order to distinguish between the rotational transitions and determine their molecular origin, rotational transition frequencies need to be known to an accuracy of a few hundreds of kHz, since the line density is on the order of tens of lines/MHz.[78–80] For spectral assignment of interstellar data, rotational transition frequencies of a given molecule are measured in laboratory experiments. Interpretation of laboratory measured data is based on quantum chemical calculations predicting rotational transitions and quantum number assignments.[81–83]

Coupled-cluster (CC) theory is a widely used computational method in the field of astrochemistry, and is the chosen method for investigating the radicals of interest in this dissertation.[84–90] It has been shown that bond distances and rotational constants can be determined via CC methods with accuracies within 0.001 Å and 20 MHz of experimental values, respectively.[78, 91–93] As a result of the unpaired electron in radicals and multiple atoms with $I > 0$ nuclear spin, there are numerous sources of angular momentum coupling that complicate the rotational spectra. To generate simulations for spectroscopic investigations, the necessary calculations include fully optimized structures, vibrationally

corrected rotational constants, centrifugal distortion constants, spin-rotation tensors, spin-spin tensors, quadrupole coupling tensors, and vibrational properties evaluated using second order vibrational perturbation theory (VPT2) with variational corrections (VPT2+K).[94–99] These spectroscopic parameters can be used to simulate the rotational and vibrational spectra of radicals. Chapter 2 describes the quantum mechanical methods used to simulate the rotational and vibrational spectra of radicals and Chapter 3 contains the published computational results for the pyridyl radicals.

1.3 Experimental Rotational Spectroscopy

Rotational spectroscopy is generally defined as the analysis of rotational transitions of polar, gas-phase molecules over a wide range of electromagnetic frequencies, ranging from millimeter to centimeter wavelengths.[100] Instruments that are developed to measure rotational spectra cover a limited spectral region because of the technical limitations of the data acquisition rate.[101] The National Bureau of Standards (NBS) performed the first high-resolution microwave measurements on the 23.9 GHz transitions of ammonia in the 1940s. [102, 103] In the years since then, rotational spectroscopy has been applied to a variety of scientific fields, including astrochemistry and astronomy, in order to study chemical kinetics, dynamics, and precise molecular structures.[104–109] Through the advancement of technology over the years, rotational spectroscopy has expanded its applications to include weakly bound complexes, radicals, ions, and other forms of transient species.[110, 111] A number of early experiments involving microwave radiation were based on Stark modulation measurements as well as direct microwave absorption spectroscopy[112, 113], but these have largely been replaced by Fourier transform microwave (FTMW) spectroscopy in more recent years.[101, 114–116]

The advent of the chirped-pulse Fourier transform microwave (CP-FTMW) spectrometer improved broadband collection of rotational spectra ($\approx 10^6$ resolution elements per shot) in a reduced measurement time.[117, 118] This spectrometer achieves high frequency resolution without the power broadening or line shape distortion found in Stark modulation spectrom-

eters. [104] The theory behind CP-FTMW spectroscopy will be discussed in greater detail in Chapter 4. Two CP-FTMW spectrometers were custom-built and tested for measuring the rotational spectra of radicals: a Ka-band CP-FTMW spectrometer and a segmented CP-FTMW spectrometer. With the ability to operate across the frequency range of 13.5 GHz with a single microwave pulse (Ka-band CP-FTMW) or 1 GHz segments (segmented CP-FTMW), they are suitable for the rapid collection of rotational spectra. Instrumentation and preliminary results for these instruments are presented in Chapters 5 and 6.

Chapter 2

Spectroscopic Characterization of Radicals Using Ab Initio Methods

2.1 Introduction

In the fields of observational astronomy and astrochemistry, rotational and vibrational spectroscopy are used to understand the chemical composition of the universe.[119, 120] Molecular detections and derived abundances can help elucidate any potential chemical reactions at play in space.[12, 121, 122] Among the many factors that make up astrochemical models, precise structure of all reactants, products, and intermediate species that are included in potential reactions must be determined.[2] The analysis of rotationally resolved molecular spectra is commonly used for this purpose.[119, 123, 124] Ab initio quantum chemical calculations provide much needed guidance for experimental studies of new molecules by predicting transition frequencies and the corresponding spectroscopic parameters needed to simulate spectra and chemical abundances.[78, 80, 91, 120, 125] The following sections provide detailed information on methods for calculating spectroscopic parameters for radicals necessary for rotational and vibrational spectroscopic studies. This includes a discussion of the rigid rotor model, angular momentum coupling, and second order vibrational perturbation theory (VPT2). Application of these methods to pyridyl radicals can be found in the published paper shown in Chapter 3.

2.2 The Molecular Hamiltonian

The construction of the molecular Hamiltonian, which involves the properties of the nuclei and electrons in a molecule, is necessary in order to calculate the spectroscopic parameters for rotational and vibrational spectroscopy. The spin-free molecular Hamiltonian is given by

$$\hat{H} = \hat{T} + \hat{V}(R_n, r_e), \quad (2.1)$$

where \hat{T} includes the electron/nuclear kinetic energy (\hat{T}_e and \hat{T}_n), and $\hat{V}(R_n, R_e)$ is the electrostatic potential energy (\hat{V}_{en} , \hat{V}_{ee} , and V_{nn}) dependent upon the interparticle distances (R_n, r_e) among electrons (e) and nuclei (n). Under the Born-Oppenheimer approximation, nuclear motion is slow compared to the motions of the electrons and can be neglected during the treatment of electron behavior. As a result of this approximation, the nuclear kinetic energy term ($\hat{T}_n = 0$) is removed from the electronic part of the molecular Hamiltonian and V_{nn} is constant. This allows for the electronic wavefunction and the approximate electronic energies that describe electronic motion to be obtained from the solution to the Schrödinger equation. This ultimately reduces the problem to solving the electronic and rovibrational Schrödinger equations separately with wavefunctions, Ψ_e and Ψ_{rv} . A thorough discussion of the nuclear and spin Hamiltonian will come in later sections.

The electronic Schrödinger equation is given by,

$$\hat{H}_e \Psi_e = V_e \Psi_e, \quad (2.2)$$

where V_e is comprised of \hat{T}_e , \hat{V}_{ee} , and V_{en} . Saving the treatment of \hat{V}_{ee} for later (i.e., independent particle model) and separating it from the \hat{T}_e and V_{en} terms reduces the electronic Hamiltonian to the sum of one-electron Hamiltonians, where the electronic wavefunction is now

$$\Psi_e = \phi_a(r_1)\phi_b(r_2)\dots\phi_k(r_n), \quad (2.3)$$

where $\phi_k(r_n)$ represents the molecular orbitals (MOs) over r electronic coordinates, as given

by

$$\phi_k(r) = \sum_{\mu=1}^{N_b} c_{\mu k} \chi_{\mu}(r). \quad (2.4)$$

$c_{\mu k}$ is the expansion coefficient and $\chi_{\mu}(r)$ represents the basis function. μ is indexed over the number of basis functions, N_b , and k is a specific MO. For $\chi_{\mu}(r)$, Slater-type orbitals and Gaussian-type orbitals are commonly chosen basis functions and $c_{\mu k}$ is determined after an initial guess prior to the SCF process. The approximate electronic energy is

$$V_e^0 = \epsilon_a + \epsilon_b + \dots + \epsilon_k, \quad (2.5)$$

where ϵ_k represents the MO energies, of which the solutions can be determined for the motion of an electron with a fixed nuclear arrangement.

Hartree-Fock Self-Consistent Field theory (HF-SCF) is the simplest method of addressing the electron-electron (V_{ee}) energy term. To represent the electronic wavefunction, a Slater determinant is constructed of orbital functions with α and β spin functions, occupied by n electrons,

$$\Psi_{HF} = \frac{1}{\sqrt{n!}} |\phi_1 \alpha \phi_2 \beta \dots \phi_{n/2} \alpha \phi_{n/2} \beta|. \quad (2.6)$$

Equation 2.6 depicts the electronic wavefunction for a closed-shell molecule with an even number of electrons.

The potential energy from electron-electron interactions can be approximated by calculating the expectation value of $1/r_{ij}$, where r is the distance between electrons, and $|\Psi\rangle$ is the HF wavefunction,

$$V_{ee} = \sum_{\substack{i,j \\ i < j}} \left\langle \Psi_{HF} \left| \frac{1}{r_{ij}} \right| \Psi_{HF} \right\rangle. \quad (2.7)$$

Minimizing the expectation value by iterative calculations of expansion coefficients is when self-consistency is reached. Once this has been achieved, the SCF approximation to the ground state electronic energy, V_{ee} , is obtained. However, HF-SCF theory is incomplete in its treatment of the total electronic system because it does not treat dynamic electron

correlation. It is therefore necessary to improve the SCF practice and choose a quantum chemical method that takes into account electron-electron correlation effects.

2.3 Coupled Cluster Method

The Coupled-cluster (CC) method can address the problem of electron correlation. The development of CC theory first began in the 1960s applied to nuclear wavefunctions[126, 127] and was later applied to atoms and molecules in the 1990s.[128] While the CC method has been well established for predicting accurate equilibrium structures and energies, the computational cost of the method is high.[84] The following discussion on this theoretical method has been adapted from Ref [78], which concisely describes various approaches to quantum-chemical calculations specifically for spectroscopic investigations.

The CC electronic wavefunction is given by

$$\begin{aligned} |\Psi_{\text{CC}}\rangle &= e^{\hat{T}}|\Psi_{\text{HF}}\rangle, \\ e^{\hat{T}} &= 1 + \hat{T} + \frac{\hat{T}^2}{2!} + \frac{\hat{T}^3}{3!} + \dots \end{aligned} \tag{2.8}$$

where the cluster operator, \hat{T} , is a power series expansion over m electrons,

$$\hat{T} = \sum_{i=1}^m \hat{T}_i. \tag{2.9}$$

\hat{T}_i corresponds to a specific level of electron excitation from a set of occupied orbitals in the Slater determinant reference wavefunction (i, j, k, l, \dots) to a set of unoccupied virtual orbitals (a, b, c, d, \dots), where all electrons from all possible occupied orbitals can be excited to all possible unoccupied orbitals, as depicted in Figure 2.1. \hat{T}_i is an i -fold excitation operator that generates i -fold excited Slater determinants, and for simplicity, Figure 2.1 is depicting only one determinant generated by \hat{T}_1 , \hat{T}_2 , and \hat{T}_3 . The result of applying the cluster operators to the Ψ_{HF} reference wavefunction can be expressed as a product of amplitudes

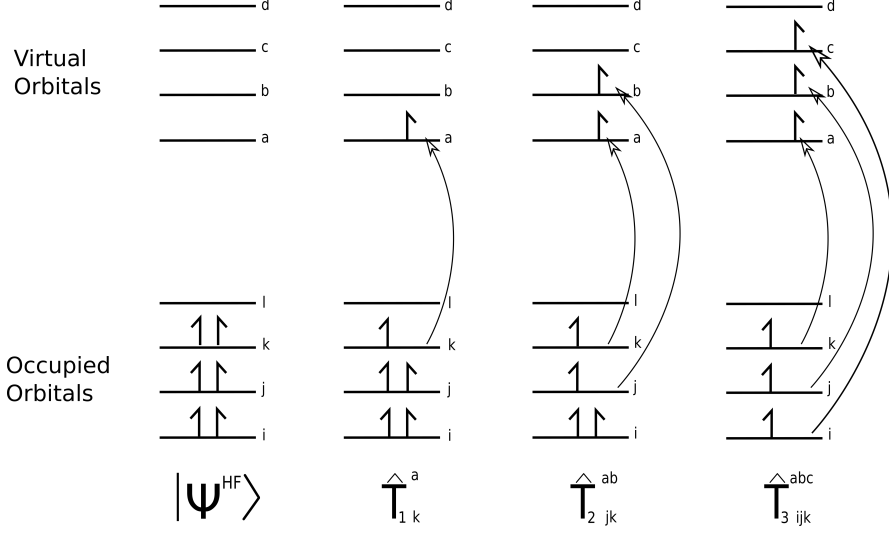


Figure 2.1: General examples of the singles, doubles, and triples excitations due to the \hat{T}_1 , \hat{T}_2 , and \hat{T}_3 cluster operators. i, j, k, l, \dots indices represent occupied orbitals and a, b, c, d, \dots indices represent virtual orbitals.

($t_i^a, t_{ij}^{ab}, t_{ijk}^{abc}$, etc.) and excited determinants, shown in Equation 2.10.

$$\begin{aligned}
 \hat{T}_1 \psi_{HF} &= \sum_{i,a}^{occ,virt} t_i^a \psi_i^a & (2.10) \\
 \hat{T}_2 \psi_{HF} &= \sum_{\substack{i<j \\ a<b}}^{occ,virt} t_{ij}^{ab} \psi_{ij}^{ab} \\
 \hat{T}_3 \psi_{HF} &= \sum_{\substack{i<j<k \\ a<b<c}}^{occ,virt} t_{ijk}^{abc} \psi_{ijk}^{abc} \\
 &\dots
 \end{aligned}$$

Those CC amplitudes are determined by solving the CC Schrödinger equation through the use of perturbation theory and evaluation of overlap integrals,

$$\begin{aligned}
 \hat{H}_e |\Psi_{CC}\rangle &= E_{CC} |\Psi_{CC}\rangle & (2.11) \\
 \langle \Psi_{HF} | \hat{H}_e | \Psi_{CC} \rangle &= E_{CC} \langle \Psi_{HF} | \Psi_{CC} \rangle \\
 \langle \Psi_{HF} | \hat{H}_e | \Psi_{CC} \rangle &= \left[\sum_{\substack{i<j<k\dots \\ a<b<c\dots}}^{occ,virt} t_{ijk\dots}^{abc\dots} \right] E_{CC}
 \end{aligned}$$

Including all terms in the expansion in Equation 2.10 (where $m = \#$ of electrons) would be equivalent to performing full configuration interaction (achieving exact solutions), which is not practical for most systems, so truncating at a certain level of excitation is common. For example, when \hat{T} is truncated at \hat{T}_2 , the method is called coupled-cluster singles and doubles (CCSD).

Single and double excitations with an estimation of the triple excitation contribution (CCSD(T)) is often used for small to medium sized systems (e.g., 2–20 atoms) in order to mitigate the increased computational costs that more excitations incur (triple, quadruple, etc.). Considerable effort has gone into determining the mean error between CCSD(T) calculated equilibrium structures and experimental values.[129, 130] Several studies have shown that CCSD(T) is accurate to within 0.2 – 0.3 pm for bond distances, assuming it is paired with a large enough basis set.[84, 87, 130, 131] Therefore, it has been demonstrated that by means of CC methods, approximate equilibrium structures can be computed based on Born-Oppenheimer potential surfaces and additional electronic properties can be calculated from the electronic wavefunction.

2.4 Watson’s Nuclear Hamiltonian

The normal mode representation of the rotation-vibration molecular Hamiltonian describes the internal motion of a molecule and is commonly referred to as Watson’s Hamiltonian. As a first step towards deriving this Hamiltonian in terms of rotational and vibrational motion, it can first be expressed in terms of kinetic energy with respect to the center of mass (\hat{T}_{CM}) and internal motion independent of the coordinates of the center of mass (\hat{H}_{int}), as shown by,

$$\hat{H} = \hat{T}_{\text{CM}} + \hat{H}_{\text{int}}. \tag{2.12}$$

The eigenfunctions (with an x, y , and z axes system) are then

$$\Phi = \Phi_{\text{CM}}(x_0, y_0, z_0)\Phi_{\text{int}}(x_1, y_1, z_1, \dots, x_l, y_l, z_l), \tag{2.13}$$

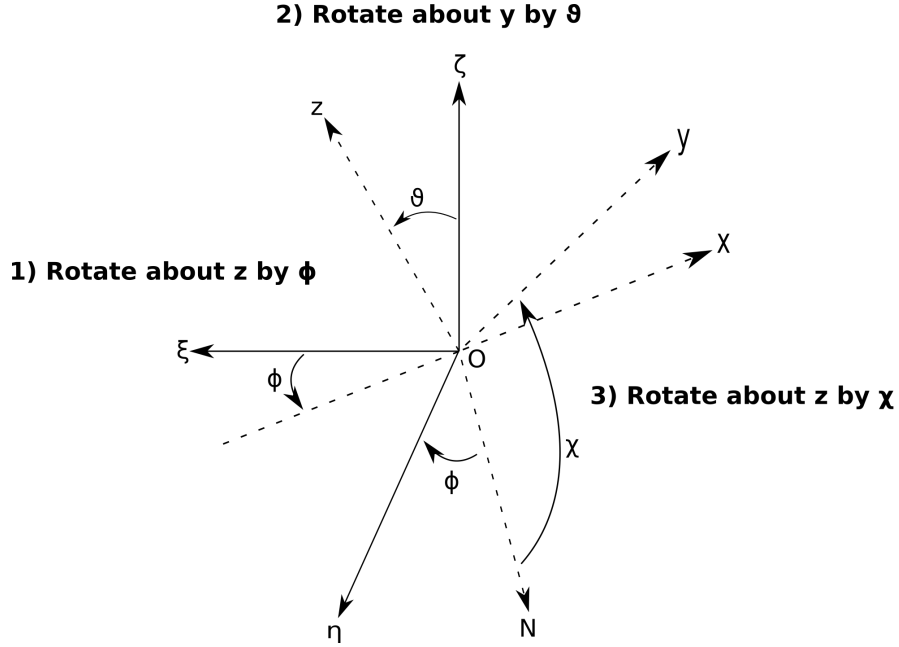


Figure 2.2: Representation of the Euler angles (θ , ϕ , χ), molecule-fixed axes (x , y , z), and nuclear positions (ξ , η , ζ), around the nuclear center of mass, O . Rotation convention occurs first about the z -axis by ϕ , then about the y -axis by θ (resulting in \vec{N}), and then about the z -axis by χ .

where x_0 , y_0 , z_0 are the center of mass coordinates and the internal coordinates ($x_1, y_1, z_1, \dots, x_l, y_l, z_l$) run over the total number of particles l . The Schrödinger equations are

$$\hat{T}_{\text{CM}}\Phi_{\text{CM}} = E_{\text{CM}}\Phi_{\text{CM}}, \quad (2.14)$$

$$\hat{H}_{\text{int}}\Phi_{\text{int}} = E_{\text{int}}\Phi_{\text{int}}, \quad (2.15)$$

and the total energy of the system is $E = E_{\text{CM}} + E_{\text{int}}$. In this coordinate system, translation is completely independent of internal motion, and here we focus only on \hat{H}_{int} . The coordinates for the rotational motion are functions of Euler angles (θ , ϕ , χ) and the nuclear coordinates (ξ , η , ζ) are the displacements.[132, 133] Rotation conventions about the x , y , and z coordinates are depicted in Figure 2.2. The Eckart frame ensures the separation of rotational and vibrational degrees of freedom in the rotational-vibrational Hamiltonian by defining three equations that represent those Euler angles. By converting the coordinates in this manner, the rotation-vibration Hamiltonian can be separated with minimal approximation.[133] Watson showed that the internal Hamiltonian can be expressed in these

coordinates as the spin-free Watson Hamiltonian for rotation-vibration, and in Watson's notation, is given by[97, 134, 135]

$$\hat{H}_{\text{Watson}} = \underbrace{\frac{1}{2} \sum_{\alpha\beta} (J_\alpha - \pi_\alpha) \mu_{\alpha\beta} (J_\beta - \pi_\beta)}_{\hat{H}_{\text{rot}} + \hat{H}_{\text{cd}}} + \underbrace{\frac{1}{2} \sum_k P_k^2 + U + V(q_1, q_2, \dots, q_{3N-6})}_{\hat{H}_{\text{vib}}}. \quad (2.16)$$

The first term represents the pure rotation and the vibration-rotation interaction. $J_{\alpha,\beta}$ is the angular momentum operator with respect to rotation about a molecule-fixed axis system (α and $\beta = x, y, \text{ and } z$) and $\pi_{\alpha,\beta}$ represents the vibrational angular momentum that includes the Coriolis interactions. $\mu_{\alpha\beta}$ is an effective reciprocal inertia tensor and can be expressed as a Taylor series in normal coordinates, q_r ,

$$\mu_{\alpha\beta} = \mu_{\alpha\beta}^e - \sum_r \mu_{\alpha\alpha}^e a_r^{\alpha\beta} \mu_{\beta\beta}^e q_r + \frac{3}{4} \sum_{r,s,\gamma} \mu_{\alpha\alpha}^e a_r^{\alpha\gamma} \mu_{\gamma\gamma}^e a_s^{\gamma\beta} \mu_{\beta\beta}^e q_r q_s + \dots, \quad (2.17)$$

where $\mu_{\alpha\beta}^e$ is an element of the inverse of the moment of inertia (I) at equilibrium, and the coefficients $a_r^{\alpha\beta}$ depend on the equilibrium nuclear geometry, nuclear masses, and nuclear potential energy.[133] The last three terms of Equation 2.16 represent pure vibration, where P_k is the momentum conjugate to the normal coordinate q_k , $V(q_r)$ encompass the electronic potential energy, and U is a constant mass-dependent contribution to the potential.

In order to define the rotational Hamiltonian, a classical description of angular momentum should be discussed. All non-vibrating particles in a rotating body have the same angular velocity ω about the center of mass, where the velocity is $\vec{v} = \omega \times \vec{r}$. The total angular momentum (J) of each particle ($i = 1, 2, \dots, n$), with mass m_i and position r_i , about that center of mass in the space-fixed frame, is

$$\vec{J} = \sum_i m_i (\vec{r}_i \times \vec{v}_i), \quad (2.18)$$

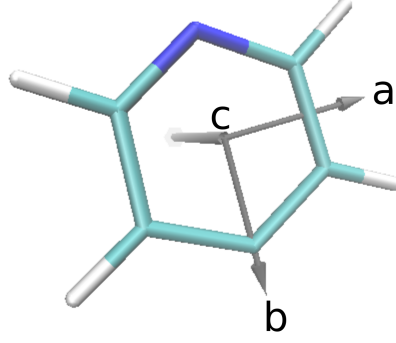


Figure 2.3: Principal axes of 4-pyridyl.

and in terms of the inertia tensor and ω , [136]

$$\hat{J} = \hat{I} \cdot \hat{\omega} \quad (2.19)$$

$$\begin{bmatrix} J_x \\ J_y \\ J_z \end{bmatrix} = \begin{bmatrix} I_{xx} & I_{xy} & I_{xz} \\ I_{yx} & I_{yy} & I_{yz} \\ I_{zx} & I_{zy} & I_{zz} \end{bmatrix} \begin{bmatrix} \omega_x \\ \omega_y \\ \omega_z \end{bmatrix}. \quad (2.20)$$

It is because of a particular orientation of the center of mass that the inertia tensor becomes a diagonal matrix, whose eigenvalues represent the principal moments of inertia (I_{aa}, I_{bb}, I_{cc}). [137]

$$\begin{bmatrix} I_{aa} & 0 & 0 \\ 0 & I_{bb} & 0 \\ 0 & 0 & I_{cc} \end{bmatrix} \quad (2.21)$$

The axis system is now called the principal axis system (a, b, c), as depicted in Figure 2.3 for 4-pyridyl. By convention, $I_{aa} \leq I_{bb} \leq I_{cc}$, and in the principal axis system, the components of J are given by the following equations:

$$J_a = I_{aa}\omega_a, \quad J_b = I_{bb}\omega_b, \quad J_c = I_{cc}\omega_c. \quad (2.22)$$

The kinetic energy for a polyatomic molecule, in the center of mass frame, is

$$T = \frac{1}{2}(\omega_a J_a + \omega_b J_b + \omega_c J_c), \quad (2.23)$$

$$T = \frac{1}{2}(\omega_a^2 I_{aa} + \omega_b^2 I_{bb} + \omega_c^2 I_{cc}), \quad (2.24)$$

$$T = \frac{1}{2} \left(\frac{J_a^2}{I_{aa}} + \frac{J_b^2}{I_{bb}} + \frac{J_c^2}{I_{cc}} \right). \quad (2.25)$$

For convenience, rotational constants are used in place of moments of inertia; in spectroscopic units of MHz, they are related to moments of inertia in units of kg m²,

$$A = \frac{\hbar}{4\pi I_{aa}} \times 10^{-6}, \quad B = \frac{\hbar}{4\pi I_{bb}} \times 10^{-6}, \quad C = \frac{\hbar}{4\pi I_{cc}} \times 10^{-6}. \quad (2.26)$$

Therefore, the kinetic energy in terms of rotational constants and angular momentum, reduces to,

$$T = AJ_a^2 + BJ_b^2 + CJ_c^2, \quad (2.27)$$

where $A \geq B \geq C$.

Molecules fall into one of several categories based on the relative values of their rotational constants.

- Linear molecules: $A = \infty$ and $B = C$
- Spherical tops: $A = B = C$
- Symmetric tops
 - Prolate symmetric tops: $A > B = C$
 - Oblate symmetric tops: $A = B > C$
- Asymmetric tops: $A > B > C$

The majority of molecules are asymmetric tops, but there is no closed-form energy solution for these types of molecules, so instead the energy levels are determined by diagonalization in a symmetric top basis.

2.4.1 The Rigid Rotor Hamiltonian

Rotational spectroscopy can, to first order, be approximated by the rigid rotor model. This assumes bonds between nuclei are rigid, ignoring perturbations to the system caused by vibrational motion. The rigid rotor rotational Hamiltonian is given by the leading $\mu_{\alpha\beta}$ term in Equations 2.16 and 2.17, where $\mu_{\alpha\beta}^e = 0$ if $\alpha \neq \beta$ and all $q_r = 0$ and $\Pi_\alpha = 0$,

$$\hat{H}_{\text{rr}} = \frac{\hbar}{2} \sum_{\alpha} \mu_{\alpha\alpha} \hat{J}_{\alpha}^2. \quad (2.28)$$

The rigid rotor Hamiltonian, defined in terms of the angular momentum operator (\hat{J}), is given by.

$$\hbar^2 \hat{H}_{\text{rr}} = X \hat{J}_x^2 + Y \hat{J}_y^2 + Z \hat{J}_z^2. \quad (2.29)$$

X , Y , and Z represent the rotational constants and depending upon the chosen mapping of the principal axes, xyz can map to abc in six different ways. For convenience, different mappings are chosen for prolate ($xyz \longleftrightarrow bca$) and oblate ($xyz \longleftrightarrow abc$) tops. The three components of \hat{J} (\hat{J}_x , \hat{J}_y , and \hat{J}_z) are not mutually observable. Traditionally, \hat{J}_z is chosen to commute with \hat{J}^2 ($[\hat{J}^2, \hat{J}_z] = 0$), and in a symmetric top, the z -axis is chosen to correspond to the symmetry axis to simplify the problem.

The eigenvalues for the $|JK\rangle$ eigenfunctions of a symmetric top basis are given by

$$\begin{aligned} \hat{J}^2 |JK\rangle &= J(J+1)\hbar^2 |JK\rangle, \\ \hat{J}_z |JK\rangle &= K\hbar |JK\rangle, \end{aligned} \quad (2.30)$$

where J is the angular momentum quantum number and K is the projection of J onto the molecular z -axis in units of \hbar . J can take integer values ≥ 0 and $K \rightarrow J, J-1, \dots, -J+1, -J$. The prolate and oblate top energy levels are given by the following expression,

$$E = YJ(J+1) + (Z-Y)K^2 \quad (2.31)$$

where Z is the unique rotational constant. As mentioned above, the asymmetric top Hamiltonian is solved by diagonalization in a symmetric top basis. However, the choice of the x ,

y , and z axes is less straightforward. Therefore, Ray's asymmetry parameter, κ , provides a quantitative measure of how far a molecule is from any specific type of symmetry limit, and is a measure of prolate or oblate character,[138]

$$\kappa = \frac{2B - A - C}{A - C}, \quad (2.32)$$

with $\kappa = -1$ for a prolate symmetric top and $\kappa = +1$ for an oblate symmetric top. κ values close to -1 use the I^r representation, κ values close to $+1$ use the III^r representation, while $\kappa \approx 0$ sometimes use the II^r representation.

The rigid rotor asymmetric top Hamiltonian can be written in terms of raising ($\hat{J}_- = \hat{J}_x - i\hat{J}_y$) and lowering ($\hat{J}_+ = \hat{J}_x + i\hat{J}_y$) operators:

$$\hat{H}_{\text{rr}} = \left(\frac{X+Y}{2} \right) \hat{j}^2 + \left(Z - \frac{X+Y}{2} \right) \hat{j}_z^2 + \frac{X-Y}{4} (\hat{j}_+^2 + \hat{j}_-^2). \quad (2.33)$$

In addition to the symmetric top matrix elements previously stated above in Equation 2.30, the matrix elements that include the raising/lowering operators (Equation 2.34) are also useful for constructing the matrix elements for an asymmetric top,

$$\begin{aligned} \langle J' K' | \hat{J}_+^2 | JK \rangle &= \hbar^2 \sqrt{(J+K)(J-K+1)(J+K-1)(J-K+2)} |J, K-2\rangle \\ \langle J' K' | \hat{J}_-^2 | JK \rangle &= \hbar^2 \sqrt{(J-K)(J+K+1)(J-K-1)(J+K+2)} |J, K+2\rangle. \end{aligned} \quad (2.34)$$

A $(2J+1) \times (2J+1)$ dimensional Hamiltonian matrix is then constructed for any value of J . For example, for $J = 1$, the 3×3 dimensional matrix is given by

$$\hbar^2 \hat{H} = \begin{pmatrix} Z + \frac{X+Y}{2} & 0 & \frac{X+Y}{2} \\ 0 & X+Y & 0 \\ \frac{X-Y}{2} & 0 & Z + \frac{X+Y}{2} \end{pmatrix}. \quad (2.35)$$

The construction and diagonalization of the Hamiltonian matrix for higher values of J can be readily performed with a computer. The energy level notation is $J_{K_a K_c}$, where K_a and K_c correspond to the projection of angular momentum on the molecular z -axis at the prolate or oblate limits, respectively. Only at those limits are they considered "good" quantum numbers. For $J = 1$, explicit expressions for the total rigid asymmetric rotor energy in terms of rotational constants are $A + B$ (1_{10}), $A + C$ (1_{11}), and $B + C$ (1_{01}).

Table 2.1: Selection rules for *a*-type, *b*-type, and *c*-type transitions for asymmetric tops.

Transition Type	Dipole Moment	ΔK_a	ΔK_c
<i>a</i> -type	$\mu_a \neq 0$	0, ± 2 , ± 4 , ...	± 1 , ± 3 , ± 5 , ...
<i>b</i> -type	$\mu_b \neq 0$	± 1 , ± 3 , ± 5 , ...	± 1 , ± 3 , ± 5 , ...
<i>c</i> -type	$\mu_c \neq 0$	± 1 , ± 3 , ± 5 , ...	0, ± 2 , ± 4 , ...

2.4.2 Rotational Selection Rules

Molecular dipole moments for an asymmetric top may not lie along a principal axis, but may be resolved along any of their three components: μ_a , μ_b , and/or μ_c . [139] This complicates the pure rotational selection rules for an asymmetric top. A transition dipole moment integral ($\langle \psi_1 | \hat{\mu}_z | \psi_2 \rangle$) must be nonzero in order for an electric dipole transition to occur, with the allowed transitions in terms of the inertial axes (*a*, *b*, *c*).

$$\langle \psi_1 | \hat{\mu}_z | \psi_2 \rangle = \mu_a \langle \psi_1 | \cos(az) | \psi_2 \rangle + \mu_b \langle \psi_1 | \cos(bz) | \psi_2 \rangle + \mu_c \langle \psi_1 | \cos(cz) | \psi_2 \rangle \neq 0. \quad (2.36)$$

The resulting constants μ_a , μ_b , and μ_c represent the magnitudes of the dipole moments along the three principal axes, and $\cos(az)$, $\cos(bz)$, and $\cos(cz)$ are the angles between the principal axes and the *z* axis. In the case of a nonzero dipole moment along all three axes, all possible transitions that are consistent with the general selection rule $\Delta J = 0, \pm 1$ are permitted. Any particular transition can be attributed to only one of the components of the dipole moment, and they are called *a*-type transitions, *b*-type transitions, and *c*-type transitions (Table 2.1). [139] An example of the $\Delta J = 1$ transition selection rule from the 0_{00} ground state is shown in Figure 2.4. [100, 138] Because the molecular dipole moment is also related to the rotational transition intensity, theoretical calculations of the dipole moments can provide quantitative information in addition to determining whether an experimental study is worthwhile.

2.4.3 Centrifugal Distortion

Simulations of the rotational spectra can be improved by including small amplitudes of vibration, in the form of centrifugal distortion effects. Treatment of centrifugal distortion

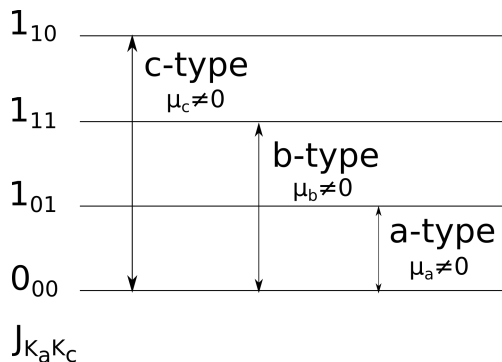


Figure 2.4: *a*-type, *b*-type, and *c*-type fundamental rotational transitions for $J' - J'' = 1 - 0$. Adapted from Ref.140

on the rotational Hamiltonian has been rigorously determined in Ref. 95; below are the key aspects of interest. Mathematically, the semi-rigid asymmetric top centrifugal distortion Hamiltonian is,

$$\hat{H}_{cd} = \sum_{\alpha, \beta}^{a, b, c} \tau_{\alpha\alpha\beta\beta} \hat{J}_\alpha^2 \hat{J}_\beta^2 + \sum_{\alpha}^{a, b, c} \Phi_{\alpha\alpha\alpha} \hat{J}_\alpha^6 + \sum_{\alpha \neq \beta}^{a, b, c} \Phi_{\alpha\alpha\beta} (\hat{J}_\alpha^4 \hat{J}_\beta^2 + \hat{J}_\beta^2 \hat{J}_\alpha^4) + \dots, \quad (2.37)$$

where the distortion coefficients, τ and Φ , are the quartic and sextic distortion constants, respectively.[119] Equation 2.37 is the result of a unitary transformation of Watson's Hamiltonian (Equation 2.16) to a reduced form. This dissertation worked with Watson's A reduction, which indicates the choice of reduction and of representation (among six different types) when using Watson's methods for analysis of rotational spectra of asymmetric tops.[141] In Watson's A reduction, the quartic distortion constants are listed as Δ_J , Δ_K , Δ_{JK} , δ_J , and δ_k , as depicted in Figure 2.5.

The Hamiltonian given in Equation 2.37 assumes a semi-rigid approximation; however, it is also necessary to take into consideration how the rotational constant varies with the vibrational level.[78, 142] For a polyatomic molecule in the ground vibrational state, these adjustments are made for all $3N - 6$ modes, thereby providing the average second-order

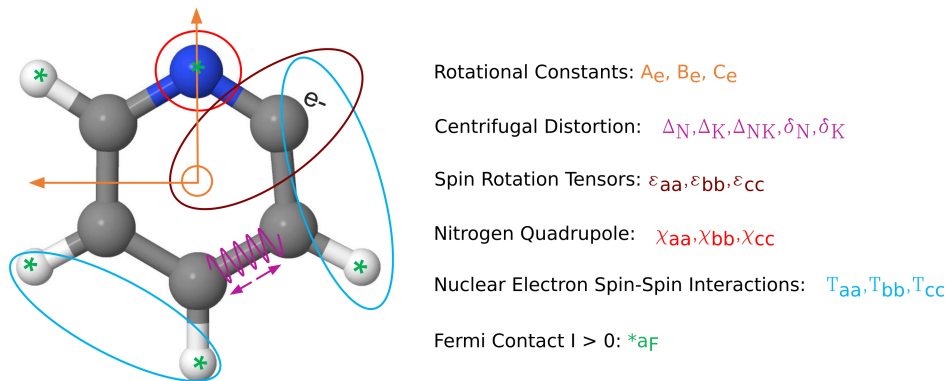


Figure 2.5: Depiction of angular momentum coupling and centrifugal distortion effects for 2-pyridyl.

correction to the rotational constants as

$$A_0 = A_e - \sum_{i=1}^{3N-6} \alpha_i^A \left(v_i + \frac{1}{2} \right), \quad (2.38)$$

$$B_0 = B_e - \sum_{i=1}^{3N-6} \alpha_i^B \left(v_i + \frac{1}{2} \right), \quad (2.39)$$

$$C_0 = C_e - \sum_{i=1}^{3N-6} \alpha_i^C \left(v_i + \frac{1}{2} \right), \quad (2.40)$$

where α_i is a vibration-rotation coupling constant, v is the vibrational quantum number, and A_0 , B_0 , and C_0 are the ground-state rotational constants.

2.4.4 Angular Momentum Coupling

Thus far, Watson's Hamiltonian has neglected spin, as stated previously in Equation 2.16. However, many of the molecules of astronomical interest are radicals with multiple heavy atoms of nonzero nuclear spin (e.g., H/N), so it is necessary to include the effects of spin to the rigid rotor Hamiltonian, thus altering the rotational Hamiltonian to include spin-rotation interactions (\hat{H}_{sr}) and hyperfine interactions (\hat{H}_{hfs}).

$$\hat{H}_{spin} = \hat{H}_{sr} + \hat{H}_{hfs} \quad (2.41)$$

This dissertation is focused on doublet radicals ($S = \frac{1}{2}$) containing C ($I = 0$), H ($I = \frac{1}{2}$) and N ($I = 1$) atoms, where I is the nuclear spin quantum number, and S is the electron

spin quantum number. An overview of the relevant couplings (2-pyridyl) and corresponding parameters is shown in Figure 2.5. The total angular momentum operator (\hat{F}) is the sum of these interactions, $\hat{F} = \hat{N} + \hat{S} + \sum \hat{I}$, where \hat{N} is the rotational and orbital angular momentum operator, \hat{S} is the electron spin angular momentum operator, and \hat{I} is the nuclear spin operator for each $I > 0$ nucleus. \hat{F}^2 commutes with the full molecular Hamiltonian, but when \hat{H}_{hfs} and \hat{H}_{sr} are small, N , I , J , and/or S may also be good quantum numbers.

2.4.4.1 Hyperfine Interactions

The hyperfine Hamiltonian can be further broken down into terms involving the nuclear quadrupole (\hat{H}_{Q}) and electronic spin-spin (\hat{H}_{ss}) interactions.

$$\hat{H}_{\text{hfs}} = \hat{H}_{\text{Q}} + \hat{H}_{\text{ss}}. \quad (2.42)$$

The following sections discuss these components of the spin Hamiltonian.

2.4.4.1.1 Nuclear Quadrupole Interaction The electric quadrupole moment (Q_{ij}) of an $I > \frac{1}{2}$ nucleus interacts with the electric field gradient (V_{ij}) at the nucleus:

$$E_{\text{Q}} = \frac{1}{6} \sum_{i,j=x,y,z} Q_{ij} V_{ij}, \quad (2.43)$$

where the i and j indices refer to the space-fixed x, y, z reference system. After a lengthy derivation in Ref. 100, the nuclear quadrupole Hamiltonian for a symmetric top (excluding nuclear spin) reduces to

$$\hat{H}_{\text{Q}} = \frac{\chi}{2J(2J-1)I(2I-1)} [3(\hat{I} \cdot \hat{J})^2 + \frac{3}{2} \hat{I} \cdot \hat{J} - \hat{I}^2 \hat{J}^2], \quad (2.44)$$

where χ is the nuclear quadrupole coupling tensor expressed in the principal axis system, which accounts for the magnitude of the nuclear quadrupole moment, the electric field gradient, and the orientation. The diagonal elements of the traceless nuclear quadrupole coupling tensor are depicted as χ_{aa} , χ_{bb} , and χ_{cc} in Figure 2.5.

2.4.4.1.2 Electron Nuclear Spin-Spin Interactions and Fermi Contact Terms In addition to nuclear quadrupole interactions, contributions from electron spin (for electronic states with $S > 0$) must also be included into the molecular Hamiltonian. The magnetic

hyperfine interaction is written in terms of a rank one spherical tensor, $T^1(\hat{x})$, and is given by

$$\hat{H}_{\text{hfs}} = a_F T^1(\hat{I}) \cdot T^1(\hat{S}) - \sqrt{10} T^1(\hat{I}) \cdot T^1(\hat{S}, C^2). \quad (2.45)$$

The first term represents the Fermi contact interaction; a_F is a constant term related to the spin density (α, β) at each nuclei. The second term is the spin-spin dipolar interaction and includes a second rank spherical tensor ($T^2(C)$) describing both the Cartesian distance and spherical polar angles between the electron relative to the nucleus. For planar molecules, the general five independent tensor elements reduces down to three.[143] In Figure 2.5, the diagonal spin-spin tensor elements for the H/N nuclei are represented in blue (T_{aa}, T_{bb}, T_{cc}).

2.4.4.2 Spin-Rotation Interaction

Spin-rotation interactions contribute to the molecular Hamiltonian for electronic states with $S > 0$. It is characterized by the coupling between electronic spin angular momentum and rotational angular momentum. The spin-rotation Hamiltonian[144] can be written in Cartesian tensor notation as,

$$\hat{H}_{\text{sr}} = \frac{1}{2} \sum_{\gamma, \delta=x,y,z} \epsilon_{\gamma\delta} (\hat{N}_\gamma \hat{S}_\delta + \hat{S}_\gamma \hat{N}_\delta), \quad (2.46)$$

where $\epsilon_{\gamma\delta}$ is the spin-rotation tensor, \hat{N} is rotational angular momentum operator, and \hat{S} is the spin angular momentum operator. The spin-rotation tensor is related to the second derivative of the electronic energy with respect to components of the spin and rotational angular momentum.[96] In the case of planar molecules, for which this dissertation is primarily focused, only five of the nine possible tensor elements are non-zero as a result of their symmetry. The diagonal terms of the spin-rotation tensor most significantly impact the rotational energy levels for a molecule, so Figure 2.5 shows only those three terms ($\epsilon_{aa}, \epsilon_{bb}$, and ϵ_{cc}).

2.5 Vibrational Energy Levels

From Watson's molecular Hamiltonian (Equation 2.16) that describes rotation-vibration interactions, only \hat{H}_{rot} (including spin) and \hat{H}_{cd} have been considered thus far. The remaining

term to discuss is \hat{H}_{vib} , which is the sum of the nuclear kinetic (\hat{T}_{vib}) and potential ($\hat{V}_{\text{vib}}(\hat{q})$) energy terms,

$$\hat{H}_{\text{vib}} = \hat{T}_{\text{vib}} + \hat{V}_{\text{vib}}(\hat{q}). \quad (2.47)$$

The potential in Watson's Hamiltonian, $V_{\text{vib}}(q)$, is a Taylor series expansion about the equilibrium over the $3N - 6$ normal coordinates, q ,

$$V_{\text{vib}}(q) = \frac{1}{2} \sum_i^{3N-6} k_i q_i^2 + \frac{1}{3!} \sum_{i,j,k} \phi_{ijk} q_i q_j q_k + \frac{1}{4!} \sum_{i,j,k,l} \phi_{ijkl} q_i q_j q_k q_l + \dots \quad (2.48)$$

which describes the energy associated with the displacement from equilibrium. The leading term represents the harmonic potential (V_{HO}) with the quadratic force constant k_i . The remaining terms are the anharmonic corrections (V_{anh}) to the harmonic potential given by cubic, quartic, etc. (ϕ_{ijk} , ϕ_{ijkl} , etc.) force constants, which are defined as the third and fourth derivatives of the potential energy with respect to the normal coordinate,[145]

$$\phi_{ijk} = \left(\frac{\partial^3 V}{\partial q_i \partial q_j \partial q_k} \right) \Big|_{q=0}, \quad \phi_{ijkl} = \left(\frac{\partial^4 V}{\partial q_i \partial q_j \partial q_k \partial q_l} \right) \Big|_{q=0}. \quad (2.49)$$

The anharmonic potential can be treated with perturbation theory using the harmonic oscillator part as the initial states ($|\Psi^{(0)}\rangle$) and energies ($E^{(0)}$). The total vibrational wavefunction is

$$\Psi^{(0)}(v_1, v_2, \dots, v_{3N-6}) = \prod_{i=1}^{3N-6} \psi_i(q_i), \quad (2.50)$$

and the harmonic solution to the Schrödinger equation gives the zero-point energy as

$$E_{v_1, v_2, \dots, v_{3N-6}}^{(0)} = \sum_i^{3N-6} \omega_i \left(v_i + \frac{1}{2} \right). \quad (2.51)$$

ω_i is the angular frequency of the harmonic oscillator (in rad/s) and is related to the force constant by $\omega_i = \sqrt{k_i/m_i}$ where m_i is the reduced mass of the vibrational mode, while v is the vibrational quantum number. Second-order vibrational perturbation (VPT2) theory

is conventionally used to approximate V_{vib} at the quartic terms. Applying VPT2 theory to V_{anh} gives the second-order energy as

$$E_i^2 = E_i^0 + \sum_{i \neq j} \frac{|\langle i | \hat{V}_{\text{anh}} | j \rangle|^2}{E_i^0 - E_j^0}. \quad (2.52)$$

The first term is the zeroth-order harmonic energy and the second term is the second-order anharmonic correction to that energy.

A resonance occurs when the denominator is zero as a result of accidental degeneracies. This happens when the difference between two energy levels are nearly equal ($E_i^0 - E_j^0 \approx 0$). VPT2 breaks down at this point, giving unrealistic (or undefined) values. Equations 2.53 and 2.54 show two types of resonance denominators when the i and j states differ by one quantum of excitation.

$$\frac{1}{2\omega_r - \omega_s} \quad (2.53)$$

$$\frac{1}{-\omega_r + \omega_s + \omega_t}, \frac{1}{\omega_r - \omega_s + \omega_t}, \frac{1}{\omega_r + \omega_s - \omega_t} \quad (2.54)$$

Computing the various energy differences between the harmonic frequencies generates a list of resonances that can potentially be treated. In the case of Fermi and Darling-Dennison (DD) resonances in a system, the treatment is known as VPT2+K. Fermi resonances occur between states that differ by a total of one quantum ($\Delta n \pm 1$) and come in two types: Type I ($\omega_a \approx 2\omega_b$) and Type II ($\omega_a \approx \omega_b + \omega_c$), whereas DD resonances occur between states that differ by a total of zero or two quanta ($\Delta n \pm 0, 2$).^[146] When vibrational states are sufficiently close, and the cubic (quartic) coupling is large, the effect of the resonance can shift the energy relative to the VPT2 value.

To generate the list of potential resonances, an arbitrary energy cutoff is chosen (e.g., $\approx 1 \text{ cm}^{-1}$) between two vibrational states (as well as a coupling threshold). For example, if the diagnostic test identified the following resonances,

$$\omega_a \approx \omega_b + \omega_c \quad (2.55)$$

$$\omega_b \approx 2\omega_d, \quad (2.56)$$

then the effective Hamiltonian to adequately treat those resonances is given by

$$H_{\text{eff}} = \begin{bmatrix} v_a^* & \frac{1}{2\sqrt{2}}\phi_{a,b,c} & \approx 0 \\ \frac{1}{2\sqrt{2}}\phi_{a,b,c} & (v_b + v_c)^* & \frac{1}{4}\phi_{b,d,d} \\ \approx 0 & \frac{1}{4}\phi_{b,d,d} & (2v_d + v_c)^* \end{bmatrix}. \quad (2.57)$$

After a variational treatment of the effective Hamiltonian is performed and the resonant terms are removed, the modified constant is marked with an asterisk. The eigenvalues of Equation 2.57 represent the variationally corrected energies and the eigenvectors contain the composition of the new vibrational state. This method ultimately provides a small number of treated states. Calculations are then repeated including more and more states, so as not to eliminate any candidates that could be contributing to frequency and intensity shifts by using VPT2 alone.[99]

VPT2+K was used extensively in the study of the pyridyl radicals because of its inclusion of both Fermi and DD resonances. Figure 2.6 shows the difference between VPT2 and VPT2+K vibrational frequencies and intensities for pyridyl. It has been shown that planar molecules (like pyridyl) can exhibit more anharmonicity within the CH stretching region ($\approx 3000 \text{ cm}^{-1}$), thereby making resonance treatments important for vibrational analysis.[99, 145, 147, 148]

2.6 Conclusion

A review of quantum chemical calculations necessary for rotational and vibrational spectroscopy has been presented. Quantum chemical calculations greatly assist experiments in high resolution spectroscopy. For accurate simulated rotational spectra, the molecular Hamiltonian requires vibrationally corrected rotational constants, centrifugal distortion interactions, and all spin angular momenta sources. A description of the vibrational Hamiltonian was also discussed, which included the harmonic and anharmonic approximation for calculating vibrational energy levels. Second-order vibrational perturbation theory (VPT2) and resonance treatments with VPT2+K were described. Chapter 3 presents an in-depth analysis of pyridyl radicals, which includes all calculations presented in this chapter.

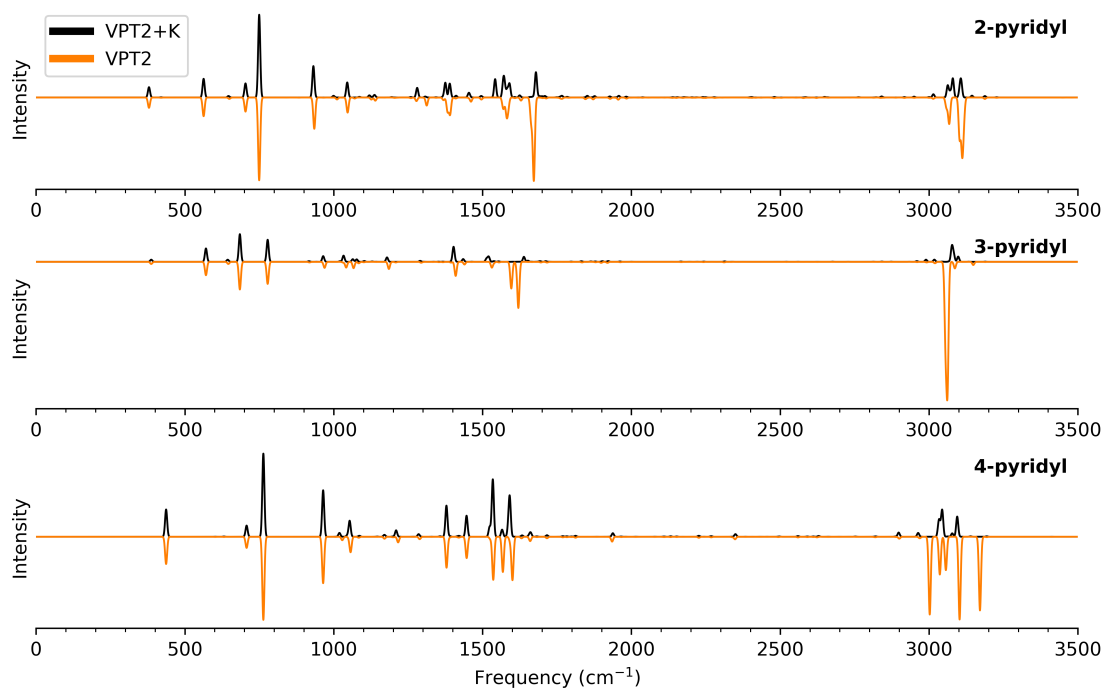


Figure 2.6: Comparison of VPT2 and VPT2+K vibrational frequencies (MHz) and intensities (km/mol) for 2-, 3-, and 4-pyridyl, convolved to 5 cm^{-1} .

Chapter 3

Rotational and Vibrational Spectra of the Pyridyl Radicals: A Coupled-Cluster Study

The following is adapted from the published article: Rotational and Vibrational Spectra of the Pyridyl Radicals: A Coupled-Cluster Study Kelly S. Meyer, John H. Westerfield, Sommer L. Johansen, Jasmine Keane, Anna C. Wannemacher, and Kyle N. Crabtree *The Journal of Physical Chemistry A* Article 2022 126 (20), 3185 – 3197 DOI: 10.1021/acs.jpca.2c01761

3.1 Abstract

Pyridyl is a prototypical nitrogen-containing aromatic radical that may be a key intermediate in the formation of nitrogen-containing aromatic molecules under astrophysical conditions. On meteorites, a variety of complex molecules with nitrogen-containing rings have been detected with non-terrestrial isotopic abundances, and larger nitrogen-containing polycyclic aromatic hydrocarbons (PANHs) have been proposed to be responsible for certain unidentified infrared emission bands in the interstellar medium. In this work, the three isomers of pyridyl (2-, 3-, and 4-pyridyl) have been investigated with coupled cluster methods. For each species, structures were optimized at the CCSD(T)/cc-pwCVTZ level of theory and force fields were calculated at the CCSD(T)/ANO0 level of theory. Second-order vibra-

tional perturbation theory (VPT2) was used to derive anharmonic vibrational frequencies and vibrationally-corrected rotational constants, and resonances among vibrational states below 3500 cm^{-1} were treated variationally with the VPT2+K method. The results yield a complete set of spectroscopic parameters needed to simulate the pure rotational spectrum of each isomer, including electron-spin, spin-spin, and nuclear hyperfine interactions, and the calculated hyperfine parameters agree well with the limited available data from electron paramagnetic resonance spectroscopy. For the handful of experimentally-measured vibrational frequencies determined from photoelectron spectroscopy and matrix isolation spectroscopy, the typical agreement is comparable to experimental uncertainty. The predicted parameters for rotational spectroscopy reported here can guide new experimental investigations into the yet-unobserved rotational spectra of these radicals.

3.2 Introduction

Pyridyl ($c\text{-C}_5\text{H}_4\text{N}$) is a prototypical nitrogen-containing aromatic radical involved in complex chemical processes in terrestrial and astrochemical environments. The amount of nitrogen-containing aromatics present during combustion processes has a significant impact on NOx emissions; this is particularly important in the combustion of biomass, where nitrogen content can be relatively high.[149–152] Pyridyl is a key intermediate in the oxidation and thermal decomposition of pyridine, a model compound for fuel-nitrogen, and a detailed understanding of its reactivity is essential to accurate combustion models.[153–155] Pyridine pyrolysis has also been shown to proceed through pyridyl intermediates,[156–158] and it has been suggested that the specific pyridyl isomer may influence the degree of gas-phase products versus soot formation.[158]

Pyridyl is also a potential intermediate in the formation of nitrogen-containing polycyclic aromatic hydrocarbons (PANHs) in space.[22] Aromatic features from PAHs have been linked to unidentified infrared (UIR) emission bands in the range of $3 - 20 \mu\text{m}$ ($3500 - 300 \text{ cm}^{-1}$).[2, 29–32, 43, 159, 160] Among the bands, the $6.2 \mu\text{m}$ feature has been proposed to indicate the incorporation of at least one nitrogen in the aromatic system; however, a unique identification of the specific molecules responsible for the UIRs remains elusive.[31, 161, 162] More recently, aromatic molecules have also been identified in cold molecular clouds. Towards TMC-1, the GOTHAM and ARKHAM surveys have detected benzonitrile and indene; the former contains a CN attached to an aromatic ring and the latter is a two-ring aromatic system.[34, 163]

Within our solar system, small nitrogen-containing molecules (NH_3 , CH_3CN , C_2N_2 , HC_3N) and the aromatic molecule benzene have been detected in Titan’s atmosphere by the ion neutral mass spectrometer onboard the Cassini-Huygens spacecraft[45, 48, 164]. Photochemical models predict PAH/PANHs and other complex N-bearing molecules are precursors for the production of haze particles in the lower atmosphere of Titan.[49, 50, 165, 166] Radical-driven chemical reactions involving aliphatic/aromatic systems with nitrogen and simple unsaturated hydrocarbons could be necessary for the formation of larger PANHs in

these environments.[23, 167]

Carbonaceous chondrite meteorites, such as Murchison,[63, 66, 69, 168, 169] show diverse populations of prebiotic molecules including nucleobases, amino acids, and other complex organic molecules (COMs)[61, 170] that are isotopically enriched in ^{13}C , ^{15}N and deuterium (D) relative to terrestrial isotopic ratios, suggesting a possible non-terrestrial origin.[60, 67, 70, 171] Many of the organic molecules contain the pyridyl moiety within their structures and their formation pathways are thought to involve radicals, potentially via photo-processes in astrophysical ices or through barrierless gas-phase reactions in cold molecular clouds (or a combination of both).[1] In the condensed phase, laboratory studies of astrophysical ice analogs have shown that nitrogen containing biological molecules, such as amino acids, can form through UV irradiation of ices containing pyrimidine and/or purine along with other small molecules (H_2O , NH_3 , CH_4).[172, 173] Astrochemical models which include gas-grain processes have also shown the production of COMs (CH_3CN , CH_3OH) from radical driven chemical reactions in ices.[174] In the gas phase, pyridyl has been shown to form the PANHs 1,4-dihydroquinoline ($\text{C}_9\text{H}_9\text{N}$) and 1,4-dihydroisoquinoline ($\text{C}_9\text{H}_9\text{N}$) under single collision conditions with 1,3-butadiene (C_4H_6) or vinylacetylene (C_4H_4).[21, 175] Theoretical potential energy surfaces (PESs) suggest that these reactions are barrierless.

Despite the importance of the pyridyl radical, little experimental spectroscopy is available. The three isomers of pyridyl (2-, 3-, and 4-pyridyl) were first detected by ESR spectroscopy, revealing that they are σ -type radicals with the unpaired electron localized in an *sp*-hybrid orbital on the carbon that is missing a hydrogen atom.[176–178] Initially, the ESR spectrum of 2-pyridyl was generated by γ -irradiation of pyridine at 77 K and a single experimental ^{13}C Fermi contact term was determined.[179] Later, all three radicals were produced by dissociative electron capture in a 4 K Ar matrix, and ESR measurements yielded H and N hyperfine coupling terms.[177, 180] The first ab initio molecular orbital studies aimed to interpret initial ESR spectroscopy measurements calculated structures, dipole moments, relative energies, and hyperfine parameters using Restricted open-shell Hartree-Fock (ROHF) and Unrestricted Hartree-Fock (UHF) methods.[181, 182] Later, Density Function

Theory (DFT) methods were used to obtain more accurate structures in order to perform a vibrational analysis of the radicals.[183–187] A small subset of experimental fundamental vibrational frequencies for the isomers were obtained in a 10 K Ar matrix after flash vacuum photolysis of iodopyridines or azopyridines.[188] In the gas phase, another set of experimental frequencies for the isomers were determined via photoelectron spectroscopy of cryogenically cooled pyridinide anions ($C_5H_4N^-$).[189] The experimental work was limited to frequencies below 1600 cm^{-1} and therefore did not cover the fundamental CH stretching modes.

Here, a theoretical investigation of 2-, 3-, and 4-pyridyl was carried out using coupled-cluster (CC) methods, with the aim of providing precise structures and spectroscopic parameters relevant for high-resolution rotational/rovibrational spectroscopy. Prior studies have used CC methods only for calculating single point energies at DFT-optimized structures. This work provides fully optimized CC structures, parameters for rotational spectroscopy including centrifugal distortion, spin-rotation, spin-spin, and quadrupole coupling tensors, and vibrational properties evaluated using second order vibrational perturbation theory (VPT2) with variational corrections (VPT2+K). The results agree qualitatively with prior theoretical calculations, and the spectroscopic parameters obtained here can be used to simulate and analyze rotational and (ro)vibrational spectra at high resolution.

3.3 Methods

Calculations were performed with a development version of the CFOUR program system [190], and employed an unrestricted Hartree-Fock (UHF) reference wave function with the coupled cluster (CC) method. The CC method has shown to be reliable and highly accurate for calculating spectroscopic parameters for rotational spectroscopy and rovibrational spectroscopy.[78, 79] For our starting reference structure, we used previously published DFT results and optimized them using coupled cluster singles and doubles with a perturbative treatment of the triple excitations including all electrons with the correlation consistent polarized weighted core valence triple zeta Dunning style basis set (ae-CCSD(T)/cc-pwCVTZ) with all electrons correlated.[21, 88] Each radical was verified to converge to a doublet state

(spin expectation values $\langle S^2 \rangle = 0.737, 0.735,$ and $0.736,$ for 2-, 3-, and 4-pyridyl, respectively). First-order properties were calculated at this level of theory, including electronic energies, equilibrium rotational constants (A_e, B_e, C_e), dipole moment projections (μ_a, μ_b), Fermi contact terms (a_F), spin-spin interaction tensors (T_{aa}, T_{bb}, T_{cc}) for H and N nuclei, and nuclear quadrupole tensors for the N nuclei ($\chi_{aa}, \chi_{bb}, \chi_{cc}$).

Electronic spin-rotation tensors [96] and force fields were calculated with frozen-core methods. For this purpose, a second reference structure was optimized at frozen-core CCSD(T) (fc-CCSD(T)) using the atomic natural orbital (ANO0)[89] basis set. Harmonic (ω) and anharmonic (ν) vibrational frequencies and intensities were derived from quadratic, cubic, and appropriate subset of quartic force constants calculated at fc-CCSD(T)/ANO0 using second order vibrational perturbation theory (VPT2).[99, 191] Resonances among low-lying vibrational levels were treated variationally using the GUINEA module of CFOUR 2.1.[190] Further details about the resonance treatment are discussed in the Vibrational Analysis section. Ground state rotational constants (A_0, B_0, C_0) and relative energies include corrections from the fc-CCSD(T)/ANO0 VPT2 zero-point vibrational calculations. The SP-CAT program was used to simulate the rotational spectra of the vibrationally-corrected rotational constants and fine/hyperfine coupling terms described above.[192]

3.4 Results and Discussion

3.4.1 Ground State Energies and Optimized Geometries

Table 3.1 shows the relative energy ordering for the three radicals at the ae-CCSD(T)/cc-pwCVTZ optimized geometry including zero-point energy evaluated at fc-CCSD(T)/ANO0. Consistent with previous DFT studies, 2-pyridyl ($C_s, {}^2A'$) is the lowest energy isomer, followed by 4-pyridyl ($C_{2v}, {}^2A_1, +17.33$ kJ/mol) and 3-pyridyl ($C_s, {}^2A', +23.33$ kJ/mol). The three isomers are σ -type radicals with spin density primarily located at the site of the “missing” hydrogen atom.[177, 179, 180, 193] The stability of 2-pyridyl is attributed to the interaction between the N atom lone pair and the radical center, which is also evident from the Fermi contact terms and spin densities reported in the following sections.[193]

Table 3.1 also contains the bond lengths and the bond angles corresponding to the ae-CCSD(T)/cc-pwCVTZ calculated minimum energy structures for 2-, 3-, and 4-pyridyl, as well as experimental values for pyridine based on the microwave structure for comparison.[194] For all three radicals, the bond lengths and bond angles differ from previous DFT studies at most by 9 mÅ and 0.8°.[21, 193] Relative to pyridine, the main structural differences in pyridyl occur at the radical site, and consistent with prior studies, reflect the origin of the additional relative stability of 2-pyridyl. The bond angles at the radical site all open up, but the increase for 3- and 4-pyridyl (angles C2-C3-C4 and C3-C4-C5, respectively) is 2° greater than that of the N1-C2-C3 bond angle for 2-pyridyl. Likewise, the C-C bonds adjacent to the radical site for 3- and 4-pyridyl all decrease by approximately 20 mÅ, while for 2-pyridyl, the C-N bond length decreases by 58 mÅ (the C-C bond length is nearly unchanged).

3.4.2 Spectroscopic Parameters

3.4.2.1 Rotational Constants and Vibration-Rotation Interactions

The ae-CCSD(T)/cc-pwCVTZ equilibrium rotational constants A_e , B_e , and C_e for each radical are shown in Table 3.2. Table 6.3 shows the ground state rotational constants A_0 , B_0 , and C_0 which were determined by adding fc-CCSD(T)/ANO0 vibration-rotation interaction terms ($A_e - A_0$, etc.) to the ae-CCSD(T)/cc-pwCVTZ equilibrium constants. The zero-point corrected inertial defects are reported in Table 3.2 and all three isomers show small, positive values indicating the treatment of anharmonicity is adequate.[195] 2-, 3-, and 4-pyridyl are asymmetric tops ($\kappa = 0.61, 0.52, 0.72$) and the calculated dipole moment projections onto the molecules' principal axes (Table 6.3) show that the rotational spectra of the three radicals are markedly different. The spectrum of 3-pyridyl is mostly *a*-type ($\mu_a = 1.90$ D, $\mu_b = 0.10$ D), that of 4-pyridyl is *b*-type ($\mu_b = 1.16$ D), and 2-pyridyl has strong *a*- and *b*-type spectra ($\mu_a = 1.66$ D, $\mu_b = 2.21$ D).

3.4.2.2 Spectroscopic Parameters for Rotational and Rovibrational Spectroscopy

Diagonal elements of the spin-spin (T_{aa} , T_{bb} , T_{cc}) and ^{14}N ($I=1$) nuclear quadrupole tensors (χ_{aa} , χ_{bb} , χ_{cc}) are shown in Table 6.3. Full spin-spin tensors and N-quadrupole tensors are

Table 3.1: ae-CCSD(T)/cc-pwCVTZ equilibrium geometries (in Ångstrom and degrees) and relative energies in kJ/mol, including fc-CCSD(T)/ANO0 zero-point vibrational energy for pyridyl radicals.

	Pyridine ^a	2-pyridyl	3-pyridyl	4-pyridyl
N1-C2	1.338	1.280	1.341	1.331
C2-C3	1.394	1.390	1.374	1.397
C3-C4	1.392	1.384	1.370	1.369
C4-C5	1.392	1.397	1.393	
C5-C6	1.394	1.380	1.389	
C6-N1	1.338	1.349	1.333	
C2-H2	1.087		1.081	1.084
C3-H3	1.083	1.079		1.080
C4-H4	1.082	1.083	1.081	
C5-H5	1.082	1.080	1.082	
C6-H6	1.087	1.082	1.083	
∠C2-N1-C6	116.9	117.8	117.7	117.5
∠N1-C2-C3	123.8	127.2	120.1	124.2
∠N1-C6-C5	123.8	121.3	124.4	
∠N1-C6-H6	116.0	116.9	115.7	116.3
∠C2-C3-C4	118.5	115.0	123.7	115.1
∠C6-C5-C4	118.5	119.0	118.3	
∠N1-C2-H2	116.0		117.0	
∠C2-C3-H3	120.1	122.5		121.0
∠C6-C5-H5	120.1	120.1	120.5	
∠C3-C4-C5	118.4	119.6	115.8	123.9
∠C3-C4-H4	120.8	120.2	122.6	
∠C5-C4-H4	120.8	120.2	121.6	
Rel. Energy		0.00	+23.33	+17.33

^a Experimental values derived by microwave spectroscopy.[194] Uncertainties are between ± 0.002 and ± 0.006 Å for bond length measurements and between $\pm 0.02^\circ$ and $\pm 0.04^\circ$ for bond angles.

Table 3.2: ae-CCSD(T)/cc-pwCVTZ equilibrium rotational constants, dipole moment projections, and electronic energies.

Parameter	2-pyridyl	3-pyridyl	4-pyridyl
A_e (MHz)	6609.12	6684.14	6478.66
B_e (MHz)	5921.23	5819.10	6014.95
C_e (MHz)	3123.15	3110.85	3119.10
$A_e - A_0^a$ (MHz)	43.10	44.09	37.55
$B_e - B_0^a$ (MHz)	40.89	38.22	43.34
$C_e - C_0^a$ (MHz)	22.27	21.73	21.57
$ \mu_a $ (D)	1.66	1.90	0.00
$ \mu_b $ (D)	2.21	0.10	1.16
Δ_0^b (amu \AA^2)	0.07	0.07	0.06

^afc-CCSD(T)/ANO0

^bInertial defect: $I_c - I_a - I_b$

reported in the Supporting Information. To the best of our knowledge, no values have been previously reported for these spectroscopic parameters. Previous microwave studies have established that the ^{14}N quadrupole coupling constants of pyridine are $\chi_{aa} = -4.88 \pm 0.04$ MHz, $\chi_{bb} = 1.43 \pm 0.03$ MHz, and $\chi_{cc} = 3.45 \pm 0.02$ MHz.[196] The analogous values for the pyridyl radicals are calculated to be similar to those of pyridine after accounting for the rotation of the principal axes relative to the heavy atom framework upon the removal of H2, H3, or H4, as denoted in Table 3.1.

Fermi contact (a_F) constants for ^1H , ^{13}C , ^{14}N are shown in Tables 3.4. The Fermi contact term gives direct information about the electron spin density at each $I > 0$ nucleus[197]; as σ -type radicals, each isomer has a large ^{13}C a_F value at the radical center. The calculated ^{13}C a_F value of 474 MHz for 2-pyridyl is quite close to the experimental value of 477 MHz derived from ESR measurements. [177] For historical context, values determined from the Intermediate Neglect of Molecular Orbitals (INDO) theory[198], a semi-empirical method

Table 3.3: Calculated rotational spectroscopic parameters of 2-, 3-, and 4-pyridyl, in MHz.

Parameter	2-pyridyl	3-pyridyl	4-pyridyl
A_0	6566.03	6640.05	6441.11
B_0	5880.35	5780.88	5971.62
C_0	3100.88	3089.11	3097.53
$10^{-4}\Delta_N$	6.98	6.62	6.63
$10^{-4}\Delta_{NK}$	1.69	2.54	0.65
$10^{-4}\Delta_K$	7.53	7.73	10.10
$10^{-4}\delta_N$	2.90	2.73	2.73
$10^{-4}\delta_K$	8.36	8.55	6.85
ϵ_{aa}	23.88	10.52	10.01
ϵ_{bb}	3.79	2.96	2.16
ϵ_{cc}	-6.15	-5.17	-4.64
χ_{aa}	-3.54	-3.98	1.52
χ_{bb}	0.75	0.58	-4.91
χ_{cc}	2.79	3.40	3.38
$a_F(\text{N1})$	93.80	-5.18	8.08
$T_{aa}(\text{N1})$	-1.75	0.74	-1.10
$T_{bb}(\text{N1})$	4.64	5.91	-0.14
$T_{cc}(\text{N1})$	-2.89	-6.65	1.24
$a_F(\text{H2})$		8.83	31.03
$T_{aa}(\text{H2})$		12.42	1.30
$T_{bb}(\text{H2})$		-5.80	1.92
$T_{cc}(\text{H2})$		-6.61	-3.21
$a_F(\text{H3})$	0.96		38.21
$T_{aa}(\text{H3})$	14.53		13.31
$T_{bb}(\text{H3})$	-7.02		-6.70
$T_{cc}(\text{H3})$	-7.51		-6.62
$a_F(\text{H4})$	29.54	39.85	
$T_{aa}(\text{H4})$	0.45	12.55	
$T_{bb}(\text{H4})$	2.36	-6.00	
$T_{cc}(\text{H4})$	-2.81	-6.56	
$a_F(\text{H5})$	0.84	18.08	
$T_{aa}(\text{H5})$	-2.38	0.93	
$T_{bb}(\text{H5})$	4.04	2.41	
$T_{cc}(\text{H5})$	-1.66	-3.34	
$a_F(\text{H6})$	3.19	2.66	
$T_{aa}(\text{H6})$	0.30	-1.77	
$T_{bb}(\text{H6})$	4.42	3.65	
$T_{cc}(\text{H6})$	-4.72	-1.88	

Table 3.4: ae-CCSD(T)/cc-pwCVTZ ^1H , ^{13}C , and ^{14}N Fermi contact terms, in MHz.

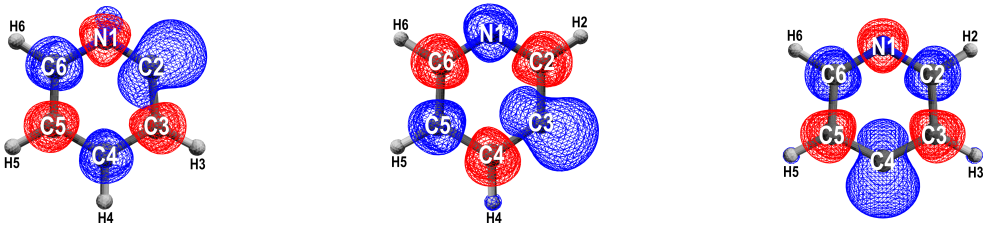
Parameter	2-pyridyl			3-pyridyl			4-pyridyl		
	^a INDO[177]	ESR[177]	This Work	^a INDO[177]	ESR[177]	This Work	^a INDO[177]	ESR[177]	This Work
$a_F(\text{N1})$	82	81±3	94	3		5	3		8
$a_F(^{13}\text{C2})$	665	477	474			27			17
$a_F(^{13}\text{C3})$			89			347			17
$a_F(^{13}\text{C4})$			12			20			348
$a_F(^{13}\text{C5})$			9			16			17
$a_F(^{13}\text{C6})$			61			12			17
$a_F(\text{H2})$				30	22±6	9	24	28±3	31
$a_F(\text{H3})$	16		1				51	53±3	38
$a_F(\text{H4})$	24	28±3	30	53	53±3	40			
$a_F(\text{H5})$	17	17±3	1	10	22±3	18	51	53±3	38
$a_F(\text{H6})$	16		3	23		3	24	28±3	31

^a Intermediate Neglect of Molecular Orbitals[198]

widely used prior to the more accurate ab initio methods used today, are provided here. Additional a_F H and N values are available for comparison, showing the same general trends in relative magnitudes of parameters as observed in experiments. Calculated spin densities (Table 3.5) agree with previous (U)B3LYP calculations that indicate the spin density is primarily located on the nominal radical center, with 2-pyridyl showing partial delocalization on the N atom. [193] By contrast, spin densities calculated previously with the (U)M06 functional [193] yielded more localization compared with the CCSD(T) spin densities calculated here.

The C_{2v} structure for 4-pyridyl imposes restrictions on the symmetry of the wavefunction from Fermi-Dirac statistics. The total internal symmetry, and therefore the product of rovibronic (Γ_{rve}) and nuclear spin (Γ_{nspin}) symmetries, must be B_1 or B_2 . The representation of the nuclear spin wavefunction in the $C_{2v}(M)$ molecular symmetry group is $\Gamma_{ns} = 10A_1 \oplus 6B_1$. In the ground vibronic state, the $K_a + K_c = \text{even}$ (A_1, A_2) rotational states must combine with the B_1 nuclear spin functions and the $K_a + K_c = \text{odd}$ (B_1, B_2) must combine with the A_1 nuclear spin functions yielding statistical weights of 3:5. The simulated rotational spectrum for 4-pyridyl shown below includes these statistical weights.

Table 3.5: Mulliken analysis of ae-CCSD(T)/cc-pwCVTZ spin densities ($\alpha = \text{blue}$, $\beta = \text{red}$).



Atom	2-pyridyl			3-pyridyl			4-pyridyl		
	This Work	(U)B3LYP[193]	(U)M06[193]	This Work	(U)B3LYP[193]	(U)M06[193]	This Work	(U)B3LYP[193]	(U)M06[193]
N1	0.14	0.11	0.07	0.03	0.09	0.08	0.04	-0.01	-0.03
C2	0.79	0.80	0.86	0.02			-0.02		
C3	0.06			0.91	0.89	0.98	0.01		
C4	-0.04			0.01			0.92	0.92	0.98
C5	0.04			-0.01					
C6	-0.01			0.02					
H2				0.00			0.02		
H3	-0.01						0.01		
H4	0.02			0.01					
H5	0.00			0.01					
H6	0.00			0.00					

Electronic spin-rotation tensors were calculated at fc-CCSD(T)/ANO0 using the optimized geometries at the same level of theory.[96] The spin-rotation interaction contributes to line splittings in pure rotational spectra, and the diagonal elements of the tensors (ϵ_{aa} , ϵ_{bb} , ϵ_{cc}) (Table 6.3) were used for the simulated spectra. The full tensors are in the Supporting Information. To our knowledge, these spin-rotation tensors have not been previously calculated and there are no experimental values present for comparison.

3.5 Simulated Rotational Spectra

Figure 3.1 shows the simulated rotational spectra of 2-, 3-, and 4-pyridyl using the spectroscopic parameters from Tables 3.2 and 6.3, which can be used to guide an experimental search. The spectrum is simulated up to 100 GHz at $T = 5$ K for F values up to 20. The pyridyl isomers are easily distinguishable from one another due to the differences in their rotational constants and hyperfine splitting patterns. 4-pyridyl has the largest κ value of \approx

0.7, exhibiting more oblate character than either 2-pyridyl ($\kappa \approx 0.6$) or 3-pyridyl ($\kappa \approx 0.5$). Owing to the relative magnitudes of the total dipole moments, the spectrum of 4-pyridyl is considerably weaker than either of the other two isomers. Nuclear spin statistical weights are included in the simulation for 4-pyridyl. SPCAT input files (.int and .var) for all three radicals are provided in the Supporting Information.

In Figure 3.2, the fundamental transitions $N' - N'' = 1 - 0$ are shown in black for each radical convolved to 50 kHz in order to better represent experimental line widths in FTMW spectroscopy. The hyperfine splitting patterns for the a-type transitions in 2- and 3-pyridyl are condensed around a region spanning approximately 5 MHz, whereas the b-type transitions for 2-, 3-, and 4-pyridyl are spread over a 20 MHz region. 4-pyridyl's b-type spectrum exhibits broad splitting primarily due to the H3/H5 spin-spin coupling. The dominant source of splitting in the spectra of 2- and 3-pyridyl also primarily arises from the spin-spin coupling from the hydrogens, particularly from H4. However, the magnitude of the splitting is also affected by the spin-rotation interaction. Nitrogen quadrupole splitting is somewhat smaller than the others and does not contribute substantially to the overall spread of the line distribution.

Detailed assignment of the hyperfine structure of these radicals would be difficult because of the complicated splitting patterns at low N ; however, as N increases, the hyperfine structure collapses into a pure spin-rotation doublet. Figure 3.3 shows selected spectra of the R -branch b-type transitions for selected spectral progressions of 2-pyridyl. By 200 GHz, most of the structure has completely collapsed, approaching the high- N limit, and the splitting is described purely by the spin-rotation terms. Similar depictions of hyperfine collapse for 3- and 4-pyridyl are provided in the Supporting Information. For this reason, the millimeter wave portion of the rotational spectrum may be most amenable for laboratory investigations. Moreover, potential astronomical searches for complex nitrogen- and hydrogen-containing radicals such as these should likewise be carried out with millimeter-wave telescopes rather than in the centimeter band to avoid excessive spectral line dilution.

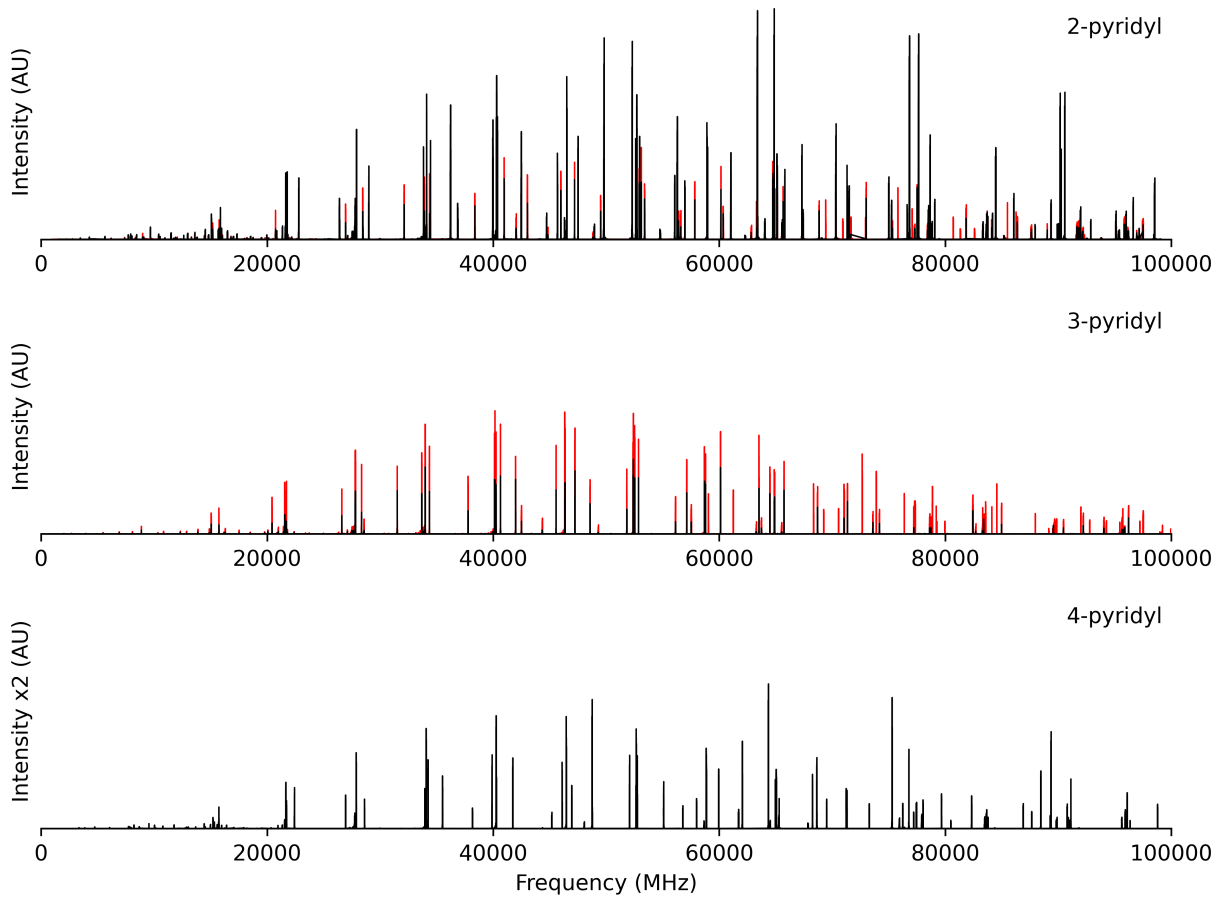


Figure 3.1: Simulated rotational spectra from top to bottom of 2-, 3-, 4-pyridyl calculated with spectroscopic parameters from Tables 3.2 and 6.3. Simulated at $T = 5$ K.
 red: a-type spectrum; black: b-type spectrum

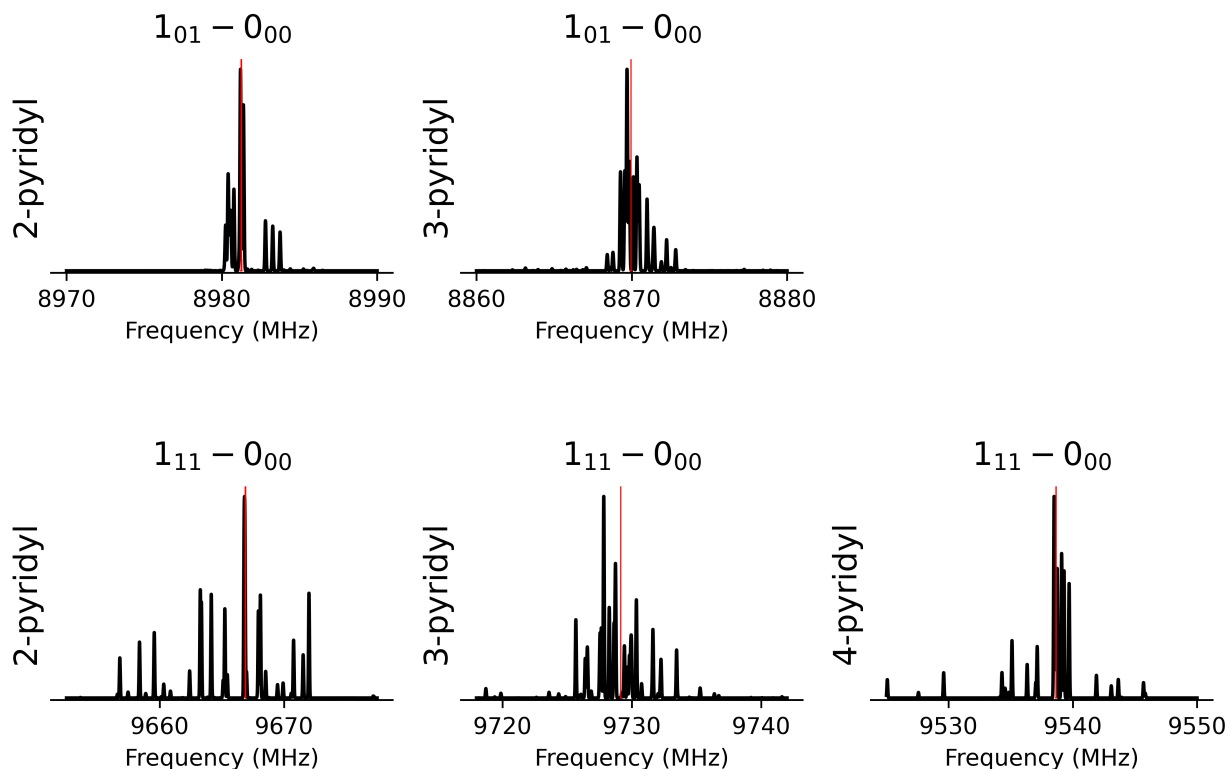


Figure 3.2: Hyperfine (black) and spin-free (red) structure of fundamental transitions for 2-, 3-, and 4-pyridyl using spectroscopic parameters in Table 6.3. Convolved to a linewidth of 50 kHz.

3.6 Vibrational Analysis

From force constants evaluated at the the fc-CCSD(T)/ANO0 optimized geometries, the harmonic (ω) frequencies and intensities were calculated with the same method and basis set. These values are available in Supporting Information along with comparisons to previous DFT calculations. The quadratic, cubic, and appropriate quartic force constants were used to calculate the anharmonic frequencies (ν) and intensities for the 24 fundamental vibrational modes of each radical using second order vibrational perturbation theory (VPT2). In addition, energy levels of vibrational states with up to three quanta of excitation were calculated. Given the large number of vibrational modes for the pyridyl radicals, potential resonances among states in the VPT2 treatment with a harmonic energy below 3500 cm^{-1} were identified and the states involved were treated variationally.

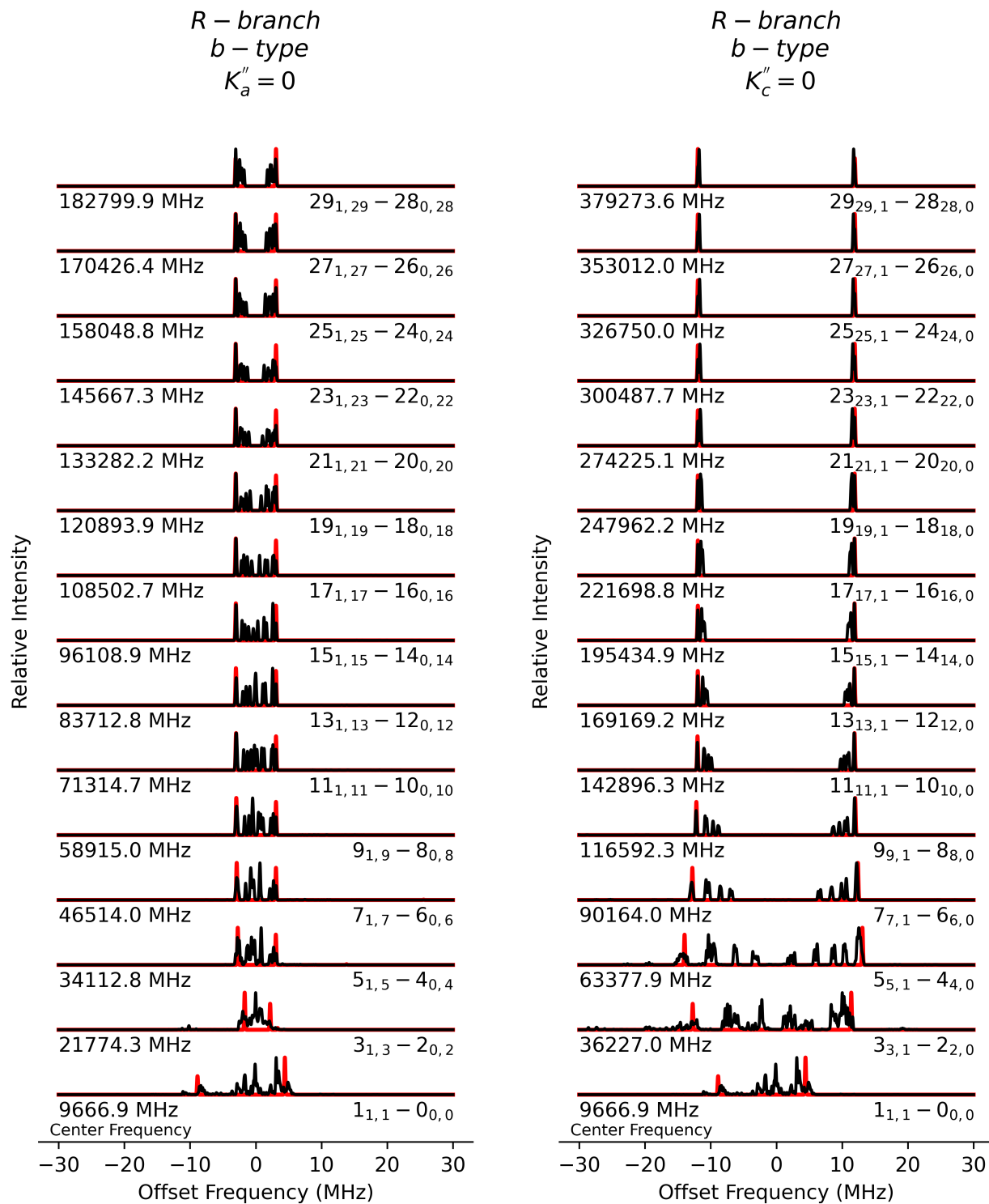


Figure 3.3: Hyperfine structure of 2-pyridyl with increasing N . R-branch b-type transitions with $K_a'' = 0$ and $K_c'' = 0$ for even N'' . Simulated at $T = 50$ K and convolved to a linewidth of 100 kHz.
 black: includes all spectroscopic parameters from Tables 3.2 and 6.3
 red: includes only spin-rotation terms

As discussed in Ref. 99, the choice of which states to treat variationally is an important consideration in any resonance-corrected VPT2 approach. Here, we began by searching for Fermi resonances using a Martin Test[199] with a threshold of 10 cm^{-1} between states with an energy difference of 200 cm^{-1} . Potential Darling-Dennison resonances[94, 146] were flagged if two appropriate states within 100 cm^{-1} in harmonic energy were coupled by a force constant of 30 cm^{-1} or greater. Additionally, any state with multiple quanta of excitation was included in the variational treatment if its transition intensity with respect to the ground vibrational state exceeded 1 km/mol . This yielded an initial set of a small number of states that were then treated variationally with the GUINEA program.[99, 148] Calculations were then repeated with lower thresholds to include potential resonances involving additional states. The energies of states in common between the two calculations were compared, looking for large differences. At the final thresholds used here (0.1 cm^{-1} for the Martin test and 2 cm^{-1} for the Darling-Dennison force constant), the differences from the previous iteration were generally of order 1 cm^{-1} . The combination of VPT2 with extensive treatment of resonances is denoted VPT2+K. Input GUINEA files for 2-, 3-, and 4-pyridyl as well as the full list of vibrational states with up to 3 quanta are provided in the Supporting Information. For this section, we adopt the convention of labeling states by $n_i^{v_i}n_j^{v_j}$, where n_i is the Herzberg mode number and v_i is the number of quanta in mode n_i (only modes with $v_i > 0$ are listed).

The variational treatment included 185 states for 2-pyridyl (135 A' , 50 A''), 181 states for 3-pyridyl (125 A' , 56 A''), and 115 states for 4-pyridyl (58 A_1 , 9 A_2 , 11 B_1 , 37 B_2). Tables A.6, A.7, and A.8 show the calculated harmonic and VPT2+K frequencies and intensities for fundamental vibrational modes along with previous experimental values from photoelectron spectroscopy of $\text{C}_5\text{H}_4\text{N}^-$ [189] and Ar matrix isolation spectroscopy[188]. Additional comparisons of this work's calculations with tentatively-assigned combination and overtone bands from photoelectron spectroscopy are also reported in the Supporting Information. Figure 3.4 shows the fc-CCSD(T)/ANO0 simulated VPT2+K infrared spectra for 2-, 3- and 4-pyridyl ranging from $300 - 3500\text{ cm}^{-1}$, convolved to a linewidth of 5 cm^{-1} .

The CH stretching modes for all three species are heavily affected by resonances in the

Table 3.6: 2-pyridyl fc-CCSD(T)/ANO0 harmonic and VPT2+K anharmonic vibrational frequencies (cm^{-1}) and intensities (km/mol).

Mode ^a	Sym.	This Work				Experiment	
		ω	Int.	ν (VPT2+K)	Int. (VPT2+K) ^e	Ref. 189 ^b	Ref. 188 ^{ce}
ν_1	A'	3236.98	3.02	*3108.16	*7.16(16)		
ν_2	A'	3226.80	10.74	^d *3104.28	*4.71(10)		
ν_3	A'	3202.11	13.21	^d *3079.91	*10.37(23)		
ν_4	A'	3193.12	1.99	^d *3071.29	*3.05(7)		
ν_5	A'	1675.97	41.87	^d *1679.29	*13.86(31)		
ν_6	A'	1610.62	17.79	^d *1542.26	*10.05(22)	1536[6]	
ν_7	A'	1492.85	2.24	*1455.21	*1.50(3)	1463[5]	
ν_8	A'	1418.76	17.52	^d *1374.95	*8.09(18)	1390[5]	
ν_9	A'	1318.28	5.66	*1280.35	*5.29(12)		
ν_{10}	A'	1236.88	0.33	*1194.69	*0.22(0)		
ν_{11}	A'	1155.65	2.49	*1137.03	*1.41(3)	1140	
ν_{12}	A'	1113.27	0.15	*1086.21	*0.37(1)	1088[6]	
ν_{13}	A'	1070.93	8.70	*1045.36	*8.24(18)	1043[5]	1044.3(19)
ν_{14}	A'	1031.91	0.78	*999.38	*0.93(2)	1010[5]	
ν_{15}	A'	949.41	17.82	*931.68	*17.20(38)	951[6]	940.9(45)
ν_{16}	A'	656.78	0.62	*646.46	*0.80(2)	649[5]	
ν_{17}	A'	569.30	10.39	562.90	10.24(23)	568[6]	564.5(33)
ν_{18}	A''	1011.72	0.07	*991.76	*0.07(0)		
ν_{19}	A''	985.83	0.06	*962.60	*0.08(0)		
ν_{20}	A''	900.21	0.07	881.74	0.06(0)		
ν_{21}	A''	762.30	45.26	749.58	45.36(100)		735.1(100)
ν_{22}	A''	712.84	7.96	703.61	7.72(17)		
ν_{23}	A''	426.56	0.11	419.79	0.13(0)		
ν_{24}	A''	387.23	5.73	379.35	5.65(12)		

^a Normal modes as numbered in the Herzberg convention. ^b Photoelectron spectroscopy. Uncertainty in brackets. ^c Ar matrix isolation spectroscopy. ^d State is heavily mixed. Refer to SI for more accurate assignments. ^e Relative intensity in parenthesis. * Variationally corrected.

Table 3.7: 3-pyridyl fc-CCSD(T)/ANO0 harmonic and VPT2+K anharmonic vibrational frequencies (cm^{-1}) and intensities (km/mol).

Mode ^a	Sym.	This Work				Experiment	
		ω	Int.	ν (VPT2+K)	Int. (VPT2+K) ^e	Ref. 189 ^b	Ref. 188 ^{ce}
ν_1	A'	3219.38	5.11	*3097.95	*6.22(19)		
ν_2	A'	3207.76	7.36	*3082.83	*8.30(25)		
ν_3	A'	3203.65	11.12	^d *3076.75	*17.76(54)		
ν_4	A'	3184.90	7.37	^d *3066.65	*0.39(1)		
ν_5	A'	1644.16	11.20	^d *1638.93	*5.93(18)		
ν_6	A'	1576.84	8.22	*1520.65	*5.96(18)	1509[6]	1499.9(33)
ν_7	A'	1470.44	3.29	*1434.86	*3.27(10)		1426.0(11)
ν_8	A'	1437.51	18.60	*1402.61	*17.81(54)		1405.1(94)
ν_9	A'	1323.31	1.07	*1290.32	*1.14(3)		1306.1(3)
ν_{10}	A'	1207.81	4.56	*1179.01	*5.23(16)		1209.1(4)
ν_{11}	A'	1202.53	1.76	^d *1129.14	*0.45(1)		1181.2(4)
ν_{12}	A'	1099.38	6.02	^d *1063.97	*3.11(9)	1085[6]	1084.9(16)
ν_{13}	A'	1067.74	7.66	*1033.03	*7.32(22)	1050[8]	1035.9(24)
ν_{14}	A'	1051.65	0.99	*1021.19	*0.75(2)	1027[8]	1023.7(8)
ν_{15}	A'	985.13	7.14	*964.60	*6.73(21)	974[6]	972.9(30)
ν_{16}	A'	652.89	2.27	*643.79	*2.51(8)	646[6]	646.3(9)
ν_{17}	A'	578.15	15.57	570.73	15.83(48)	568[5]	569.5(71)
ν_{18}	A''	1001.54	0.07	981.51	0.05(0)		
ν_{19}	A''	960.94	0.09	940.58	0.12(0)		
ν_{20}	A''	938.77	0.65	*916.82	*0.74(2)		
ν_{21}	A''	791.35	26.55	778.06	26.13(80)		764.3(60)
ν_{22}	A''	695.82	32.65	684.66	32.75(100)		671.8(100)
ν_{23}	A''	420.72	0.03	414.06	0.04(0)		
ν_{24}	A''	394.49	2.62	386.95	2.54(8)		

^a Normal modes as numbered in the Herzberg convention. ^b Photoelectron spectroscopy. Uncertainty in brackets. ^c Ar matrix isolation spectroscopy. ^d State is heavily mixed. Refer to SI for more accurate assignments. ^e Relative intensity in parenthesis. * Variationally corrected.

Table 3.8: 4-pyridyl fc-CCSD(T)/ANO0 harmonic and VPT2+K anharmonic vibrational frequencies (cm^{-1}) and intensities (km/mol).

Mode ^a	Sym.	This Work				Experiment	
		ω	Int.	ν (VPT2+K)	Int. (VPT2+K) ^d	Ref. 189 ^b	Ref. 188 ^{cd}
ν_1	A_1	3225.14	0.02	*3099.02	*0.02(0)		
ν_2	A_1	3178.16	5.33	*3036.97	*3.48(8)		
ν_3	A_1	1584.90	42.70	*1534.45	*29.73(69)	1509[5]	
ν_4	A_1	1479.06	9.51	*1446.22	*10.96(25)	1445[5]	
ν_5	A_1	1235.51	3.04	*1209.59	*3.33(8)		1439.9(10)
ν_6	A_1	1078.59	8.66	*1053.48	*8.32(19)		1372.3(12)
ν_7	A_1	1047.80	1.28	*1019.19	*2.01(5)	1020[6]	
ν_8	A_1	981.33	22.05	964.45	24.20(56)	969[6]	1052.7(10)
ν_9	A_1	608.26	0.13	*599.86	*0.09(0)	603[6]	
ν_{10}	A_2	1002.35	0.00	983.54	0.00(0)		
ν_{11}	A_2	846.86	0.00	829.94	0.00(0)		1017.4(10)
ν_{12}	A_2	382.83	0.00	374.26	0.00(0)		
ν_{13}	B_1	975.37	0.01	*954.71	*0.01(0)		1031.8(< 1)
ν_{14}	B_1	776.76	43.64	763.58	43.30(100)		
ν_{15}	B_1	717.77	6.11	707.32	5.81(13)		
ν_{16}	B_1	443.21	14.41	436.89	14.19(33)		
ν_{17}	B_2	3224.27	5.51	*3094.54	*10.50(24)		
ν_{18}	B_2	3176.45	21.88	*3044.18	*13.68(32)		
ν_{19}	B_2	1642.08	25.93	*1591.37	*19.25(44)		
ν_{20}	B_2	1408.02	16.87	*1378.52	*15.05(35)		
ν_{21}	B_2	1313.97	1.24	*1285.18	*1.35(3)		1570.9(50)
ν_{22}	B_2	1208.67	1.57	*1170.28	*0.99(2)		1496.8(25)
ν_{23}	B_2	1076.35	0.99	*1045.15	*0.66(2)		
ν_{24}	B_2	639.11	0.12	630.96	0.12(0)		

^a Normal modes as numbered in the Herzberg convention. ^b Photoelectron spectroscopy. Uncertainty in brackets. ^c Ar matrix isolation spectroscopy. Assignments as given in Ref. [188]. ^d Relative intensity in parenthesis. * Variationally corrected.

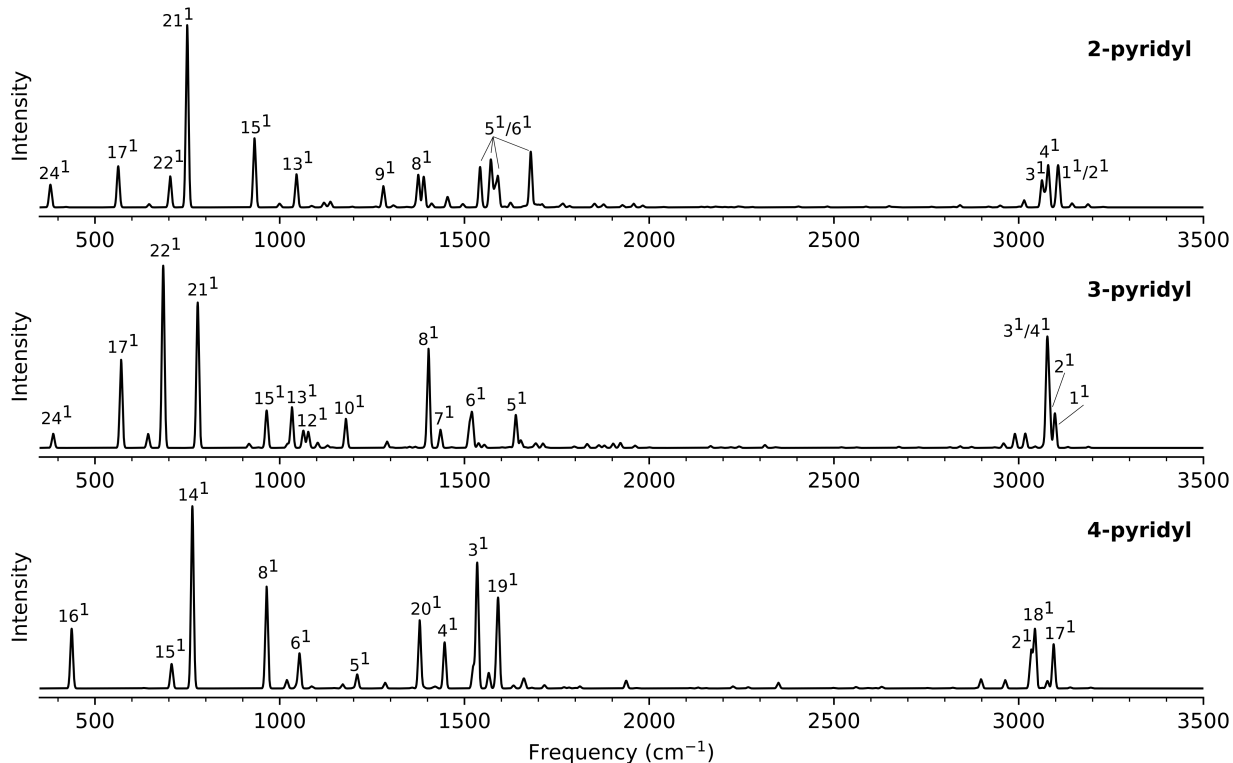


Figure 3.4: Simulated VPT2+K IR spectra of 2-, 3-, and 4-pyridyl convolved to a linewidth of 5 cm^{-1} . Fundamental vibrational modes are labeled for each species. Owing both to state mixing and the simulation linewidth, many peaks also contain contributions from overtones and/or combination bands.

VPT2 treatment. A comparison of the VPT2 spectrum with the VPT2+K spectrum for the regions $1300\text{--}1700\text{ cm}^{-1}$ and $2900\text{--}3200\text{ cm}^{-1}$, is shown in Figure 3.5. For 2-pyridyl, harmonic energies of several 2-quantum states involving combinations of ν_5 , ν_6 , and/or ν_7 lie near those of the the $\nu_1 - \nu_4$ fundamentals giving rise to a complex set of Fermi resonances. Generally, the resonances in the VPT2 treatment artificially increase the intensities of the combination bands and overtones while decreasing those of the fundamentals, and introduce erroneous perturbative frequency corrections in VPT2. The VPT2+K treatment restores the intensities of the fundamentals to values closer to their harmonic intensities, but also reveals heavy mixing among a number of states with substantial intensity borrowing from the forbidden transitions. In Tables A.6-A.8, such heavily mixed states are flagged with a footnote. For instance, in 2-pyridyl the state nominally assigned to 3^1 is better described as

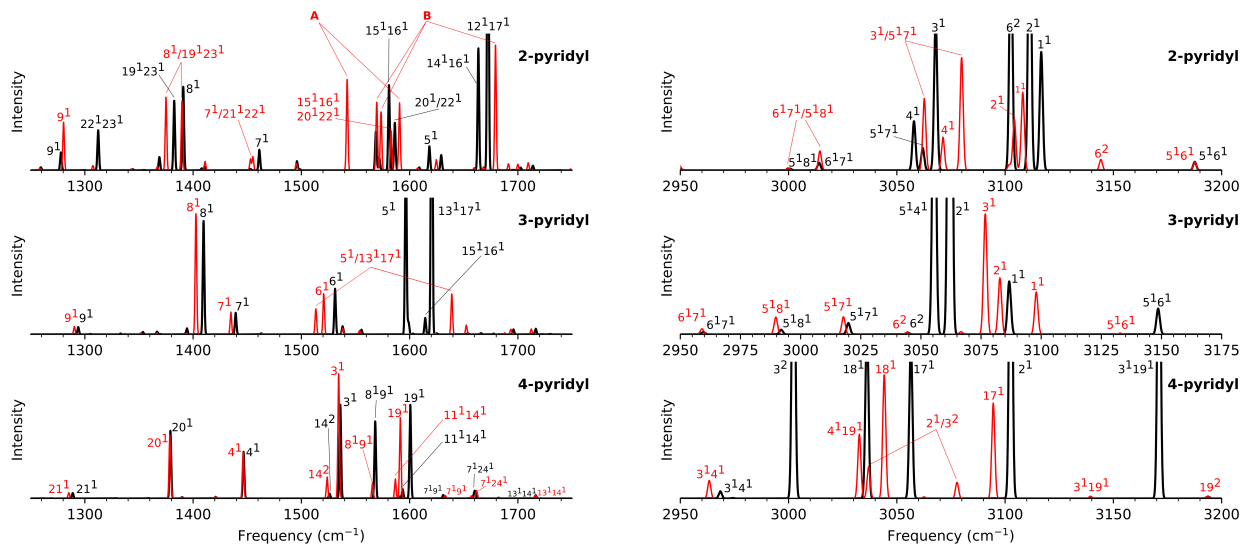


Figure 3.5: Comparison of VPT2+K (red) and VPT2 (black) infrared spectra in the ring deformation regions (left) and C-H stretch (right) regions. Individual transitions are convoluted to a line width of 1 cm^{-1} . Each panel is scaled independently according to the VPT2+K intensity; the VPT2 transitions heavily affected by resonances are cut off. **A**: Mixture of 6^1 , 15^116^1 , 14^117^1 , and 20^122^1 . **B**: Mixture of 5^1 , 12^117^1 , 14^116^1 , 14^117^1 , and 15^116^1 .

30% 3^1 + 25% 2^1 + 13% 5^17^1 + 10% 6^2 with additional minor contributions from 1^1 and 5^16^1 . Likewise, the state nominally assigned to 2^1 is primarily composed of 51% 4^1 + 21% (5^17^1), along with many other states at the $< 10\%$ level. Owing to the strong mixing among these levels, the 5^17^1 combination band (upper state 49% 5^17^1 + 34% 3^1) gains an intensity (6.95 km/mol) comparable to those of the nearby fundamentals, and this can be seen in Figures 3.4 and 3.5. To first order, the 3^1 and 5^17^1 bands form a Fermi-split pair at 3063 and 3079 cm^{-1} . Two other notable features appear in the spectrum: the 6^2 overtone gains intensity from 1^1 and shifts upward in frequency by about 40 cm^{-1} relative to its VPT2 value, and the 6^17^1 and 5^18^1 combination band states are coupled by a Darling-Dennison resonance.

The analogous states in 3-pyridyl are likewise involved in a network of Fermi resonances, also giving rise to intensity errors under standard VPT2 as well as frequency errors of 10–20 cm^{-1} . In particular, the 2^1 fundamental is involved in a Fermi resonance with the 5^17^1 combination band, the latter of which is also coupled to fundamentals 3^1 and 4^1 . In the VPT2

treatment, the intensity of the 2^1 transition is 143 km/mol and that of the ν_3 fundamental is 46 km/mol, considerably greater than their respective harmonic values of 7 and 11 km/mol, respectively. The VPT2+K treatment restores the intensities of these two much closer to their harmonic values, but 3^1 gains intensity from 4^1 through their mutual coupling with 5^17^1 . That said, as a result of the couplings among the aforementioned states, 4^1 is not the leading contribution to any single vibrational level: in Table A.7 the mode listed as 4^1 is better described as 31% 3^1 + 24% 4^1 with several other contributions, while that listed as 3^1 is 40% 3^1 + 29% 4^1 . As a result of intensity borrowing among these states, no strong peak is present in the spectrum corresponding to the 4^1 fundamental.

The C_{2v} symmetry of 4-pyridyl imposes restrictions on which states may be involved in resonances, and also changes the mode numberings in the Herzberg convention relative to 2- and 3-pyridyl. For 2- and 3-pyridyl with C_s symmetry, 17 of the modes are of A' symmetry and the remaining 7 are A'' , the latter of which comprise the majority of the lowest-frequency modes. 4-pyridyl has 9 A_1 modes (2 of which are CH stretches), 3 A_2 modes, 4 B_1 modes, and 8 B_2 modes (2 of which are the remaining CH stretches). Only states with the same symmetry can be coupled. In the CH stretching region, several near-degeneracies in harmonic energies give rise to substantial frequency and intensity errors in VPT2: in particular between $2^1/3^2$ ($\Delta E=8.2$ cm $^{-1}$) and $17^1/3^119^1$ ($\Delta E=2.7$ cm $^{-1}$). In VPT2+K, the 1^1 (A_1) state is mixed with 3^2 and 4^111^2 , causing its frequency to increase by 10 cm $^{-1}$ relative to the VPT2 value; however, the intensity of this transition (VPT2+K: 0.02 km/mol, harmonic: 0.04 km/mol) is negligible. The other CH stretches are all involved in resonances: 2^1 (A_1) is involved in a strong Fermi resonance with 3^2 (ν_3 is analogous to ν_6 in 2- and 3-pyridyl), giving rise to a pair of bands at 3037 and 3078 cm $^{-1}$. Similarly, a Fermi resonance between the B_2 states 18^1 and 4^119^1 generates a strong pair of bands at 3033 and 3044 cm $^{-1}$ which share the intensity of 18^1 . All of these bands are shifted considerably from their VPT2 counterparts as shown in Figure 3.5. As a result of the strong state mixing, the CH stretching region features 5 bands with appreciable intensity, while the harmonic approximation predicts only 3.

The 1250–1750 cm $^{-1}$ region of the spectrum (ring deformation modes) also features com-

plex resonances that result in significant differences between VPT2 and VPT2+K. 2-pyridyl is the most complicated among the three radicals. The 5^1 fundamental is involved in a network of Fermi resonances with 2-quantum states including 12^117^1 , 14^116^1 , 14^117^1 , and 15^116^1 which are further coupled through Darling-Dennison resonances. The strong harmonic intensity of 5^1 is split into three main components at 1570, 1574, and 1679 cm^{-1} , the latter of which is the most intense by about a factor of 2. The 6^1 fundamental is likewise coupled with 15^116^1 and 20^122^1 , yielding a set of three relatively intense transitions at 1542, 1583, and 1591 cm^{-1} . Finally, two comparatively simple 2-state Fermi resonances are observed: one of which couples 7^1 with 21^122^1 yielding a doublet at 1453 and 1455 cm^{-1} , and the other couples 8^1 with 19^123^1 to give a doublet at 1375 and 1390 cm^{-1} . As a result, this region of the spectrum is predicted to contain about twice as many vibrational bands as expected from a simple harmonic picture.

For 3- and 4-pyridyl, the couplings are less extensive in the same spectral region. 3-pyridyl features one strong Fermi resonance between 5^1 and 13^117^1 ; the two components are split by over 125 cm^{-1} (1513 and 1639 cm^{-1}). For most other bands in this region, only minor differences in frequency and intensity exist between the VPT2 and VPT2+K treatments. For 4-pyridyl, the most notable differences are a slight downward frequency shift of the 19^1 fundamental relative to VPT2, and a rebalancing of intensities between 3^1 and 8^19^1 .

Selected vibrational frequency measurements for the pyridyl radicals are available from Ar matrix isolation spectroscopy [188] and photoelectron spectroscopy [189]. Of the four values available for 2-pyridyl from matrix isolation, all are in excellent agreement in both frequency and relative intensity; the largest difference is 15 cm^{-1} . The agreement is also good for the gas-phase photoelectron frequencies; most calculated values for 2-pyridyl differ by an amount comparable to the experimental uncertainty, with the largest difference being 20 cm^{-1} (3.3σ) for 15^1 . Similar agreement is obtained for 3-pyridyl with the exception of modes 9^1 , 10^1 , and 11^1 from matrix isolation spectroscopy, all of which have relative intensities of 4% or less relative to the strongest band. For 4-pyridyl, the VPT2+K frequencies agree within experimental uncertainty with the exception of 3^1 , which differs by 25 cm^{-1} . However,

the matrix isolation spectroscopy assignments provided in the Supporting Information of Ref. 188 for 4-pyridyl disagree by significant margins, and also include one assignment to ν_{11} of A_2 symmetry. In addition, the reported frequency for ν_8 (1052.7 cm^{-1}) differs by over 80 cm^{-1} from the cryo-SEVI value (969 cm^{-1}), a difference too large to be ascribed to a matrix shift. It seems likely there was a transcription error in Ref. 188, so these will not be considered further.

In addition to the fundamental frequencies, the photoelectron spectroscopy results [189] yielded tentative assignments for several combination bands and overtones. Detailed comparisons are provided in the Supporting Information, along with potential alternative assignments to other totally symmetric states. In some cases, the proposed alternative assignments here correspond to transitions to 2-quantum states rather than the 3-quantum states originally proposed. For example, a band at 1940 cm^{-1} was originally assigned as 16^3 for 3-pyridyl; here we propose an alternative assignment of 15^2 (VPT2+K: 1938 cm^{-1}). These proposed assignments are based only on frequency agreement and upper state symmetry; additional insight could be obtained by Franck-Condon calculations which may help determine the most probable assignment.

3.7 Conclusion

A computational investigation into the rotational and vibrational spectra of the pyridyl radical isomers was carried out at the ae-CCSD(T)/cc-pwCVTZ and fc-CCSD(T)/ANO0 levels of theory. For use in pure rotational spectroscopy, we have computed equilibrium and ground state rotational constants, centrifugal distortion terms, spin-rotation tensors and hyperfine coupling parameters. The calculated hyperfine coupling constants involving ^1H , ^{13}C , and ^{14}N agree well with values derived from ESR spectroscopy. With these spectroscopic constants, detailed simulations of hyperfine splitting show that the hyperfine structure for the strongest series of rotational transitions collapses to a simple spin-rotation doublet above $N \approx 20$, which generally corresponds to frequencies above 200 GHz. For this reason, spectroscopy in the millimeter band is promising for the first spectroscopic identification of these

radicals. The vibrational spectrum in the 300-3500 cm^{-1} spectrum was calculated using the VPT2+K method, which involves an extensive variational treatment of resonances that cause the perturbative corrections in VPT2 to break down. In particular, the vibrational spectrum of 2-pyridyl is expected to feature considerably more intense vibrational bands compared with a harmonic treatment, though experimental measurements in the spectral regions featuring these resonances have not been made. For the low-frequency modes which have been measured experimentally, the calculated frequencies generally agree to within 20 cm^{-1} , with the majority falling within experimental uncertainty. Owing to the importance of pyridyl as an important reactive intermediate in combustion, atmospheric chemistry, and astrochemistry, it is hoped that the calculations presented here will assist in guiding the interpretation of new spectroscopic investigations in the laboratory.

3.8 Supporting Information

Additional supporting data for this work is loaded in Appendix A.

Chapter 4

Chirped-pulse Fourier Transform Microwave Spectroscopy (CP-FTMW)

Chirped-pulse Fourier transform microwave (CP-FTMW) spectroscopy is a technique for measuring the rotational spectra of gas-phase, polar molecules. Since CP-FTMW spectroscopy operates over a wide spectral region (~ 10 GHz), it is considered a broadband technique. This increased bandwidth enables several rotational transitions to be measured simultaneously, in contrast with previous techniques which are limited to ≈ 1 MHz bandwidth. A broadband microwave spectrum via CP-FTMW spectroscopy can be obtained several orders of magnitude faster than previous techniques because it exploits frequency-agile pulse generation and modern high-speed digitizers.[117] This chapter discusses the theoretical background for CP-FTMW spectroscopy, including chirp generation, polarization/emission, and sources of spectral line broadening.

4.1 Chirp Generation

Figure 4.1 shows a general block diagram of a CP-FTMW spectrometer. The microwave source (e.g., AWG) generates a linearly increasing frequency chirp in the form of an expo-

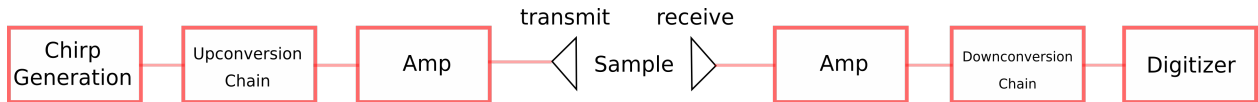


Figure 4.1: General CP-FTMW spectrometer schematic.

ponential function,

$$E(t) = E_0 e^{i(\omega_0 t + \frac{1}{2} \alpha t^2)}, \quad (4.1)$$

where E_0 is the electric field of the pulse, α is the linear sweep rate, and the instantaneous frequency (ω_{inst}) is equal to ω_0 at $t = 0$, by the following relationship,

$$\omega_{inst} = \omega_0 + \alpha t, \quad (4.2)$$

while α is the bandwidth ($\Delta\omega$) per pulse duration (t_{pulse}):

$$\alpha = \frac{\Delta\omega}{t_{pulse}}. \quad (4.3)$$

Once the chirp is generated, it may be upconverted as needed and amplified for broadcast via gain horns into a vacuum chamber containing the molecular sample, with all oscillators or frequency sources phase locked to a reference source (typically 10 MHz). On the receiver side, the chirp is amplified and (if needed) downconverted by a broadband mixer to lower frequency ranges and subsequently sampled by a digitizer. All electrical components on the upconversion/downconversion chain can be modified to produce the desired frequency range. Specific details of a custom built segmented CP-FTMW spectrometer (6 – 18 GHz) and a Ka-band CP-FTMW spectrometer (26.5 – 40 GHz) are in Chapters 5 and 6.

4.2 Polarization of Molecular Sample and FID Collection

A fast, frequency-swept pulse of electromagnetic radiation passing through the molecular sample causes the dipole moments of the molecules to coherently rotate. The resultant macroscopic polarization of the ensemble is described by the following in-phase (P_r) and

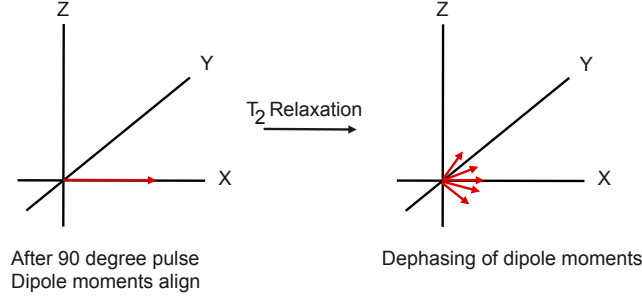


Figure 4.2: T_2 relaxation process.

out-of-phase (P_i) polarization components,

$$P_r = \frac{\Delta N \mu_{ab}}{2} r_1', \quad (4.4)$$

$$P_i = \frac{\Delta N \mu_{ab}}{2} r_2', \quad (4.5)$$

where N is the total number of molecules per unit volume, μ is the dipole moment, and r_1'/r_2' are the real and imaginary components of the macroscopic polarization.[200] The ensemble polarization is related to the emitted electromagnetic radiation, which will be discussed in Section 4.3. The mechanism of polarization and relaxation in FT microwave spectroscopy is analogous to spin-polarization in FT-NMR spectroscopy. The polarization relaxes according to three first-order linear differential equations,

$$\frac{dP_r}{dt} + \Delta\omega P_i + P_r = 0 \quad (4.6)$$

$$\frac{dP_i}{dt} - \Delta\omega P_r + \frac{\mu\omega_1\Delta N}{2} + \frac{P_i}{T_2} = 0 \quad (4.7)$$

$$\frac{d}{dt} \left(\frac{\mu\Delta N}{2} \right) + \omega_1 P_i + \frac{(\mu/2)(\Delta N - \Delta N_0)}{T_1} = 0 \quad (4.8)$$

where T_1 and T_2 are phenomenological relaxation times, $\Delta\omega$ is the difference between the resonant frequency of the system and the applied frequency, ΔN is the population difference, and ΔN_0 is the equilibrium average of ΔN . T_1 is the timescale for ΔN to relax to the equilibrium value ΔN_0 , and T_2 the decoherence time (Figure 4.2).[201] Technological advances in chirp generation sources makes it possible to perform chirped-pulse excitation

in a time scale shorter than the transient emission time (T_2), thereby allowing detection of the molecular emission to occur following chirped excitation.[104]

The relative time of the frequency sweep and the molecular relaxation time (T_2) comes in two types: rapid adiabatic passage (RAP) regime and linear fast passage (LFP) regime. RAP regimes are those in which there is strong coupling between the molecules to the microwave field (i.e., Rabi frequency), whereas LFP regimes are those in which there is weak coupling. More commonly, the chirped pulse response in CP-FTMW spectroscopy falls in the range of the LFP regime, which can be described via the following chirped pulse excitation signal strength expression,

$$S \propto \omega \mu^2 E_{pulse} \Delta N_0 \sqrt{\frac{\pi}{\alpha}}, \quad (4.9)$$

where ω is the angular frequency of excitation, μ is the transition dipole moment, E_{pulse} is the electric field strength of the pulse, and once again, ΔN_0 is the population difference at equilibrium (assumed to be unchanged in the weak pulse limit of the LFP). A number of tests were performed on the Ka-band CP-FTMW spectrometer for two different rotational transitions of pyridine, in order to determine the optimal sweep rate that achieved maximum intensity. These results are in Chapter 6.

4.3 FID Detection

Relaxation from the polarized state by the high-powered chirped-pulse results in a free induction decay (FID). A receiver horn collects the FIDs and the incoming signal passes through an optional downconversion chain before digitizing via an oscilloscope. The emission signal from the FID is amplified by a low-noise amplifier to boost the FID signal for data processing. A diode limiter and a fast PIN switch ensure the low-noise amplifier is protected from the high-powered chirp. A DC block prevents any build-up of DC potential that could damage the amplifiers. Timings are controlled by an external pulse generator referenced to the common 10 MHz clock to allow for coherent time domain averaging of the FID. A Fourier transform of the digitized rotational FID signal results in a rotational spectrum. Experimental data from a Ka-band CP-FTMW spectrometer are in Chapter 6.

4.4 Molecular Sample

Microwave spectroscopy is often performed at very low temperatures (< 30 K) because the rotational partition function scales with $T^{\frac{3}{2}}$ for nonlinear polyatomic molecules and T for diatomic molecules. To produce such low temperatures, a common method is to use a free jet expansion of gas into a vacuum chamber. The constraint lies in the considerable amount of carrier gas needed to effectively cool the gas during an expansion, which necessitates more powerful vacuum pumps in order to achieve high repetition rates.[202] The rotational spectra of metal complexes, biomolecules, Van der Waals complexes, and transient species like ions and radicals have all been measured in pulsed free jet.[105, 115, 118, 203] The properties of a pulsed free jet gas expansion depend on the difference between the backing pressure (P_b) of the gas and the vacuum chamber pressure (P_0). Empirical analysis of an ideal gas has shown that the location of the Mach-disk (x) relative to the nozzle diameter (d) is estimated to be[204]

$$\frac{x}{d} \propto \sqrt{\frac{P_0}{P_b}}, \quad (4.10)$$

where the temperature ratio between the stagnation pressure and backing pressure (T_0/T_b) of the system is approximately one. Supersonic flow is achieved when the pressure ratio P_0/P_b at the nozzle exit exceeds the critical pressure from the following expression,

$$P_{\text{critical}} = \frac{P_0}{P_b} = \left(\frac{\gamma + 1}{2} \right)^{\frac{\gamma}{\gamma-1}}, \quad (4.11)$$

where γ is the specific heat ratio of a gas.

With each pulse of gas into a low pressure vacuum chamber, internal energy is converted to translational energy, and the number density and internal temperature decrease over the length of the expansion. Rotational transitions are then measured with low collision rates at these low temperatures (≈ 10 K), thus reducing pressure broadening effects. The number density n of molecules along the axis of the expansion is

$$n = n_0 \left(\frac{x}{a(\alpha)\frac{d}{2}} \right)^{-2}, \quad (4.12)$$

where n_0 is the number density at the nozzle exit and $a(\alpha)$ is a constant that depends on γ . [205, 206] The temperature decrease of a free jet expansion is also related to x , $a(\alpha)$, d and γ by

$$T(x) = T_0 \left(\frac{x}{a(\alpha) \frac{d}{2}} \right)^{-2(\gamma-1)}. \quad (4.13)$$

The direction of the microwave radiation relative to the expansion axis can also add additional Doppler broadening contributions (Section 4.5.3) to the linewidth. To minimize Doppler effects, co-axial interactions of the free jet expansion and radiation tend to be employed. [101, 207] The spectral lineshape dependence on molecular trajectories that are not perpendicular to the microwave radiation are related to the flow velocity V and the angle θ from the center flow line by $\approx V \sin(\theta)$. [208] A more thorough discussion of Doppler broadening effects is in Section 4.5.3.

4.5 Sources of Spectral Line Broadening

The spectra of a molecule contains peaks that have a characteristic shape and width as a result of homogeneous or inhomogeneous line broadening. The homogeneous broadening of a spectral peak gives rise to a Lorentzian lineshape function, and can arise most often by pressure broadening caused by collisions, in addition to smaller factors like the natural linewidth. Inhomogeneous line broadening takes on the Gaussian form and is most often a consequence of Doppler effects. Figure 4.3 (provided by K. N. Crabtree) shows both the Lorentzian and Gaussian lineshape functions with different widths. The following sections discuss the different types of broadening effects and their relevance for CP-FTMW spectroscopy.

4.5.1 Natural Linewidth

The natural linewidth of a rotational transition is typically very small, compared with other forms of broadening. Spontaneous emission from state m to n has a particular lifetime (Δt) and energy (ΔE), as shown by the uncertainty principle,

$$\Delta E \Delta t \geq \frac{\hbar}{2}. \quad (4.14)$$

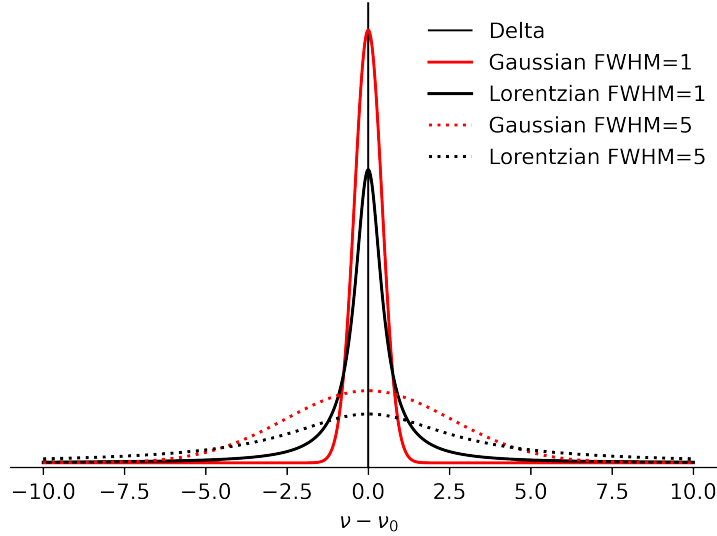


Figure 4.3: Normalized Gaussian (red) and Lorentzian (black) lineshape functions for two different full width at half maximum (FWHM) values.

The natural linewidth ($\Delta\nu$) for this type of transition depends on the dipole moment matrix element ($\hat{\mu}$), and in frequency units of Hz, is given by,

$$\Delta\nu \approx 1.86 \times 10^{-38} v_{mn}^3 |\langle \phi_m | \hat{\mu} | \phi_n \rangle|^2, \quad (4.15)$$

where v_{mn} is the rotational transition frequency.

In one example, a microwave pulse may polarize an ensemble of oscillating dipole moments, and as the amount of population in the upper state decreases, the amplitude of the oscillation will also decrease. In order to determine the Lorentzian lineshape function that describes that phenomenon, a Fourier transform of a damped oscillation is performed in order to determine the frequency distribution related to this natural linewidth. Normalizing the Lorentzian lineshape function, squaring it, and converting from angular frequency, ω , to frequency, ν , gives

$$L(\nu) = \frac{\gamma}{(\frac{\gamma}{2})^2 + (2\pi)^2(\nu - \nu_0)^2}, \quad (4.16)$$

with a full width at half maximum (FWHM) given by $\gamma/2\pi$, which provides a useful measure of the width of the peak. Figure 4.3 shows the shape of a typical Lorentzian lineshape function.

4.5.2 Pressure Broadening

Pressure broadening of spectral peaks is a result of intermolecular collisions between molecules as well as collisions between molecules and their boundaries, effectively reducing the S/N ratio by reducing the duration of the detectable signal.[209] The linewidth ($\Delta\nu_{1/2}$) is inversely proportional to the mean time between collisions, T_2 , and proportional to the pressure (P) and the experimentally determined pressure-broadening coefficient (α):

$$\Delta\nu_{1/2} = \frac{1}{\pi T_2} = \alpha P. \quad (4.17)$$

Generally, α values are on the order of 10 MHz/Torr.[100]

At a particular temperature, α represents the collisional cross section of two colliding species. There is a general trend of increasing α with increasing molecular size as well as a linear dependence on pressure broadening coefficients with temperatures of $T > 30$ K.[210] However, at low temperatures ($T < 10$ K), there is a deviation from this pattern and the pressure broadening coefficients tend to increase as temperature decreases.[211]

4.5.3 Doppler Broadening

Doppler broadening is a form of inhomogeneous line broadening of a spectral peak and takes on the form of a Gaussian line shape function (refer to Figure 4.3 for the shape of a typical Gaussian lineshape function illustrated by two different FWHM values). For a given particle moving with a certain velocity, ν , traveling parallel or perpendicular to the direction of propagation, \vec{k} , there is frequency shift from the perspective of the detector, simply described as

$$\nu = \nu_0 \left(1 + \frac{v}{c} \right), \quad (4.18)$$

where ν_0 is the resonant frequency without Doppler shifts, v is the velocity of the molecule, and c is the speed of light (299,792,458 m/s).

The Maxwell-Boltzmann distribution function, $(m/2\pi k_b T)^{\frac{1}{2}} e^{-\frac{mv^2}{2k_b T}}$, describes the distribution of velocity that generates the Doppler lineshape function for a system in local thermodynamic equilibrium (LTE), where m is the mass of the particle, k_b is Boltzmann's constant,

T is temperature, and v is the velocity. The normalized Doppler lineshape function, in terms of velocity gives the following expression,

$$S_D(v, v_0) = S_0 e^{\left[\frac{-mc^2}{2k_b T} \left(\frac{v - v_0}{v_0} \right)^2 \right]}, \quad (4.19)$$

where S_0 is a constant defined as $(1/v_0)(mc^2/2\pi k_b T)^{1/2}$. The lineshape function in terms of the line breadth, Δv_D , is

$$S_D(v, v_0) = S_0 2^{-\left[\frac{v - v_0}{\Delta v_D} \right]^2}, \quad (4.20)$$

with the FWHM for Doppler broadened peaks twice that of the line breadth,

$$2\Delta v_D = \frac{2v_0}{c} \sqrt{2N_a k_b T \ln(2)}, \quad (4.21)$$

where N_a is Avogadro's number. In experiments where a pulsed jet expansion is perpendicular to the microwave radiation, Doppler broadening effects incur linewidths on the order of ~ 100 kHz (for a 10 GHz transition) because of the velocity spread that makes up the geometry of the gas expansion.[117]

4.6 Conclusion

The theoretical basis for a CP-FTMW spectrometer has been discussed and the general design has been presented. This technique allows for broadband chirped pulse excitation and broadband detection of rotational FIDs, ensuring for highly resolved molecular spectra. High-speed digital electronics enable real-time FID detection and fast data acquisition, enabling the development of this broadband technique for use in FTMW spectroscopy. A CP-FTMW spectrometer equipped with a pulsed valve that generates a free jet gas expansion can reach cold rotational temperatures applicable for studying astrochemically relevant molecules. Several sources of homogeneous and inhomogeneous spectral line broadening are also discussed. Pressure and Doppler broadening can often be attributed to many of the broadenings observed in rotational spectra. Application of this technique can be found in

Chapters 5 and 6, which provides a design implementation for two custom-built CP-FTMW spectrometers as well as the results of optimizations.

Chapter 5

Segmented CP-FTMW Spectroscopy with Direct Digital Synthesis (DDS) Technology

5.1 Introduction

As discussed in Chapter 4, chirped-pulse Fourier transform microwave (CP-FTMW) spectroscopy is a valuable spectroscopic technique for the discovery of new astrochemically relevant molecules. By making use of this fast and high-resolution broadband technique, rotational spectra of short-lived species can be collected quickly and easily. However, the high bandwidth also increases the cost of a CP-FTMW spectrometer. To address this, a “segmented” CP-FTMW spectrometer divides the entire measured broadband bandwidth into smaller segments (in this case 1 GHz).[212] As a result of segmented acquisition, broadband frequency ranges can be measured with a reduced digitizer sampling rate, thereby reducing the overall cost of the instrument.

To further reduce the cost, the instrument described in this chapter also replaces the arbitrary waveform generator (AWG)[212, 213] conventionally used in a CP-FTMW spectrometer with a low-cost direct digital synthesizer (DDS).[214, 215] The DDS-based programmable waveform generator is a low cost alternative to the AWG with a remarkably low power consumption (< 100 mW). In 2015, the components of a DDS-based CP-FTMW

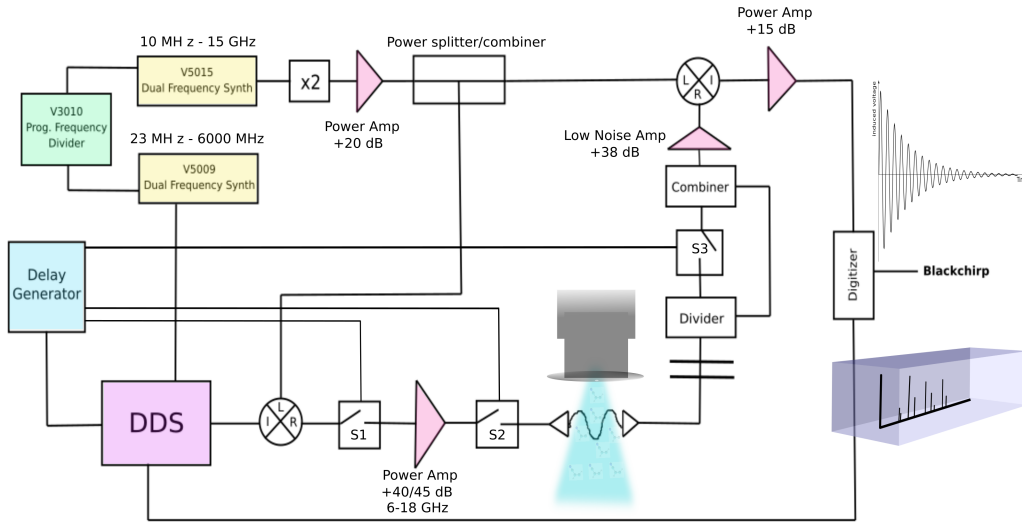


Figure 5.1: Schematic of the segmented CP-FTMW spectrometer using the DDS technology.

spectrometer cost up to \$5000[216, 217], while each major component of a CP-FTMW spectrometer using AWG technology with powerful amplifiers/digitizers costs between \$100,000 and \$200,000.[218, 219] This chapter discusses the technical specifications of a custom-built DDS-based segmented CP-FTMW spectrometer and the initial results for microwave chirp generation.

5.2 Technical Specifications

A schematic of the segmented CP-FTMW spectrometer is shown in Figure 5.1. For the purposes of chirp generation, a DDS (Analog Devices, 9914) outputs a linearly increasing frequency chirp from DC – 1 GHz. The output of a Valon 5015 dual frequency synthesizer (tunable across the 6–15 GHz band) is frequency doubled (Marki, MLD-0632) and then amplified (Mini-Circuits, ZX60-183A-S+), before it is mixed (Miteq, DB0418LW1) with the output from the DDS. The output of the mixer contains two sidebands above and below the carrier frequency. Two SPST protection switches (S1/S2, Narda, S213D) flank a solid state amplifier (40 dBm, RF-Lambda, RFLUPA0618GA) and remain open until the amplified chirp is triggered. When the DDS transmits the signal, S1/S2 close for the transmission of the

chirp, and then open immediately for the remainder of the chirp excitation process, timings of which are controlled by a delay generator (Quantum Composer, 9528). The resultant chirp is broadcast by a standard gain horn through a Teflon lens into a chamber ($\approx 10^{-6}$ Torr) where it probes a supersonic expansion of gas, which is produced by a piezoelectric pulsed valve at a rate of 1 Hz. The microwave horns are designed to transmit and receive radiation for the following frequencies: 7.05 – 10 GHz (Pasternack, PE9858-10) and 12.4 – 18 GHz (Pasternack, PE9854-10). All frequency generation sources are phase-locked to a 10 MHz reference from the Valon 3010.

On the receiving side, a third SPST protection switch (S3) remains closed at all times except when the chirp is received, thereby preventing damage to the downconversion chain. A power divider/combiner (Mini-circuits, ZX10-2-183-S+) splits off power from the chirp to allow for real-time monitoring of the chirp after the switch. The emission signal is amplified by a low noise amplifier (Mini-Circuits, ZX60-P105LN+), downconverted by a broadband mixer (Narda, DB0418LW1), and digitized (Spectrum Instrumentation, M4i.2220-x8) for data processing at a sample rate of 2.5 GS/s and analog bandwidth of 1.25 GHz. A Valon dual synthesizer produces the reference clock frequency of 3.75 GHz for the AD9914, instead of the 3.5 GHz specified in the device manual, in order to better match the sampling rate of the digitizer. The segmented acquisition is $\approx 1 \mu\text{s}$ long for a single pulse and the LO signal is added/subtracted from each segment to obtain the full bandwidth. For a full broadband scan, different LO segments of 1 GHz bandwidth are stitched together to cover the full 6 – 18 GHz frequency range.

Example pulse timings used for collecting FIDs are shown in Figure 5.2. The chirped pulse delay of $200 \mu\text{s}$ is shown on the AWG control line (I). The eventual chirp (II) is $1 \mu\text{s}$ long. Timings for opening and closing the S1/S2 and S3 switches are indicated by the AMP (III) signal and Prot (IV) signal, respectively. The AMP signal is active low and both Prot and AWG signals are active high. For active low signal settings, the S1/S2 switches are open when the voltage is high on the AMP control line and closed when the voltage is low (reverse this logic for active high signals).

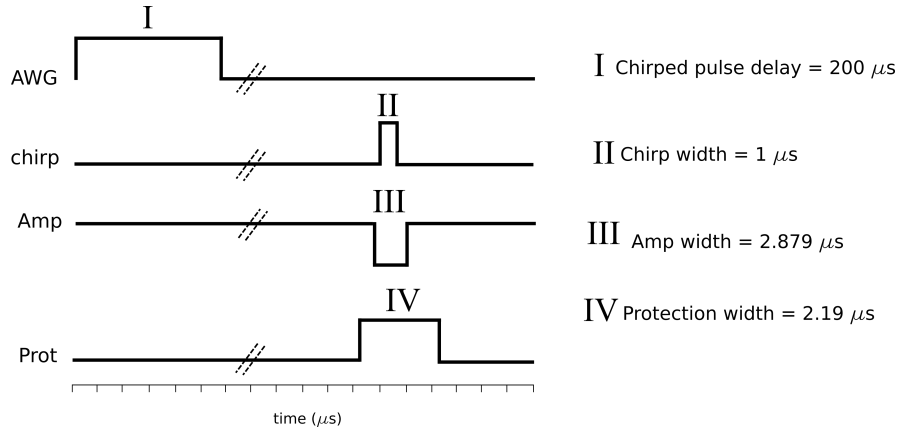


Figure 5.2: Example pulse timings (not to scale) used for collecting free induction decays during the instrument optimization phase.

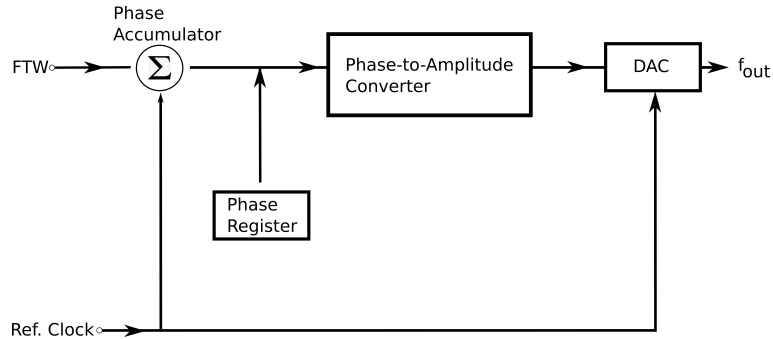


Figure 5.3: Block diagram of DDS.

A DDS generates an analog sinusoidal waveform using a digital-to-analog converter.[220] The output frequency is controlled by a frequency tuning word (FTW) and reference-clock frequency (f_{clock}), the latter of which is from an internal phase-locked loop multiplier,[221]

$$f_{\text{out}} = \frac{FTW}{2^{32}} * f_{\text{clock}}. \quad (5.1)$$

Figure 5.3 shows a general overview of the DDS components, inspired by Ref. [222].

The AD9914 contains a set of 32-bit LSB-first registers spanning an address range of 0 to 27 (0x00 to 0x1B in hexadecimal format). Of the potential 28 serial registers, there are a select few that control the digital ramp generator (DRG). The register values are set with an Arduino microprocessor (Arduino Mega). The AD9914 features a ramp generation mode in which the DDS signal control parameters are delivered by a digital ramp generator. Several of the DDS registers control the ramp parameters, such as the digital ramp lower/upper

Table 5.1: Register map and bit descriptions for generating a 1 GHz chirp.

Register Name	Contents	Value
Digital Ramp Lower Limit	0x00000000	0 GHz
Digital Ramp Upper Limit	0x44444433	1.15 GHz
Rising Digital Ramp Step Size	0x0156AC01	22.46 MHz
Falling Digital Ramp Step Size	0x0156AC01	22.46 MHz
Digital Ramp Negative Slope	0x0003	3 ns
Digital Ramp Positive Slope	0x0003	3 ns

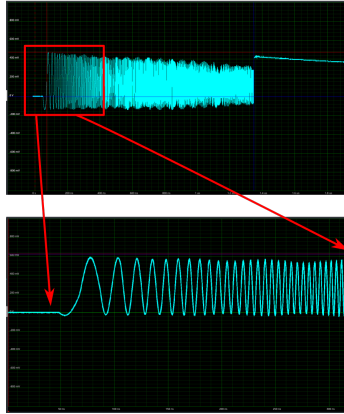


Figure 5.4: Linearly increasing 1 GHz frequency chirp from the segmented CP-FTMW spectrometer (top) and zoomed in portion showing the linearly increasing frequency characteristic (bottom).

limits, the digital ramp rising/falling step size, and the digital ramp positive/negative slope characteristics, shown in Table 5.1. For the CP-FTMW spectrometer, the settings are chosen to generate a 1 GHz linear frequency sweep in $1 \mu\text{s}$ (Figure 5.4).

Phase stability was a concern when testing the chirp. Figure 5.5 shows phase drift present in the initial portion of the linearly increasing chirp. This is caused by the DDS output beginning where previous chirps end, so all subsequent chirps appear to be out-of-phase. To solve this problem, the “Autoclear phase accumulator” command is sent through the Arduino to effectively reset the DDS phase to 0 MHz. This ensured that the chirp was always in phase.

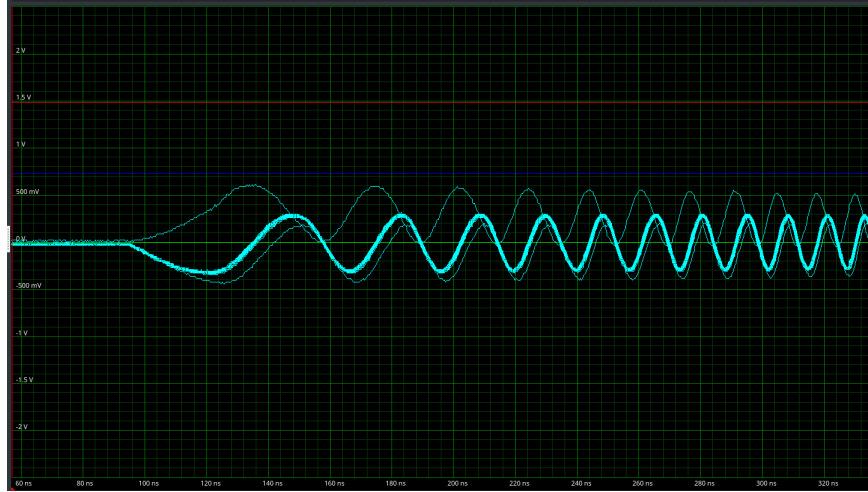


Figure 5.5: Phase instability of chirp.

5.3 Results

The segmented CP-FTMW spectrometer was tested for its ability to generate a linearly increasing frequency chirp. As stated previously, results of the linearly increasing 1 GHz chirp are shown in Figure 5.4. However, once the DDS was connected to the entire microwave circuit detailed in 5.1, power inconsistencies were present across the 6 – 18 GHz frequency range. The chirp power distribution is shown in Figure 5.6 from 9 – 10 GHz, with normalized intensities. The left plot shows the chirp (150 FIDs averaged) passing through the upconversion/downconversion chain while bypassing the vacuum chamber and microwave horns, whereas the right plot includes both of those components. When power is passed through the vacuum chamber and horns, it is evident that there is a significant power loss. A few likely causes for this power dropout include the Teflon lenses placed on the entrance and exits to the vacuum chamber where radiation to passes through as well as the coupling efficiency/diffraction effects from the possible misalignment of the microwave horns. It is also possible that a high-pass filter is attenuating the signal with frequencies lower than the cutoff frequency, ultimately decreasing the amplitude of low frequencies. With these factors in mind, boosting the power across the desired frequency range may require modifications to the design. Further testing of the segmented instrument was suspended in favor of work-

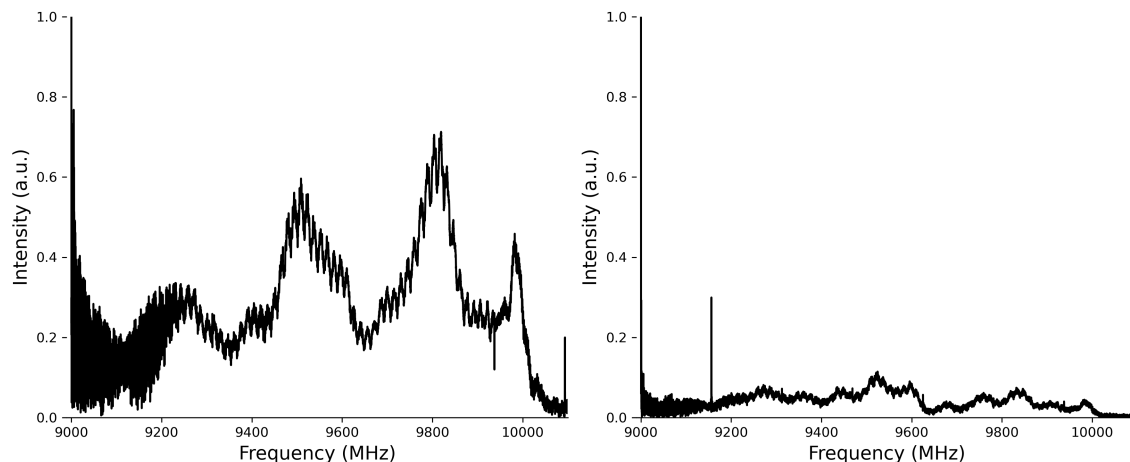


Figure 5.6: Chirp power distribution from 9–10 GHz for the segmented CP-FTMW spectrometer after upconversion/downconversion chain. (left) Bypassing vacuum chamber/microwave horns, (right) including vacuum chamber/microwave horns. Chirp duration: $1 \mu\text{s}$, LO frequency: 9 GHz

ing with the newly constructed Ka-band CP-FTMW spectrometer, results of which are in Chapter 6.

5.4 Conclusion

This study presents a segmented CP-FTMW spectrometer which has been constructed and tested, as well as its performance evaluated. During the optimization phase, the results show that the segmented CP-FTMW spectrometer successfully outputs a linearly increasing 1 GHz chirp. This instrument uses the DDS technology to generate the chirp, which passes through an upconversion chain to eventually output the frequency range of 6 – 18 GHz. User controlled digital ramp generation precisely controls the frequency, phase, and amplitude of the chirp. A register map was used to control these signal parameters. The results from these optimizations show promise for this instrument. Future work should include further tests on the power distribution of the chirp as well as timings relative to the gas pulse from the piezoelectric pulsed valve source (described in Chapter 6) for the intent to measure the rotational spectra of gas-phase molecules in a supersonic expansion.

Chapter 6

Optimization of a Custom Built Ka-band Chirped-Pulse Fourier Transform Microwave (CP-FTMW) Spectrometer

6.1 Introduction

This chapter discusses the optimization of a custom built Ka-band CP-FTMW spectrometer and the data obtained from the instrument's initial experiments. This newly built instrument is capable of measuring the rotational spectra of polar, gas-phase molecules in the frequency range of 26.5 – 40 GHz. To establish a baseline for this instrument's capabilities, and optimize the signal, two molecules were chosen to study: pyridine and acrylonitrile. The parameter space explored during the optimizations include gas source pulse duration, discharge source, and chirp excitation timings relative to the gas expansion. The data obtained from these experiments will be discussed further, as well as the resulting rotational spectra of pyridine and acrylonitrile.

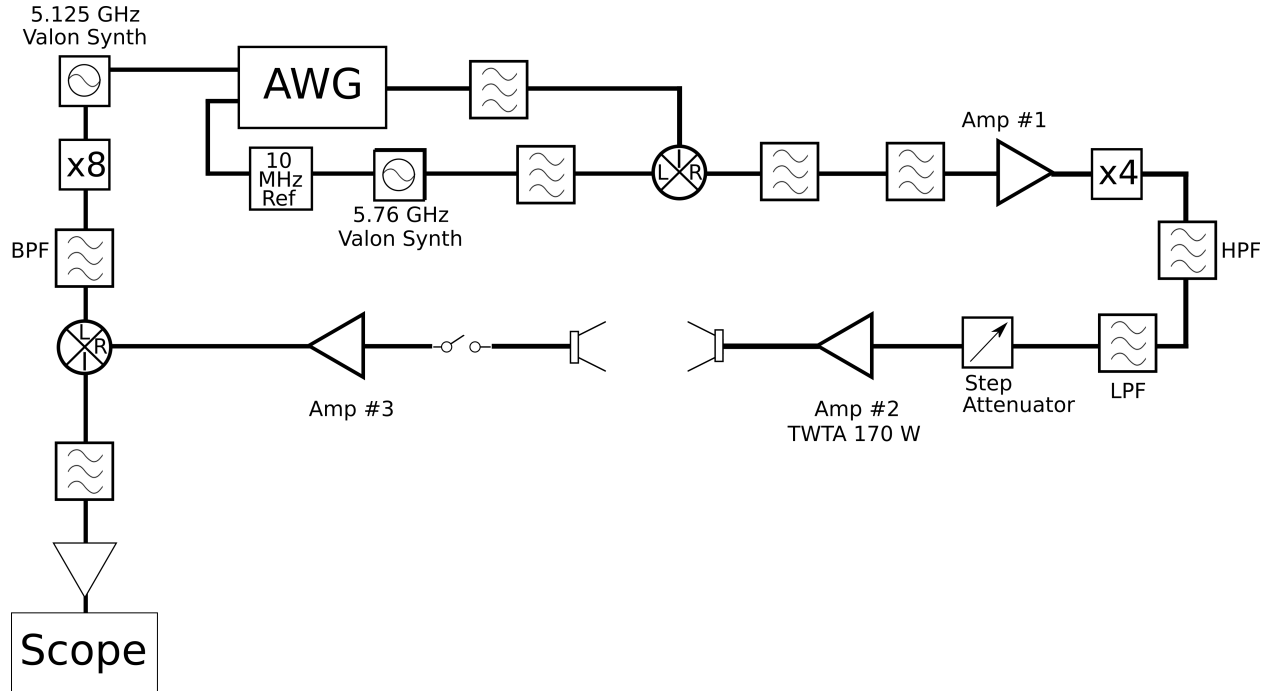


Figure 6.1: Block diagram of the Ka-band CP-FTMW spectrometer.

6.2 Ka-band CP-FTMW Spectrometer

The Ka-band spectrometer consists of three primary components: 1) chirp generation, 2) sample interaction region, and 3) detection region. Figure 6.1 shows the general overview of the Ka-band spectrometer. To create the microwave chirp, a 3.375 GHz linear frequency sweep is generated from an arbitrary waveform generator (Tektronix AWG700002A, 16 GSa/s) from 1.52 – 4.895 GHz. This signal passes through a filter (K&L Microwave 6L250-6000/T18000-O/O) and is mixed (Marki MWave, T3H-18IS) with a single 11.52 GHz frequency source (Valon Technology 5009) and the unwanted frequencies in the upper side band are removed using band-pass filters (Marki MWave LPF, FLP-4300 & AMTI HPF, H26G40G1). The signal is then multiplied (x4, Wright Technologies, ASX40-420) and the resulting 13.5 GHz chirp spanning 26.5 – 40 GHz is amplified to approximately 170 W by a traveling wave tube amplifier (TWTA, Applied Systems Engineering 187Ka-H) and transmitted into the vacuum chamber through a horn-coupled microwave antenna (Advanced Technical Materials, PNR 28-449-6/24). In this case, microwave radiation is perpendicular

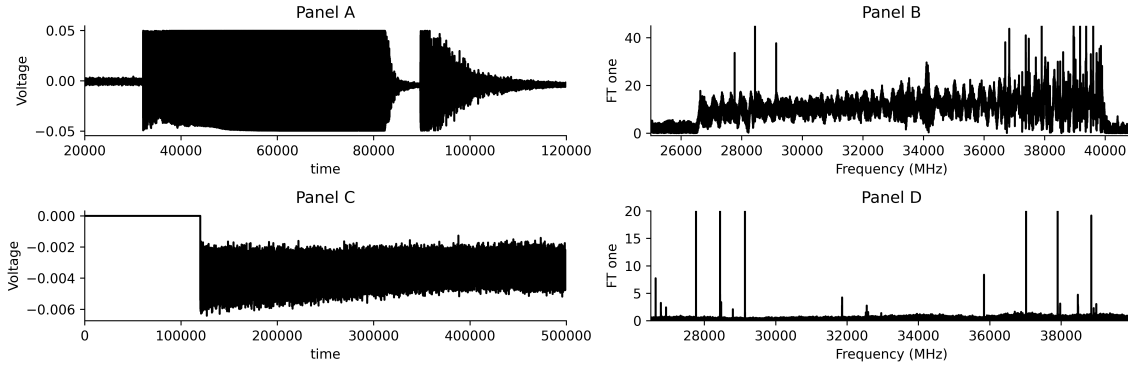


Figure 6.2: Panel A: Time domain signal of microwave chirp. Panel B: Fourier transform of microwave pulse showing broadband coverage of 13.5 GHz. Panel C: Chirp zeroed out of time domain signal. Panel D: Fourier transform signal of zeroed out time domain signal showing rotational transition frequencies.

to the expansion of the free jet gas. A second antenna located on the other side of the vacuum chamber (≈ 60 cm away) receives the microwave chirp/emission signal. Eccosorb foam microwave absorber lines the interior of the vacuum chamber to reduce the reflectivity of the microwave radiation from the interior metal surface.

On the downconversion side, a diode limiter (Clear Microwave, LT1840H) and SPST switch (Quinstar, QSC-ASR000) together protect the low noise amplifier (Minicircuits, ZX60-P105LN+) from the high powered chirp. The emission signal with a 40.96 GHz LO frequency from the outputted 5.12 GHz output of the Valon programmable frequency synthesizer (Valon 5009) is downconverted at a mixer (Marki MWave, ML1-1644IS), filtered by a low-pass filter (Marki MWave, FLP-1740), and amplified (Minicircuits, ZVA-183-S+) before the oscilloscope (Tektronix DPO72004 16 GHz DSO) digitizes the signal. The Fourier transform of the time-domain signal yields a rotational spectrum with a 13.5 GHz bandwidth.

Figure 6.2 shows the downconverted microwave chirp (Panel A), allowing for real-time monitoring of the chirp for phase coherence. The chirp is saturating the digitizer, so the entirety of the chirp is not present in the figure. Panel B displays the Fourier transform of the time-domain signal including the attenuated chirp, which shows the Ka-band frequency bandwidth of 13.5 GHz. Zeroing out the values of the microwave chirp removes the chirp,

leaving the FID (Panel C). The FT then yields the Ka-band rotational spectrum (Panel D).

6.3 Experimental Setup

6.3.1 Sample Preparation

Two types of sample delivery systems are available for the Ka-band spectrometer, both of which are fed through a piezoelectric pulsed valve and expanded into a vacuum chamber, which is described more thoroughly in Section 6.3.2. Option one consists of sending a carrier gas at a constant backing pressure (0.5 – 3 atm) through a gas bubbler containing a liquid sample at room temperature. Option two is to dilute a carrier gas (< 1%) pressurized to ≈ 3 atm at room temperature. Ar (99.999%, Sigma-Aldrich) was generally chosen as the carrier gas. Typically, the experiments with the bubbler system achieved a factor of two greater S/N ratio compared to the 1% diluted system.

6.3.1.1 Pyridine

Pyridine (C_5H_5N , 99.8%, Sigma-Aldrich) is a 6-membered aromatic nitrogen heterocycle that is a near-oblate asymmetric top ($A = 6039.25$ MHz, $B = 5804.91$ MHz, and $C = 2959.21$ MHz).[194] The dipole moment for pyridine is $\mu_a = 2.215(1)$ D, determined from Stark measurements of ^{15}N -pyridine.[98] The vapor pressure of pyridine is ≈ 2 kPa at $20^\circ C$. [223]

6.3.1.2 Acrylonitrile

Acrylonitrile (CH_2CHCN , 99.9%, Sigma-Aldrich) is a near-prolate asymmetric top ($\kappa \approx -0.97$) with rotational constants of $A = 49850.69655(43)$ MHz, $B = 4971.212565(37)$ MHz, and $C = 4513.828516(39)$ MHz.[224] Acrylonitrile has a strong a -type rotational spectrum ($\mu_a = 3.821(3)$ D) and a weaker b -type spectrum ($\mu_b = 0.687(8)$ D).[112] The vapor pressure of acrylonitrile is ≈ 11 kPa at $20^\circ C$. [225]

6.3.2 Piezoelectric Pulsed Valve

The supersonic gas expansion source used in this dissertation is a custom-built Proch-Trickl pulsed valve (Figure 6.3).[226] It is comprised of a piezoelectric disc translator (Physik Instrumente, P-286.23) with an open time on the order of $50 - 100 \mu s$ and a stroke of $100 \mu m$



Figure 6.3: Piezoelectric pulsed valve (left) and discharge stack (right).

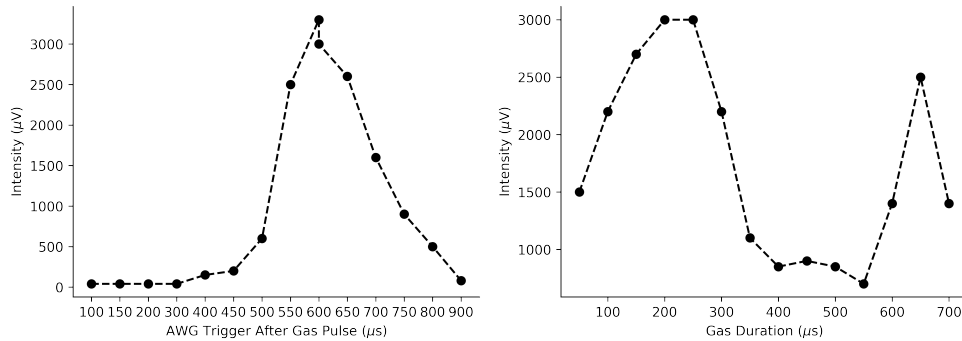


Figure 6.4: Timing of AWG trigger relative to the initial gas pulse (left) and different gas pulse widths with a constant $600 \mu\text{s}$ AWG delay (right).

at -1 kV . An o-ring attached to a movable plunger controls gas flow through a pinhole, and it is mounted in a hole at the center of the actuator by specially designed nuts. The plunger is positioned to appropriately compress the o-ring. The gas exits a $d = 1.25 \text{ mm}$ nozzle, generating a cold free jet gas expansion into a vacuum chamber, which is evacuated to a base pressure of 10^{-6} Torr by a diffusion pump (CVC, Type PMC-PMCS) that is backed by a mechanical pump (Welch 1397). The valve is driven by a high-voltage pulser at a repetition rate of 1 Hz for these experiments. The pulse strength is monitored by the current on an ionization gauge attached to the vacuum chamber.

In the experimental setup, the supersonic gas expansion travels a distance of approximately 150 mm to reach the microwave radiation. The optimal timing of the chirp relative to the gas pulse was determined by monitoring the intensity of the $4_{04} - 3_{03}$ (37903.5 MHz) rotational transition for acrylonitrile while varying the chirp delay (Figure 6.4) The highest

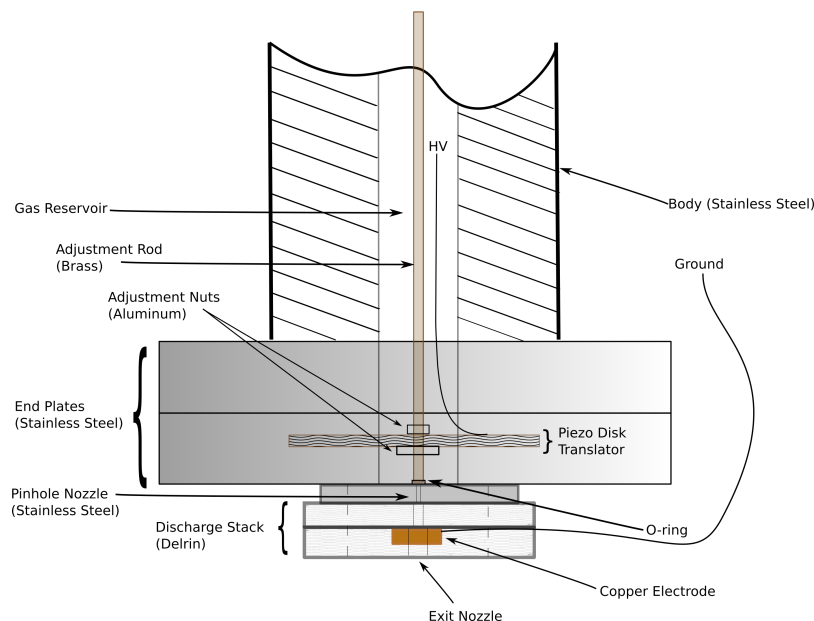


Figure 6.5: Cross-sectional illustration of the discharge stack attached to the piezoelectric pulsed valve.

signal intensity was observed at a delay of $600 \mu\text{s}$ after the gas pulse, and had a width of $100 \mu\text{s}$. Additionally, the gas duration was varied ($50 - 700 \mu\text{s}$) while keeping the AWG delay constant ($600 \mu\text{s}$) in order to determine the consistency of the gas pulse, as indicated by the right plot in Figure 6.4. Two peaks were observed at 200 and $650 \mu\text{s}$, which indicates two gas duration times that are optimal for the interaction of microwave radiation with the gas. Generally, shorter gas pulses showed more consistent behavior and used less sample, so all experiments used a gas pulse duration value of less than $200 \mu\text{s}$, depending on the experimental conditions (backing pressure, nozzle diameter, sample delivery system, etc.).

6.3.3 Plasma Discharge Chemistry

For the generation of transient gas-phase species, such as radicals, an end-mounted discharge stack is attached to the body of the piezoelectric pulsed valve device, as shown in the Figure 6.5. As soon as a gas pulse is generated, it is discharged at a copper electrode (DC to -700 V) for $1000 \mu\text{s}$, while the face plate acts as a ground. The discharged gas then passes through a confined channel from two inert Delrin discs that are placed after the exit nozzle insulating

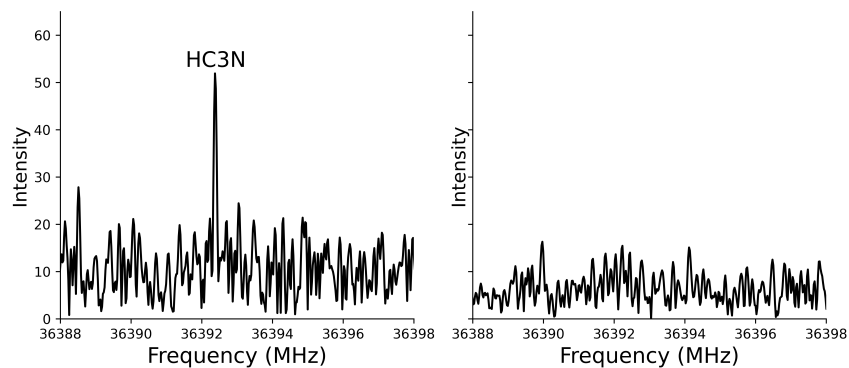


Figure 6.6: Comparison of acrylonitrile rotational spectrum with discharge on (left) and off (right). Single peak is fragmentation product cyanoacetylene HC_3N .

the copper electrode (Figure 6.3). A variety of species are produced in a plasma discharge, and a CP-FTMW spectrometer is used to detect all the polar species simultaneously by measuring their rotational spectrum. From an acrylonitrile discharge, the strongest discharge product was cyanoacetylene (HC_3N), as shown in the rotational spectrum of Figure 6.6. This was an obvious molecule to measure because it has a large dipole moment (~ 3.7 D[227]) and rotational transitions in the Ka-band. As a means of maximizing the S/N ratio of all rotational transitions, the signal from this fragment was repeatedly measured and optimized.

Identifying fragments in the discharge spectrum of pyridine proved more challenging because there was an overall large intensity drop for the discharge products compared to the parent molecule. Figure 6.7 shows the comparison between a pyridine spectrum and a pyridine discharge spectrum. There are a number of unknown/unidentified(U) lines visible in the discharge spectrum. It is likely that fragmentation and recombination chemistry is frequent in the plasma discharge, generating molecules that are not measurable in the Ka-band. Several timings were altered to change the conditions of the plasma discharge, including discharge pulse duration (50 - 1000 μs) and discharge voltage (250 - 900 V). The backing pressure (0.5 - 3 atm) was monitored and adjusted as needed to maximize signal. Delrin discs with different thicknesses, ranging from 5.65 - 8.65 mm, were interchanged to adjust the distance the gas traveled between plasma generation and expansion. The inner diameters of the Delrin discs were also tested with a range of values (1 - 9 mm) and it

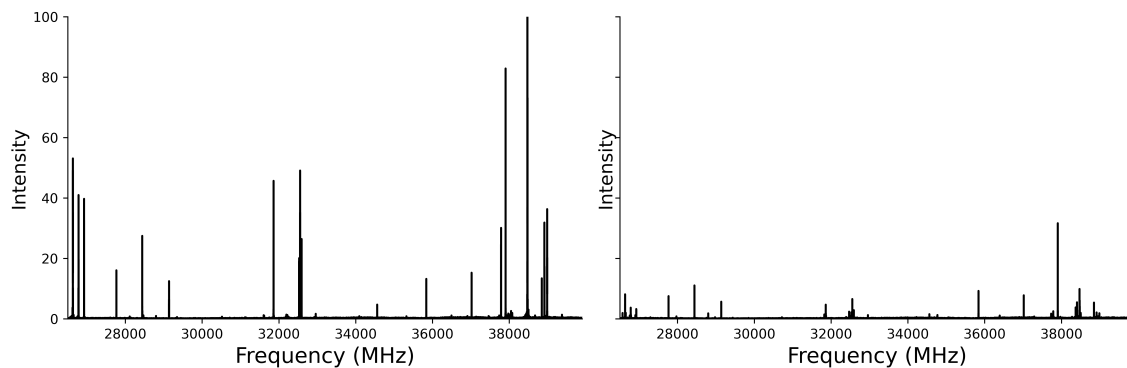


Figure 6.7: (left) CP-FTMW spectrum of pyridine. (right) CP-FTMW spectrum of pyridine discharge

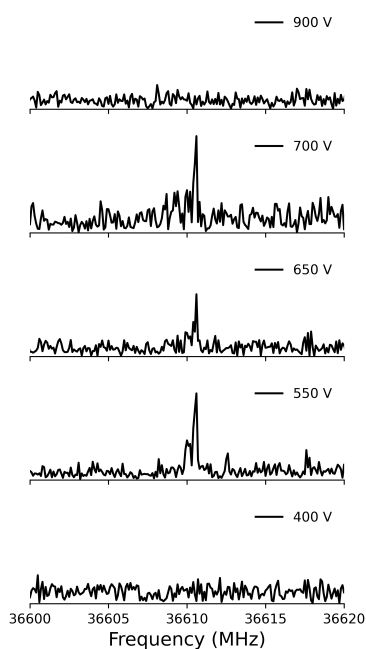


Figure 6.8: Pyridine discharge spectrum showing the discharge product U line at 36610 MHz with different applied voltages ranging from 400 V to 900 V.

was determined that a relatively large stack diameter (~ 7 mm) relative to the exit pin hole diameter (~ 1 mm) produced greater signals, compared to the alternatives.

In addition to adjusting the designs of the discharge stack, the voltages applied to the stack can also be adjusted during the optimization phase. Optimal discharge voltages for our application ranged from 500 to 700 V (Figure 6.8). For the U line at 36610 MHz,

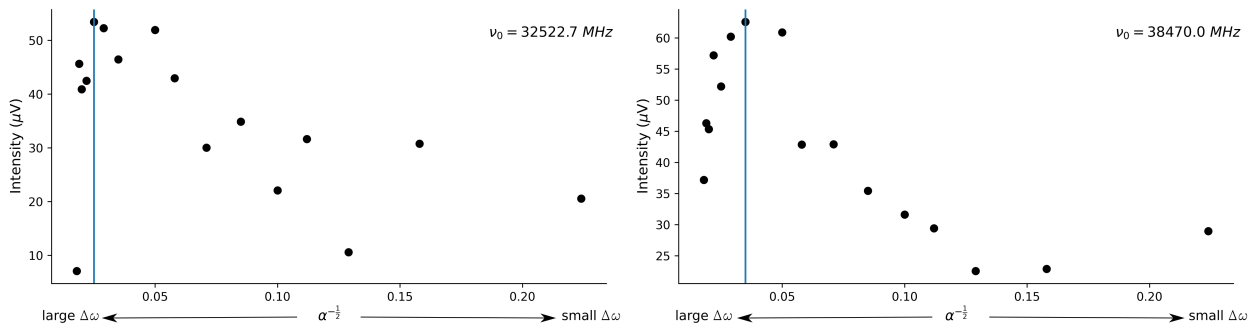


Figure 6.9: Variation in signal strength with pulse bandwidth ($\alpha^{-\frac{1}{2}}$) with a pulse duration of 1 μs is shown for 32522.7 MHz (left) and 38470.0 MHz (right) rotational transitions for pyridine.

below 500 V no discharge products were present leaving only the precursor available to be measured. Above 700 V, no lines were observed from either the precursor or any products.

6.4 Signal Intensity Levels

Chapter 4 discussed the macroscopic polarization when microwave radiation interrogates a molecular sample. The signal intensity of the resulting free induction decay (FID) is

$$\text{Signal} \propto \omega E \mu^2 \Delta N_0 \sqrt{\frac{\pi}{\alpha}}, \quad (6.1)$$

where E is the chirp electric field strength, μ is the projection of the electric dipole moment, ΔN_0 is the population difference between the upper and lower states, and α is the linear sweep rate, which is the ratio of the chirp frequency bandwidth ($\Delta\omega$) and the chirp pulse duration (Δt).

$$\alpha = \frac{\Delta\omega}{\Delta t}. \quad (6.2)$$

Plots of signal intensity (μV) versus $\alpha^{-\frac{1}{2}}$ for two rotational transitions of pyridine are shown in Figure 6.9. The chirps were centered on the rotational frequency and the bandwidth varied, holding the chirp duration constant. For both experiments, the chirp excitation reaches a peak before dropping off exponentially, indicating that decreasing the bandwidth past this point is negatively affecting the signal intensity. Equation 6.1 only pertains to the linear region at low values of $\alpha^{-\frac{1}{2}}$. Note the optimal chirp excitation bandwidth (which is illustrated as the blue line in Figure 6.9) was determined to be ≈ 800 MHz for the respective

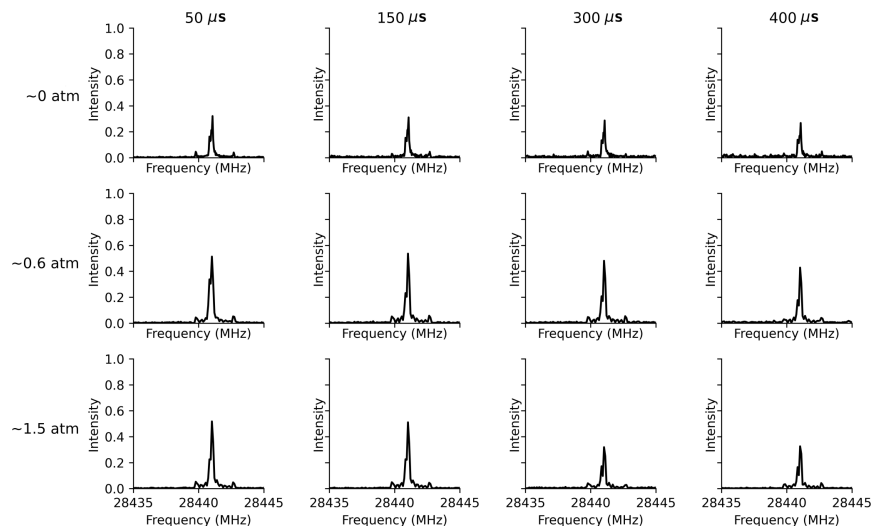


Figure 6.10: Comparison of four gas pulse width settings and four backing pressures for the acrylonitrile.

transitions.

6.5 Results

Twelve different experiments were conducted to compare which combination of four gas pulse widths and three backing pressures produced the most intense rotational transition. Figure 6.10 shows the normalized $3_{03} - 2_{02}$ rotational transition of acrylonitrile with the following combinations of gas pulse widths ($50 \mu\text{s}$, $150 \mu\text{s}$, $300 \mu\text{s}$, and $400 \mu\text{s}$) and backing pressures (0 atm, 0.6 atm, and 1.5 atm). For each given experiment, the chirp delay and voltage applied to the piezo were adjusted manually to achieve the strongest signal, the concentration of acrylonitrile was held constant at 1%, and five microwave chirps were averaged per gas pulse. As indicated in Figure 6.10, evidence suggests that a small gas pulse width ($\approx 50 \mu\text{s}$) and a high backing pressure (1.5 atm) achieved the strongest signal. Therefore, all future experiments used these settings.

The final spectrum of pyridine and acrylonitrile, after optimizing the Ka-band CP-FTMW spectrometer, are shown in Figure 6.11. For pyridine, 17000 FIDs were averaged in five hours of integration time at a pulsed valve repetition rate of 1 Hz. 38 lines were measured

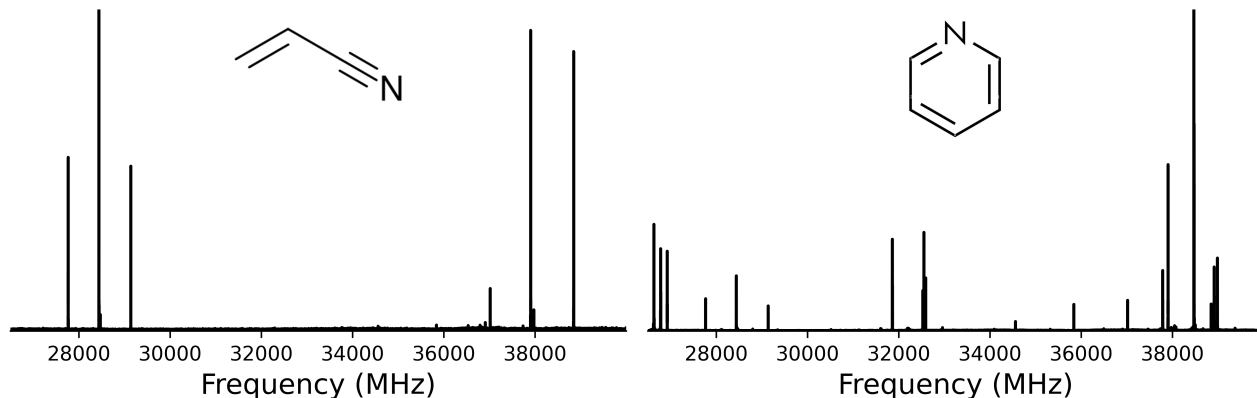


Figure 6.11: Ka-band CP-FTMW spectrum of acrylonitrile (left) and pyridine (right). For acrylonitrile, a constant backing pressure of 2225 Torr of a $\approx 1\%$ acrylonitrile in Ar pre-made mixture was delivered to the pulsed valve. The piezo voltage was 220 V with a gas pulse width of 150 μs . For pyridine, a constant backing pressure of 1800 Torr in Ar was delivered to the pulsed valve via a glass bubbler. The piezo voltage was 390 V with a gas pulse width of 50 μs . Intensities not to scale.

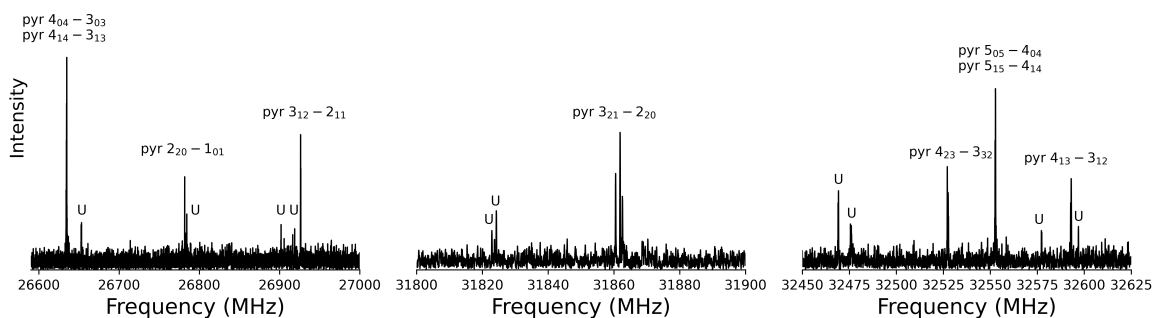


Figure 6.12: Segments of the pyridine discharge spectrum showing rotational transitions for the parent molecule and U lines.

up to $J = 10$, the majority of which are R-branch transitions. The list of experimental transition frequencies with their quantum number assignments can be seen in Table 6.1.[196, 228] For the pyridine discharge experiments, many discharge lines were produced (examples in Figure 6.12) and the observed rotational transitions are in Table 6.2. It can be seen that cyanovinylacetylene (HC_2CHCHCN) and cyanoacetylene occur most often, while the remaining peaks are still U lines.

The rotational temperature of the free jet expansion for pyridine was estimated using

Table 6.1: Observed rotational transitions of pyridine.

$J'_{Ka'Kc'} - J''_{Ka''Kc''}$	ν_0 (MHz)	Intensity (a.u.)	$J'_{Ka'Kc'} - J''_{Ka''Kc''}$	ν_0 (MHz)	Intensity (a.u.)
$3_{2,2} - 2_{2,1}$	26291.06	9.69	$4_{1,3} - 3_{1,2}$	32593.03	26.43
$3_{2,2} - 2_{2,1}$	26292.63	10.55	$4_{3,2} - 3_{3,1}$	37786.08	24.64
$3_{2,2} - 2_{2,1}$	26292.92	0.65	$4_{3,2} - 3_{3,1}$	37787.55	30.12
$6_{2,4} - 6_{2,5}$	26623.56	2.43	$4_{3,2} - 3_{3,1}$	37788.13	15.88
$6_{3,4} - 6_{1,5}$	26624.27	3.72	$10_{4,6} - 10_{4,7}$	38438.15	1.57
$4_{1,4} - 3_{1,3}$	26634.48	49.15	$10_{5,6} - 10_{3,7}$	38438.55	1.42
$5_{1,4} - 5_{1,5}$	26636.38	6.76	$4_{2,2} - 3_{2,1}$	38469.15	8.15
$2_{2,0} - 1_{0,1}$	26778.82	10.21	$8_{2,6} - 8_{2,7}$	38471.05	160.13
$2_{2,0} - 1_{0,1}$	26781.68	40.99	$5_{2,4} - 4_{2,3}$	38473.44	49.78
$2_{2,0} - 1_{0,1}$	26784.35	19.62	$5_{2,4} - 4_{2,3}$	38473.72	103.39
$3_{1,2} - 2_{1,1}$	26926.16	39.74	$5_{1,4} - 4_{1,3}$	38476.87	34.88
$3_{2,1} - 2_{2,0}$	31860.52	25.63	$5_{1,4} - 4_{1,3}$	38477.16	73.07
$3_{2,1} - 2_{2,0}$	31861.85	45.69	$7_{1,6} - 7_{1,7}$	38480.73	5.36
$3_{2,1} - 2_{2,0}$	31862.57	22.94	$3_{3,0} - 2_{1,1}$	38914.65	14.71
$4_{2,3} - 3_{2,2}$	32527.13	19.07	$3_{3,0} - 2_{1,1}$	38915.37	31.88
$4_{2,3} - 3_{2,2}$	32527.56	20.11	$3_{3,0} - 2_{1,1}$	38917.18	17.37
$5_{1,5} - 4_{1,4}$	32552.50	21.95	$4_{2,2} - 3_{2,1}$	38987.32	8.52
$5_{0,5} - 4_{0,4}$	32552.79	42.31	$4_{2,2} - 3_{2,1}$	38987.56	36.33
$4_{1,3} - 3_{1,2}$	32592.75	16.23	$4_{2,2} - 3_{2,1}$	38987.85	27.47

Table 6.2: Observed rotational transitions of pyridine discharge.

ν_0 (MHz)	Name	$J'_{Ka'Ke'} - J''_{Ka''Ke''}$
27294.32	HC ₃ N (Cyanoacetylene)	3-2
28506.82	(Z)-HC ₂ CHCHCN ((Z)-Cyanovinylacetylene)	7 _{0,7} -6 _{1,6}
28753.06	(E)-HC ₂ CHCHCN ((E)-Cyanovinylacetylene)	10 _{1,10} -9 _{1,9}
28977.84	(E)-HC ₂ CHCHCN ((E)-Cyanovinylacetylene)	10 _{0,10} -9 _{0,9}
29115.51	(Z)-HC ₂ CHCHCN ((Z)-Cyanovinylacetylene)	6 _{1,5} -5 _{1,4}
31732.30	(Z)-HC ₂ CHCHCN ((Z)-Cyanovinylacetylene)	7 _{2,6} -6 _{2,5}
31817.08	U	
34770.08	(E)-HC ₂ CHCHCN ((E)-cyanovinylacetylene)	12 _{0,0} -11 _{0,11}
36392.38	HC ₃ N (cyanoacetylene)	4-3
36610.53	U	
37290.17	U	

a simulated spectrum from previously reported data.[98, 228, 229] The simulation included the Watson S-reduced parameters of the ground state rotational constants and centrifugal distortion terms (cubic and quartic force constants). Spin contributions from nitrogen quadrupole tensor are also included (diagonal elements). Results from the simulations estimate the rotational temperature to be ≈ 8 K approximately 150 mm downstream from the nozzle exit.

For acrylonitrile (Figure 6.11 (right)), this spectrum was collected with approximately 2000 FIDs averaged, which took approximately 30 minutes of integration time at a pulsed valve repetition rate of 1 Hz. Fewer acrylonitrile transitions lie in the Ka-band compared to pyridine. Figure 6.11 shows two very strong sets of triplet peaks in this frequency range that correspond to the 3 - 2 transitions ($3_{13} - 2_{12}$, $3_{03} - 2_{02}$, and $3_{12} - 2_{11}$) and 4 - 3 transitions ($4_{14} - 3_{13}$, $4_{04} - 3_{03}$, $4_{13} - 3_{12}$).

Table 6.3: Experimental ground state rotational constants, centrifugal distortion constants, and N-quadrupole terms for pyridine determined via microwave spectroscopy (in MHz) used to estimate the experimental rotational temperature.[196, 228, 229]

Parameter	Pyridine
A_0	6039.24
B_0	5804.90
C_0	2959.22
$(10^{-3})D_J$	1.70
$(10^{-3})D_{JK}$	-2.25
$(10^{-3})D_J$	1.01
$(10^{-6})d_1$	-6.88
$(10^{-5})d_2$	-2.06
$(10^{-9})H_K$	-1.22
$(10^{-9})H_{KJ}$	3.13
$(10^{-9})H_{JK}$	-2.52
$(10^{-10})H_J$	6.60
χ_{aa}	-4.86
χ_{bb}	1.50
χ_{cc}	3.36

6.6 Conclusion

A Ka-band CP-FTMW spectrometer has been constructed, tested, and optimized and its performance assessed. During the extensive optimization phase, the results show that the Ka-band CP-FTMW spectrometer successfully measures the rotational spectra of closed-shell molecules: pyridine and acrylonitrile. Different discharge stack geometries were tested, and through those discharge experiments of pyridine and acrylonitrile, the Ka-band spectrometer measured many U lines that still need to be identified. Various pulsed gas width/delay timings were evaluated in relation to the chirp excitation and it was determined that a small gas pulse width ($50\mu\text{s}$) with a chirp delay of $600\mu\text{s}$ relative to the gas pulse was optimal. In addition, the signal intensity levels of specific rotational transitions for pyridine were investigated and the results were used to determine the most optimal linear sweep rate for future experiments, which was on order of $0.8\text{ MHz } \mu\text{s}^{-1}$. Despite many attempts to

measure radicals, specifically the pyridyl radicals, no conclusive identification was made. Several modifications would benefit this instrument, including a larger vacuum chamber and more powerful vacuum pumps, as well as a redesign of the discharge stack to study the effects of different geometries on a supersonic expansion.

Appendix A

Rotational and Vibrational Spectroscopy of the Pyridyl Radicals: A Coupled Cluster Study Supporting Information

Table A.1: Filenames and descriptions of the outputs for 2- and 3-pyridyl.

2-pyridyl	
2pZMATcartesian.txt	Final geometry at ae-CCSD(T)/cc-pwCVTZ.
2pnormalcoord.txt	Normal coordinates of vibration.
2pvibcorrections.txt	Vibrational corrections to the rotational constants (MHz) at fc-CCSD(T)/ANO0.
2pfinalvibquanta.csv	*Vibrational frequencies (cm^{-1}) and intensities (km/mol) up to 3 quanta with VPT2/VPT2+K corrections at fc-CCSD(T)/ANO0.
2p.var	SPCAT input file with control flags and values of constants.
2p.int	SPCAT input file with information for intensity calculation.
2pguineaA1.txt	GUINEA input file for A' states.
2pguineaA2.txt	GUINEA input file for A'' states.
2pheatmapA1.png	Variational coefficients for anharmonic vibrational states for A' states.
2pheatmapA2.png	Variational coefficients for anharmonic vibrational states for A'' states.
3-pyridyl	
3pZMATcartesian.txt	Final geometry at ae-CCSD(T)/cc-pwCVTZ.
3pnormalcoord.txt	Normal coordinates of vibration.
3pvibcorrections.txt	Vibrational corrections to the rotational constants (MHz) at fc-CCSD(T)/ANO0.
3pfinalvibquanta.csv	*Vibrational frequencies (cm^{-1}) and intensities (km/mol) up to 3 quanta with VPT2/VPT2+K corrections at fc-CCSD(T)/ANO0.
3p.var	SPCAT input file with control flags and values of constants.
3p.int	SPCAT input file with information for intensity calculation.
3pguineaA1.txt	GUINEA input file for A' states.
3pguineaA2.txt	GUINEA input file for A'' states.
3pheatmapA1.png	Variational coefficients for anharmonic vibrational states for A' states.
3pheatmapA2.png	Variational coefficients for anharmonic vibrational states for A'' states.

*To avoid adding quote characters to the filenames and .csv entries, A' states for 2- and 3- pyridyl are labeled A1, and A'' states are labeled as A2.

Table A.2: Filenames and descriptions of the outputs for 4-pyridyl.

4-pyridyl	
4pZMATcartesian.txt	Final geometry at ae-CCSD(T)/cc-pwCVTZ.
4pnormalcoord.txt	Normal coordinates of vibration.
4pvibcorrections.txt	Vibrational corrections to the rotational constants (MHz) at fc-CCSD(T)/ANO0.
4pfinalvibquanta.csv	Vibrational frequencies (cm^{-1}) and intensities (km/mol) up to 3 quanta with VPT2/VPT2+K corrections at fc-CCSD(T)/ANO0.
4p.var	SPCAT input file with control flags and values of constants.
4p.int	SPCAT input file with information for intensity calculation.
4pguineaA1.txt	GUINEA input file for A_1 states.
4pguineaA2.txt	GUINEA input file for A_2 states.
4pguineaB1.txt	GUINEA input file for B_1 states.
4pguineaB2.txt	GUINEA input file for B_2 states.
4pheatmapA1.png	Variational coefficients for anharmonic vibrational states for A_1 states.
4pheatmapA2.png	Variational coefficients for anharmonic vibrational states for A_2 states.
4pheatmapB1.png	Variational coefficients for anharmonic vibrational states for B_1 states.
4pheatmapB2.png	Variational coefficients for anharmonic vibrational states for B_2 states.

Table A.3: Calculated spin-spin tensors at ae-CCSD(T)/cc-pwCVTZ for 2-, 3-, and 4-pyridyl, in MHz.

	2-pyridyl					3-pyridyl				
	N1	H3	H4	H5	H6	N1	H2	H4	H5	H6
T_{aa}	-1.75	14.53	0.45	-2.38	0.30	0.74	12.42	12.55	0.93	-1.77
T_{bb}	4.64	-7.02	2.36	4.04	4.42	5.91	-5.80	-6.00	2.41	3.65
T_{cc}	-2.89	-7.51	-2.81	-1.66	-4.72	-6.65	-6.61	-6.56	-3.34	-1.88
T_{ab}	-6.20	0.80	-0.65	0.02	3.21	-6.23	-0.51	3.51	1.70	-0.31
T_{ac}	0.00	0.00	0.00	0.00	0.00	0.00	0.00	0.00	0.00	0.00
T_{bc}	0.00	0.00	0.00	0.00	0.00	0.00	0.00	0.00	0.00	0.00

	4-pyridyl		
	N1	H2	H3
T_{aa}	-1.10	1.30	13.31
T_{bb}	-0.14	1.92	-6.70
T_{cc}	1.24	-3.21	-6.62
T_{ab}	0.00	-1.40	-1.75
T_{ac}	0.00	0.00	0.00
T_{bc}	0.00	0.00	0.00

Table A.4: Calculated electronic N-quadrupole tensors at ae-CCSD(T)/cc-pwCVTZ for 2-, 3-, and 4-pyridyl, in MHz.

	2-pyridyl	3-pyridyl	4-pyridyl
χ_{aa}	-3.54	-3.98	1.52
χ_{bb}	7.46	0.58	-4.91
χ_{cc}	2.79	3.40	3.38
χ_{ab}	2.08	2.11	0.00
χ_{ac}	0.00	0.00	0.00
χ_{bc}	0.00	0.00	0.00

Table A.5: Calculated electronic spin-rotation tensors at fc-CCSD(T)/ANO0 for 2-, 3-, and 4-pyridyl, in MHz.

	2-pyridyl			3-pyridyl			4-pyridyl		
	J_x	J_y	J_z	J_x	J_y	J_z	J_x	J_y	J_z
S_x	23.88	8.97	0.00	10.52	1.43	0.00	-4.64	0.00	0.00
S_y	7.28	3.79	0.00	1.50	2.96	0.00	0.00	10.01	0.00
S_z	0.00	0.00	-6.15	0.00	0.00	-5.17	0.00	0.00	2.16

Table A.6: 2-pyridyl fc-CCSD(T)/ANO0 harmonic (ω) vibrational frequencies (cm^{-1}) and intensities (km/mol) with previous DFT harmonic frequencies.

Mode ^a	Sym.	DFT				This Work	
		Ref. 189 ^b	Ref. 188 ^c	Ref. 183 ^d	Ref. 230 ^e	ω	Int.
ν_1	A'	3204		3200	3223	3237.0	3.02
ν_2	A'	3197		3194	3215	3227.8	10.74
ν_3	A'	3178		3173	3193	3202.1	13.21
ν_4	A'	3165		3162	3182	3193.1	1.99
ν_5	A'	1662		1660	1675	1676.0	41.87
ν_6	A'	1572		1567	1589	1611.6	17.79
ν_7	A'	1502		1496	1515	1493.8	2.24
ν_8	A'	1424		1419	1436	1419.8	17.52
ν_9	A'	1335		1330	1348	1318.3	5.66
ν_{10}	A'	1265		1260	1278	1237.9	0.33
ν_{11}	A'	1169		1165	1177	1156.6	2.49
ν_{12}	A'	1108		1107	1116	1113.3	0.15
ν_{13}	A'	1074	1074	1072	1084	1071.9	8.70
ν_{14}	A'	1035	1037	1033	1042	1032.9	0.78
ν_{15}	A'	956	956	953	951	949.4	17.82
ν_{16}	A'	663	663	662	663	657.8	0.62
ν_{17}	A'	578	578	578	574	569.3	10.39
ν_{18}	A''	993	1012	989	998	1018.7	0.07
ν_{19}	A''	961	975	962	963	986.8	0.06
ν_{20}	A''	885	893	886	891	900.2	0.07
ν_{21}	A''	749	755	750	756	762.3	45.26
ν_{22}	A''	703	716	699	704	713.8	7.96
ν_{23}	A''	425		422	426	427.6	0.11
ν_{24}	A''	385		382	387	387.2	5.73

^a Normal modes as numbered in the Herzberg convention.

^b B3LYP/6-311+G*

^c B3LYP/cc-pVTZ

^d B3LYP/6-311++G**

^e B3LYP/6-31G*

Table A.7: 3-pyridyl fc-CCSD(T)/ANO0 harmonic (ω) vibrational frequencies (cm^{-1}) and intensities (km/mol) with previous DFT harmonic frequencies.

Mode ^a	Sym.	DFT				This Work	
		Ref. 189 ^b	Ref. 188 ^c	Ref. 183 ^d	Ref. 230 ^e	ω	Int.
ν_1	A'	3184		3202	3205	3219.4	5.11
ν_2	A'	3178		3190	3198	3207.8	7.36
ν_3	A'	3167		3185	3188	3203.7	11.12
ν_4	A'	3156		3168	3174	3184.9	7.37
ν_5	A'	1613		1627	1629	1644.2	11.20
ν_6	A'	1543	1542	1557	1560	1576.8	8.22
ν_7	A'	1473	1471	1478	1484	1470.4	3.29
ν_8	A'	1442	1440	1448	1454	1437.5	18.60
ν_9	A'	1333	1331	1335	1343	1323.3	1.07
ν_{10}	A'	1263	1260	1286	1287	1207.8	4.56
ν_{11}	A'	1206	1203	1209	1213	1202.5	1.76
ν_{12}	A'	1110	1109	1115	1119	1099.4	6.02
ν_{13}	A'	1065	1066	1072	1074	1067.7	7.66
ν_{14}	A'	1044	1047	1048	1050	1051.6	0.99
ν_{15}	A'	990	991	987	988	985.1	7.14
ν_{16}	A'	662	662	662	662	652.9	2.27
ν_{17}	A'	581	580	577	578	578.2	15.57
ν_{18}	A''	981	998	985	983	1001.5	0.07
ν_{19}	A''	939	951	945	944	960.9	0.09
ν_{20}	A''	916	927	921	921	938.8	0.65
ν_{21}	A''	779	788	785	785	791.3	26.55
ν_{22}	A''	684	692	688	688	695.8	32.65
ν_{23}	A''	421		423	424	420.7	0.03
ν_{24}	A''	389		390	391	394.5	2.62

^a Normal modes as numbered in the Herzberg convention.

^b B3LYP/6-311+G*

^c B3LYP/cc-pVTZ

^d B3LYP/6-311++G**

^e B3LYP/6-31G*

Table A.8: 4-pyridyl fc-CCSD(T)/ANO0 harmonic (ω) vibrational frequencies (cm^{-1}) and intensities (km/mol) with previous DFT harmonic frequencies.

Mode ^a	Sym.	DFT				This Work	
		Ref. 189 ^b	Ref. 188 ^c	Ref. 183 ^d	Ref. 230 ^e	ω	Int.
ν_1	A_1	3187		3184	3209	3225.1	0.02
ν_2	A_1	3151		3145	3167	3178.2	5.33
ν_3	A_1	1543	1539	1536	1560	1584.9	42.70
ν_4	A_1	1476	1476	1468	1490	1479.1	9.51
ν_5	A_1	1233	1230	1228	1241	1235.5	3.04
ν_6	A_1	1080	1080	1073	1085	1078.6	8.66
ν_7	A_1	1038	1041	1036	1044	1047.8	1.28
ν_8	A_1	983	982	981	980	981.3	22.05
ν_9	A_1	620		619	616	608.3	0.13
ν_{10}	A_2	973	990	978	976	1002.4	0.00
ν_{11}	A_2	817	831	825	831	846.9	0.00
ν_{12}	A_2	376		377	380	382.8	0.00
ν_{13}	B_1	951	968	956	959	975.4	0.01
ν_{14}	B_1	760	772	767	770	776.8	43.64
ν_{15}	B_1	708		707	709	717.8	6.11
ν_{16}	B_1	443		442	446	443.2	14.41
ν_{17}	B_2	3185		3183	3207	3224.3	5.51
ν_{18}	B_2	3149		3143	3165	3176.5	21.88
ν_{19}	B_2	1619	1618	1615	1633	1642.1	25.93
ν_{20}	B_2	1413	1409	1405	1423	1408.0	16.87
ν_{21}	B_2	1322	1322	1316	1334	1314.0	1.24
ν_{22}	B_2	1269	1266	1265	1292	1208.7	1.57
ν_{23}	B_2	1076	1080	1077	1088	1076.4	0.99
ν_{24}	B_2	647		644	646	639.1	0.12

^a Normal modes as numbered in the Herzberg convention.

^b B3LYP/6-311+G*

^c B3LYP/cc-pVTZ

^d B3LYP/6-311++G**

^e B3LYP/6-31G*

Table A.9: 2-pyridyl fc-CCSD(T)/ANO0 harmonic, VPT2+K anharmonic vibrational frequencies for combination/overtone bands (cm^{-1}) and intensities (km/mol) with photoelectron spectroscopy values for comparison. Suggested alternative assignments are listed.

Mode ^a	Sym.	This Work		Experiment	Alternative Assignment
		ω	ν (VPT2+K)	Ref. 189 ^b	weight (Mode ^a) (MHz)
$\nu_{16} + \nu_{17}$	A'	1226.08	*1208.99	1216[7]	
$2\nu_{16}$	A'	1313.55	*1298.66	1298[7]	
$\nu_{15} + \nu_{16}$	A'	1606.18	^c *1582.83	1600[8]	$13^1 17^1$ (1607.38)
$\nu_{14} + \nu_{16}$	A'	1688.68	^c *1659.62	1659[7]	
$\nu_{13} + \nu_{16}$	A'	1727.70	*1691.25	1692[7]	$0.81(18^1 22^1) + 0.12(13^1 16^1)$ (1694.60) $11^1 17^1$ (1699.92)
$\nu_{12} + \nu_{16}$	A'	1770.04	*1748.42	1737[6]	
$\nu_{11} + \nu_{16}$	A'	1812.42	*1783.81	1789[8]	$11^1 16^1$ (1783.81)
$2\nu_{16} + \nu_{17}$	A'	1882.86	1861.31	1864[7]	15^2 (1868.44)
$3\nu_{16}$	A'	1970.33	1948.81	1947[7]	$14^1 15^1$ (1945.59), $8^1 17^1$ (1951.77)
$\nu_8 + \nu_{16}$	A'	2075.53	*2035.02	2039[7]	$12^1 15^1$ (2037.71)
$\nu_{13} + \nu_{14}$	A'	2102.84	2055.72	2049[7]	
$2\nu_{13}$	A'	2141.86	*2086.28	2082[7]	
$\nu_7 + \nu_{16}$	A'	2149.63	*2104.52	2112[7]	$12^1 14^1$ (2117.84)
$\nu_6 + \nu_{16}$	A'	2267.40	*2217.99	2185[7]	$11^1 13^1$ (2186.36)
$\nu_{15} + 2\nu_{16}$	A'	2262.96	2227.49	2246[7]	$11^1 12^1$ (2239.66), $10^1 13^1$ (2249.61)
$\nu_{14} + 2\nu_{16}$	A'	2345.46	2316.25	2306[7]	$10^1 12^1$ (2305.18)
$\nu_{13} + 2\nu_{16}$	A'	2384.48	2344.29	2339[7]	$10^1 11^1$ (2343.39)

^a Normal modes as numbered in the Herzberg convention.

^b Photoelectron spectroscopy.

^c This is a heavily mixed state and the assigned label reflects the mode with the largest leading coefficient for that frequency. A singular mode assignment is not an accurate description for this frequency. Refer to

SI for more accurate assignments.

Intensity in parenthesis. Uncertainty in brackets.

* Variationally corrected.

Table A.10: 3-pyridyl fc-CCSD(T)/ANO0 harmonic, anharmonic, and deperturbed vibrational frequencies for combination/overtone bands (cm^{-1}) and intensities (km/mol) with photoelectron spectroscopy values for comparison.

Mode ^a	Sym.	This Work		Experiment	Alternative Assignment
		ω	ν (VPT2+K)	Ref. 189 ^b	weight (Mode ^a) (MHz)
$\nu_{16} + \nu_{17}$	A'	1231.04	1217.18	1216[6]	0.58(21 ¹ 23 ¹) + 0.32(11 ¹) (1212.07)
$2\nu_{16}$	A'	1305.78	*1292.05	1292[6]	9 ¹ (1290.32)
$\nu_{15} + \nu_{17}$	A'	1563.28	*1538.18	1543[9]	
$\nu_{15} + \nu_{16}$	A'	1638.02	*1615.47	1619[6]	15 ¹ 16 ¹ (1615.47), 19 ¹ 22 ¹ (1623.49)
$\nu_{14} + \nu_{16}$	A'	1704.54	*1678.70	1670[6]	18 ¹ 22 ¹ (1664.10)
$\nu_{13} + \nu_{16}$	A'	1720.63	*1687.69	1695[6]	20 ¹ 21 ¹ (1693.48)
$\nu_{12} + \nu_{16}$	A'	1752.27	1729.62	1731[6]	
$2\nu_{16} + \nu_{17}$	A'	1883.93	1863.96	1862[6]	0.49(9 ¹ 17 ¹) + 0.45(19 ¹ 20 ¹) (1862.07) 0.50(9 ¹ 17 ¹) + 0.46(19 ¹ 20 ¹) (1865.29)
$3\nu_{16}$	A'	1958.67	1938.87	1940[7]	15 ² (1938.22)
$\nu_{14} + \nu_{15}$	A'	2036.78	*2002.55	1998[9]	7 ¹ 17 ¹ (2007.88)
$\nu_{13} + \nu_{15}$	A'	2052.87	*2010.92	2021[6]	
$\nu_6 + \nu_{16}$	A'	2229.73	*2174.03	2151[7]	12 ¹ 15 ¹ (2051.68) 8 ¹ 16 ¹ (2054.20)
$\nu_{15} + \nu_{16} + \nu_{17}$	A'	2216.17	2183.72	2188[6]	0.51(11 ¹ 14 ¹) + 0.41(11 ¹ 13 ¹) (2192.61)
$\nu_{15} + 2\nu_{16}$	A'	2290.91	2259.89	2265[6]	10 ¹ 12 ¹ (2268.35)
$\nu_{14} + 2\nu_{16}$	A'	2357.43	2323.81	2315[6]	11 ² (2313.24)
$\nu_{13} + 2\nu_{16}$	A'	2373.52	2333.09	2340[5]	0.78(10 ¹ 11 ¹) + 0.15(9 ¹ 13 ¹) (2340.82)
$\nu_{14} + \nu_{15} + \nu_{16}$	A'	2689.67	2645.42	2642[6]	
$\nu_{13} + \nu_{15} + \nu_{16}$	A'	2705.76	2654.82	2665[6]	
$\nu_{12} + \nu_{15} + \nu_{16}$	A'	2737.40	2696.63	2704[5]	8 ¹ 9 ¹ (2698.74)

^a Normal modes as numbered in the Herzberg convention.

^b Photoelectron spectroscopy.

Intensity in parenthesis. Uncertainty in brackets.

* Variationally corrected.

Table A.11: 4-pyridyl fc-CCSD(T)/ANO0 harmonic, anharmonic, and deperturbed vibrational frequencies for combination/overtone bands (cm^{-1}) and intensities (km/mol) with photoelectron spectroscopy values for comparison.

Mode ^a	Sym.	This Work		Experiment	Alternative Assignment
		ω	ν (VPT2+K)	Ref. 189 ^b	weight (Mode ^a) (MHz)
$2\nu_9$	A_1	1216.51	*1203.87	1207[5]	5^1 (1209.59)
$\nu_8 + \nu_9$	A_1	1589.59	*1565.67	1570[6]	
$\nu_7 + \nu_9$	A_1	1656.06	*1632.82	1622[6]	
$\nu_8 + 2\nu_{16}$	A_1	1867.76	1837.91	1804[5]	
$3\nu_9$	A_1	1824.77	1805.63	1813[5]	
$2\nu_8$	A_1	1962.67	*1927.12	1933[6]	
$\nu_7 + \nu_8$	A_1	2029.13	*1992.69	1983[5]	
$\nu_4 + \nu_9$	A_1	2087.32	*2044.90	2045[6]	
$\nu_3 + \nu_9$	A_1	2193.16	2132.85	2110[6]	6^2 (2109.36)
$\nu_8 + 2\nu_9$	A_1	2197.85	2171.90	2173[6]	$5^1 8^1$ (2179.70)
$\nu_7 + 2\nu_9$	A_1	2264.31	2233.28	2225[6]	
$2\nu_8 + \nu_9$	A_1	2570.92	2533.31	2531[7]	
$\nu_7 + \nu_8 + \nu_9$	A_1	2637.39	2596.38	2585[6]	
$2\nu_7 + \nu_9$	A_1	2703.86	2658.58	2640[7]	
$\nu_3 + 2\nu_9$	A_1	2801.42	2729.69	2707[8]	

^a Normal modes as numbered in the Herzberg convention.

^b Photoelectron spectroscopy.

Intensity in parenthesis. Uncertainty in brackets.

* Variationally corrected.

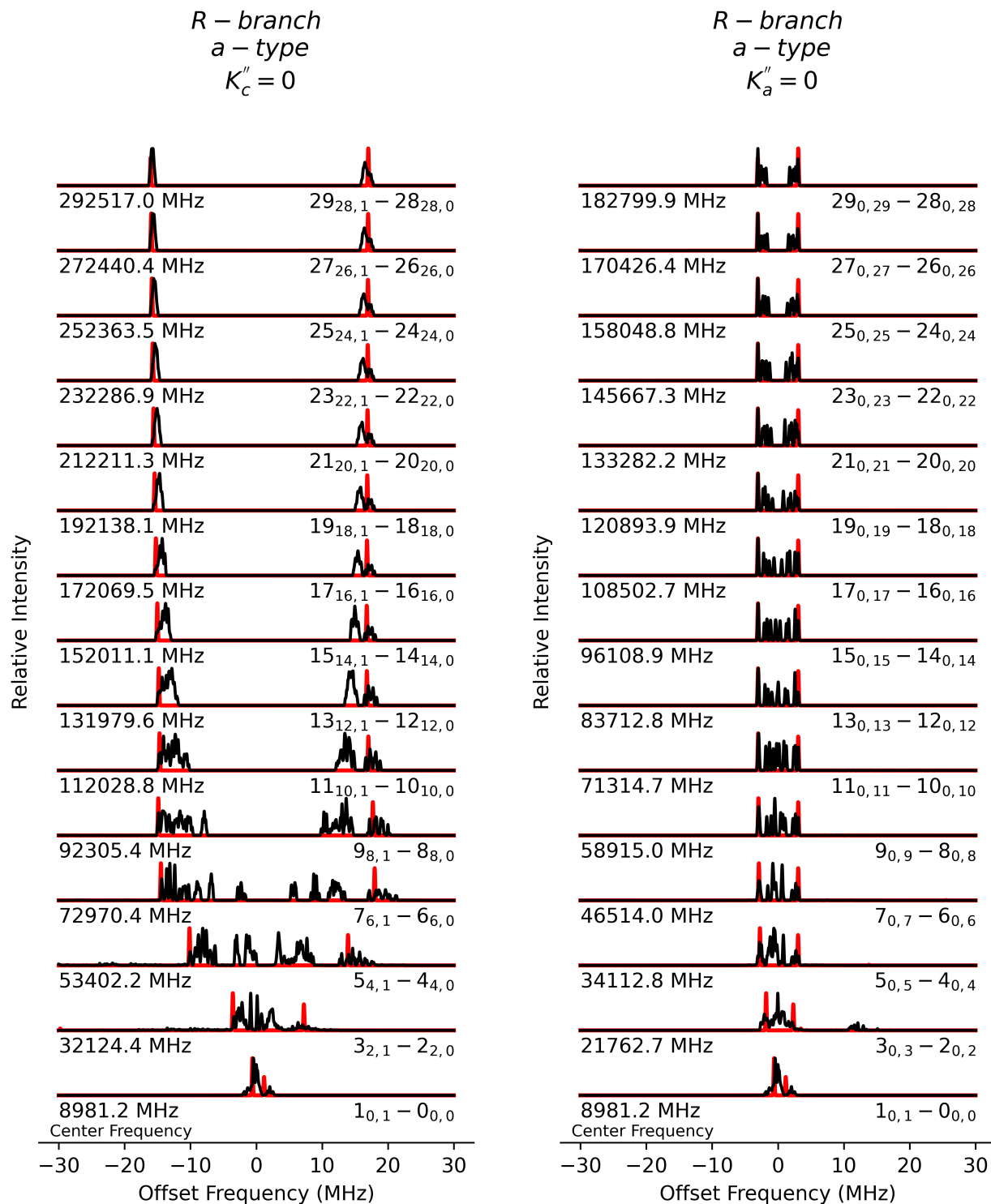


Figure A.1: Hyperfine collapse with increased N for 2-pyridyl. Selected R-branch a-type transitions with $K_c'' = 0$ (left) and $K_a'' = 0$ (right) for even N'' . Simulated at $T = 50K$. Convolved to 100 kHz. black: includes all spectroscopic parameters; red: only spin-rotation splitting

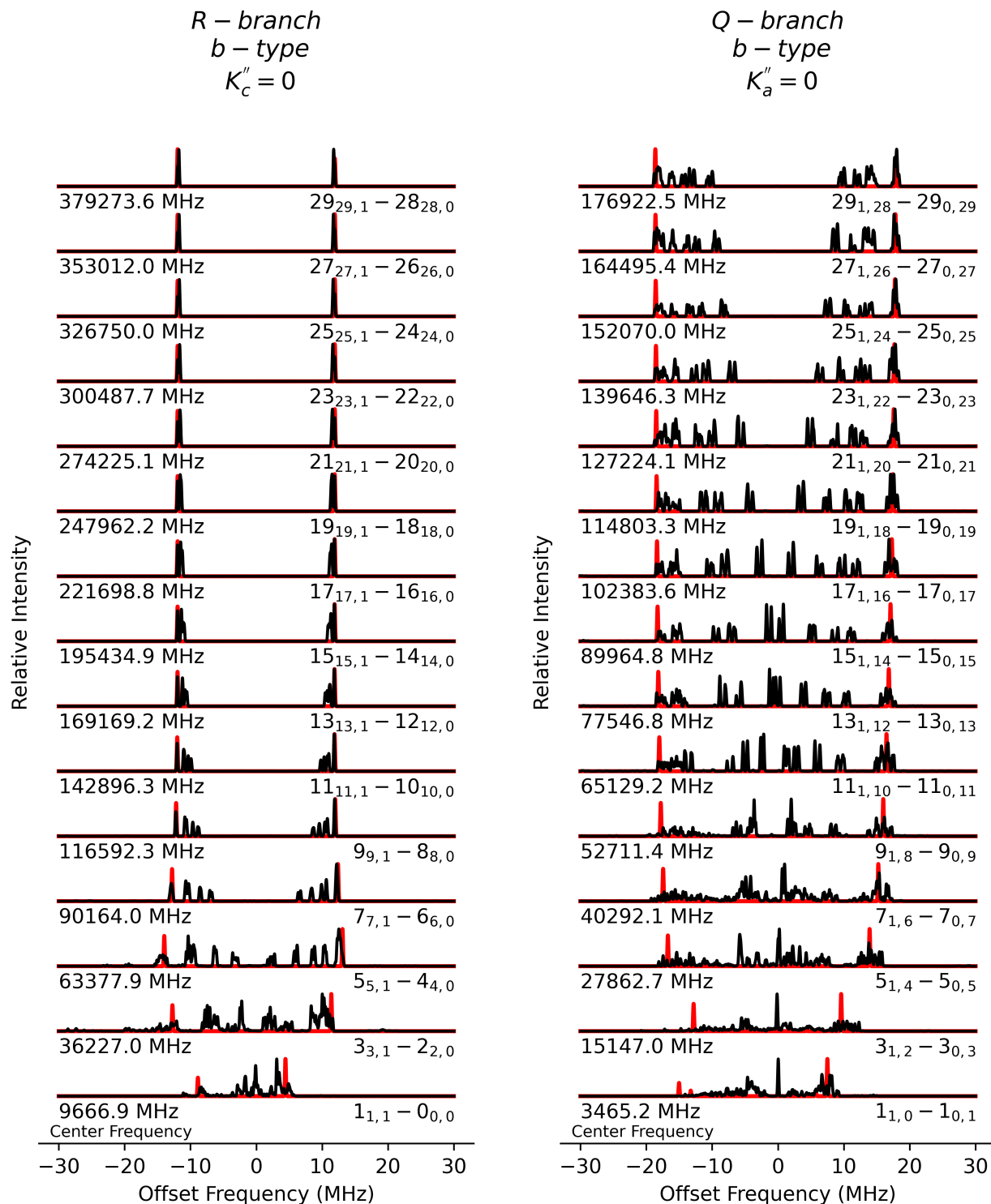


Figure A.2: Hyperfine collapse with increased N for 2-pyridyl. Selected R-branch b-type transitions with $K_c'' = 0$ (left) and Q-branch b-type transitions with $K_a'' = 0$ (right) for even N'' . Simulated at $T = 50K$. Convolved to 100 kHz. black: includes all spectroscopic parameters; red: only spin-rotation splitting

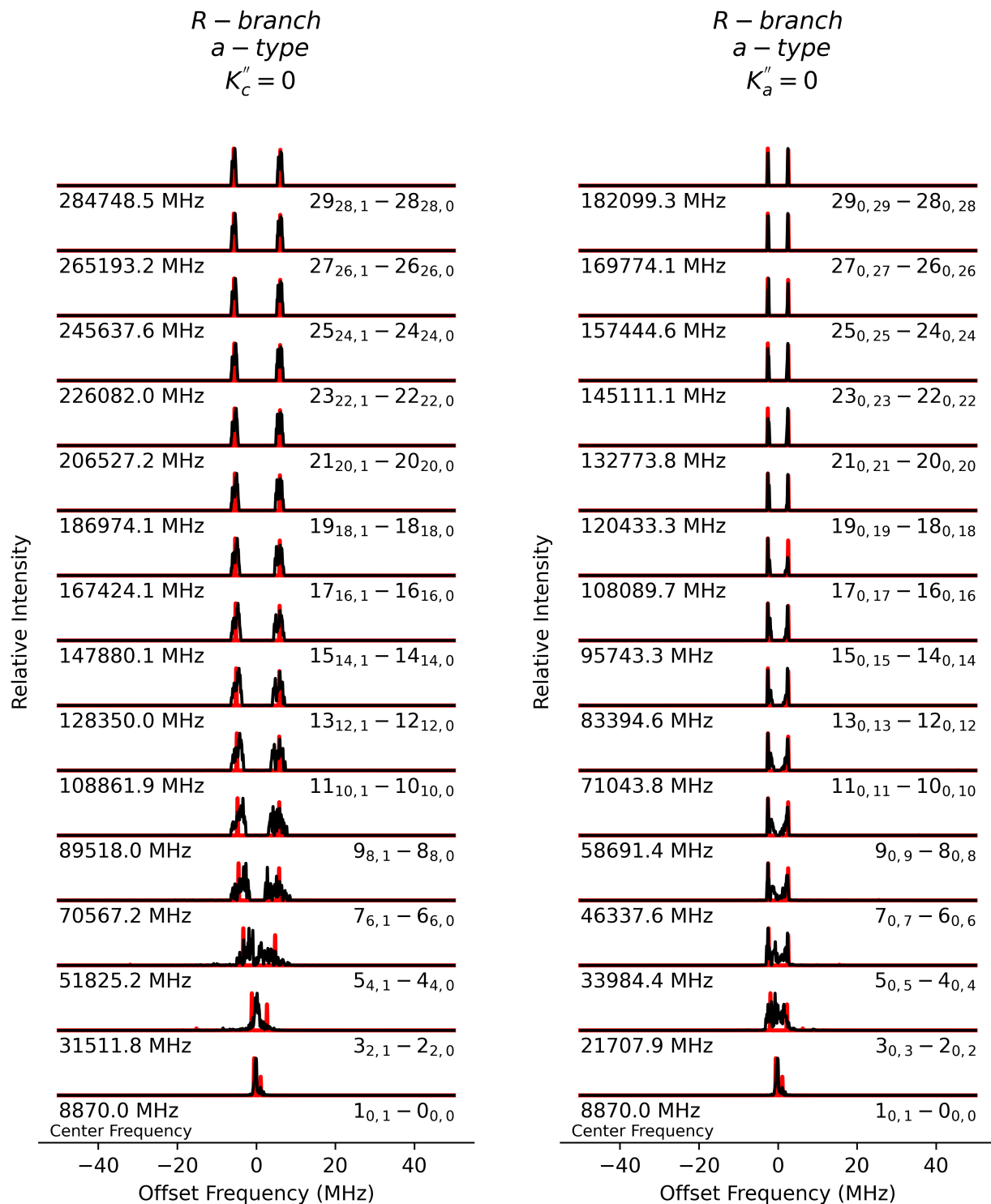


Figure A.3: Hyperfine collapse with increased N for 3-pyridyl. Selected R-branch a-type transitions with $K_c'' = 0$ (left) and $K_a'' = 0$ (right) for even N'' . Simulated at $T = 50K$. Convolved to 100 kHz. black: includes all spectroscopic parameters; red: only spin-rotation splitting

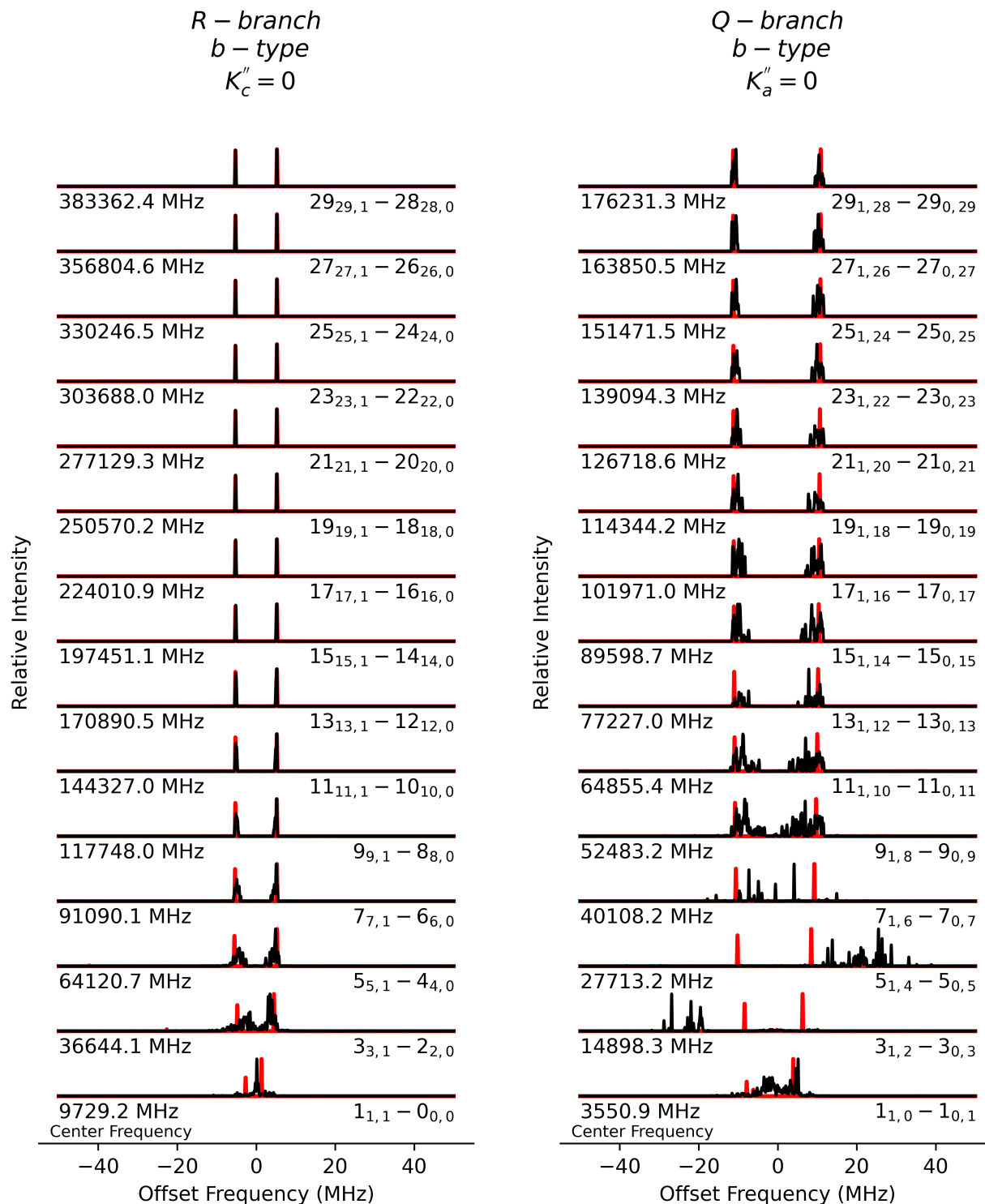


Figure A.4: Hyperfine collapse with increased N for 3-pyridyl. Selected R-branch *b*-type transitions with $K_c'' = 0$ (left) and Q-branch *b*-type transitions with $K_a'' = 0$ (right) for even N'' . Simulated at $T = 50K$. Convolved to 100 kHz. black: includes all spectroscopic parameters; red: only spin-rotation splitting

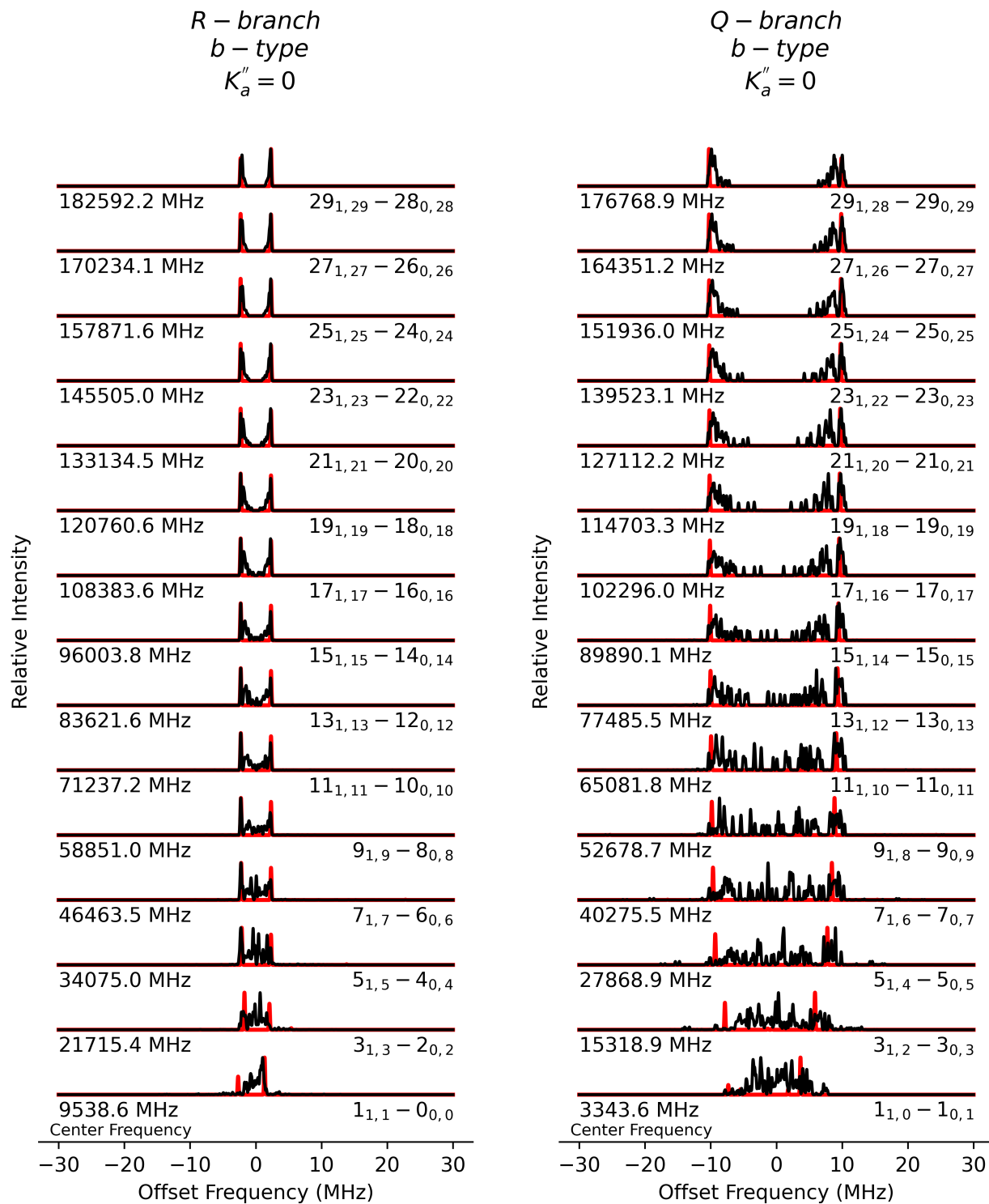


Figure A.5: Hyperfine collapse with increased N for 4-pyridyl. Selected R-branch (left) and Q-branch (right) b-type transitions with $K_a'' = 0$ for even N'' . Simulated at $T = 50K$. Convolved to 100 kHz. black: includes all spectroscopic parameters; red: only spin-rotation splitting

REFERENCES

- [1] E. Herbst, “Three milieux for interstellar chemistry: gas, dust, and ice,” *Phys. Chem. Chem. Phys.*, vol. 16, pp. 3344–3359, 2014. [Online]. Available: <http://dx.doi.org/10.1039/C3CP54065K>
- [2] A. M. Tielens, “The molecular universe,” *Rev. Mod. Phys.*, vol. 85, no. 3, pp. 1021–1081, 2013. [Online]. Available: <https://doi.org/10.1103/RevModPhys.85.1021>
- [3] P. Caselli and C. Ceccarelli, “Our astrochemical heritage,” *Astron. Astrophys. Rev.*, vol. 20, no. 1, p. 56, 2012. [Online]. Available: <https://doi.org/10.1007/s00159-012-0056-x>
- [4] B. A. McGuire, “2021 Census of Interstellar, Circumstellar, Extragalactic, Protoplanetary Disk, and Exoplanetary Molecules,” *Astrophys. J. Suppl. Ser.*, vol. 259, no. 2, p. 30, mar 2022. [Online]. Available: <https://doi.org/10.3847/2F1538-4365%2Fac2a48>
- [5] P. Swings and L. Rosenfeld, “Considerations Regarding Interstellar Molecules,” vol. 86, pp. 483–486, Nov. 1937. [Online]. Available: <https://ui.adsabs.harvard.edu/abs/1937ApJ....86..483S/abstract>
- [6] O. E. H. Rydbeck, J. Elldér, and W. M. Irvine, “Radio detection of interstellar CH,” *Nat.*, vol. 246, no. 5434, pp. 466–468, 1973. [Online]. Available: <https://www.nature.com/articles/246466a0>
- [7] S. R. Federman, C. J. Strom, D. L. Lambert, J. A. Cardelli, V. V. Smith, and C. L. Joseph, “Chemical Transitions for Interstellar C₂ and CN in Cloud Envelopes,” *Astrophys. J.*, vol. 424, p. 772, Apr. 1994. [Online]. Available: <https://ui.adsabs.harvard.edu/abs/1994ApJ...424..772F/abstract>
- [8] J. Maier, N. Lakin, G. Walker, and a. Bohlender, “Detection of C₃ in Diffuse

- Interstellar Clouds,” *Astrophys. J.*, vol. 553, p. 267, 12 2001. [Online]. Available: <https://iopscience.iop.org/article/10.1086/320668>
- [9] T. Oka, J. Dahlstrom, B. McCall, S. Friedman, L. Hobbs, P. Sonnentrucker, D. Welty, and D. York, “Observations of C₃ in Translucent Sight Lines,” *Astrophys. J.*, vol. 582, p. 823, 12 2003. [Online]. Available: <https://iopscience.iop.org/article/10.1086/344726>
- [10] J. A. Thorburn, L. M. Hobbs, B. J. McCall, T. Oka, D. E. Welty, S. D. Friedman, T. P. Snow, P. Sonnentrucker, and D. G. York, “Some Diffuse Interstellar Bands Related to Interstellar C₂ Molecules,” *Astrophys. J.*, vol. 584, no. 1, pp. 339–356, Feb. 2003. [Online]. Available: <https://ui.adsabs.harvard.edu/abs/2003ApJ...584..339T/abstract>
- [11] H. Liszt, R. Lucas, and J. Pety, “Millimeter-wave Observations of Polyatomic Molecules in Diffuse Clouds,” *Proc. Int. Astron. Union*, vol. 1, no. S231, pp. 187–196, 2005. [Online]. Available: <https://www.cambridge.org/core/journals/proceedings-of-the-international-astronomical-union/article/millimeterwave-observations-of-polyatomic-molecules-in-diffuse-clouds/51F1D4F68FF8419B230761D0D8803727>
- [12] E. Herbst and E. F. van Dishoeck, “Complex Organic Interstellar Molecules,” *Annu. Rev. Astron. Astrophys.*, vol. 47, no. 1, pp. 427–480, 2009. [Online]. Available: <https://doi.org/10.1146/annurev-astro-082708-101654>
- [13] S. E. Cummins, R. A. Linke, and P. Thaddeus, “A Survey of the Millimeter-Wave Spectrum of Sagittarius B2,” *Astrophys. J.*, vol. 60, p. 819, Mar. 1986. [Online]. Available: <https://ui.adsabs.harvard.edu/abs/1986ApJS...60..819C/abstract>
- [14] K. I. Öberg, S. Bottinelli, J. K. Jørgensen, and E. F. van Dishoeck, “A Cold Complex Chemistry Toward the Low-Mass Protostar B1-b: Evidence for Complex Molecule Production in Ices.” *Astrophys. J.*, vol. 716, no. 1, pp. 825–834, may 2010. [Online]. Available: <https://doi.org/10.1088/0004-637x/716/1/825>

- [15] A. A. Jaber, C. Ceccarelli, C. Kahane, and E. Caux, “The Census of Complex Organic Molecules in the Solar-Type Protostar IRAS 16293-2422,” *Astrophys. J.*, vol. 791, no. 1, p. 29, jul 2014. [Online]. Available: <https://doi.org/10.1088/0004-637x/791/1/29>
- [16] R. T. Garrod and E. Herbst, “Formation of methyl formate and other organic species in the warm-up phase of hot molecular cores,” *Astron. Astrophys.*, vol. 457, no. 3, pp. 927–936, 2006. [Online]. Available: <https://doi.org/10.1051/0004-6361:20065560>
- [17] S. Viti and D. A. Williams, “Time-dependent evaporation of icy mantles in hot cores,” *Mon. Not. R. Astron Soc.*, vol. 305, no. 4, pp. 755–762, 05 1999. [Online]. Available: <https://doi.org/10.1046/j.1365-8711.1999.02447.x>
- [18] V. Taquet, C. Ceccarelli, and C. Kahane, “Multilayer modeling of porous grain surface chemistry - I. The GRAINOBLE model,” *Astron. Astrophys.*, vol. 538, p. A42, 2012. [Online]. Available: <https://doi.org/10.1051/0004-6361/201117802>
- [19] A. Bacmann, V. Taquet, A. Faure, C. Kahane, and C. Ceccarelli, “Detection of complex organic molecules in a prestellar core: a new challenge for astrochemical models,” *Astron. Astrophys.*, vol. 541, p. L12, 2012. [Online]. Available: <https://doi.org/10.1051/0004-6361/201219207>
- [20] C. Vastel, C. Ceccarelli, B. Lefloch, and R. Bachiller, “The Origin of Complex Organic Molecules in Prestellar Cores,” *Astrophys. J.*, vol. 795, no. 1, p. L2, oct 2014. [Online]. Available: <https://doi.org/10.1088/0004-637x/795/1/L2>
- [21] D. S. N. Parker, T. Yang, B. B. Dangi, R. I. Kaiser, P. P. Bera, and T. J. Lee, “Low temperature formation of nitrogen-substituted polycyclic aromatic hydrocarbons (PANHs)—barrierless routes to dihydro(iso)quinolines.” *Astrophys. J.*, vol. 815, no. 2, p. 115, dec 2015. [Online]. Available: <https://iopscience.iop.org/article/10.1088/0004-637X/815/2/115>

- [22] D. S. N. Parker, R. I. Kaiser, O. Kostko, T. P. Troy, M. Ahmed, A. M. Mebel, and A. G. G. M. Tielens, “Gas phase synthesis of (iso)quinoline and its role in the formation of nucleobases in the interstellar medium.” *Astrophys. J.*, vol. 803, no. 2, p. 53, apr 2015. [Online]. Available: <https://doi.org/10.1088/0004-637x/803/2/53>
- [23] D. S. N. Parker, R. I. Kaiser, O. Kostko, T. P. Troy, M. Ahmed, B.-J. Sun, S.-H. Chen, and A. H. H. Chang, “On the formation of pyridine in the interstellar medium,” *Phys. Chem. Chem. Phys.*, vol. 17, no. 47, pp. 32 000–32 008, 2015. [Online]. Available: <http://dx.doi.org/10.1039/C5CP02960K>
- [24] R. J. Shannon, M. A. Blitz, A. Goddard, and D. E. Heard, “Accelerated chemistry in the reaction between the hydroxyl radical and methanol at interstellar temperatures facilitated by tunnelling,” *Nat. Chem.*, vol. 5, no. 9, pp. 745–749, 2013. [Online]. Available: <https://doi.org/10.1038/nchem.1692>
- [25] I. R. Sims and I. W. Smith, “Gas-phase reactions and energy transfer at very low temperatures,” *Annu. Rev. Phys. Chem.*, vol. 46, no. 1, pp. 109–138, 1995. [Online]. Available: <https://www.annualreviews.org/doi/10.1146/annurev.pc.46.100195.000545>
- [26] E. Herbst, “The synthesis of large interstellar molecules,” *Int. Rev. Phys. Chem.*, vol. 36, no. 2, pp. 287–331, 2017. [Online]. Available: <https://doi.org/10.1080/0144235X.2017.1293974>
- [27] Y. Yang, X. Hu, D. Zhang, W. Zhang, G. Liu, and J. Zhen, “Laboratory formation and photochemistry of covalently bonded polycyclic aromatic nitrogen heterocycle (PANH) clusters in the gas phase,” *Mon. Not. R. Astron Soc.*, vol. 498, no. 1, pp. 1–11, 07 2020. [Online]. Available: <https://doi.org/10.1093/mnras/staa2212>
- [28] R. I. Kaiser, D. S. Parker, and A. M. Mebel, “Reaction Dynamics in Astrochemistry: Low-Temperature Pathways to Polycyclic Aromatic Hydrocarbons in the Interstellar Medium,” *Ann. Phys. Chem.*, vol. 66, no. 1, pp. 43–67, 2015, pMID: 25422849. [Online]. Available: <https://doi.org/10.1146/annurev-physchem-040214-121502>

- [29] A. G. G. M. Tielens, “Interstellar polycyclic aromatic hydrocarbon molecules,” *Annu. Rev. Astron. Astrophys.*, vol. 46, no. 1, pp. 289–337, 2008. [Online]. Available: <https://doi.org/10.1146/annurev.astro.46.060407.145211>
- [30] L. J. Allamandola, A. G. G. M. Tielens, and J. R. Barker, “Polycyclic aromatic hydrocarbons and the unidentified infrared emission bands: Auto exhaust along the milky way!” *Astrophys. J.*, vol. 290, pp. L25–L28, 1985. [Online]. Available: <https://ui.adsabs.harvard.edu/abs/1985ApJ...290L..25A/abstract>
- [31] D. M. Hudgins, C. W. Bauschlicher, Jr., and L. J. Allamandola, “Variations in the peak position of the 6.2 μm interstellar emission feature: A tracer of N in the interstellar polycyclic aromatic hydrocarbon population,” *Astrophys. J.*, vol. 632, no. 1, pp. 316–332, oct 2005. [Online]. Available: <http://stacks.iop.org/0004-637X/632/i=1/a=316>
- [32] A. Leger and J. L. Puget, “Identification of the “unidentified” IR emission features of interstellar dust,” *Astron. Astrophys.*, vol. 137, pp. L5–L8, 1984. [Online]. Available: <https://adsabs.harvard.edu/full/1984A&A...137L...5L>
- [33] J. Cernicharo, A. M. Heras, A. G. G. M. Tielens, J. R. Pardo, F. Herpin, M. Guélin, and L. B. F. M. Waters, “*Infrared Space Observatory’s* Discovery of C_4H_2 , C_6H_2 , and Benzene in CRL 618,” *Astrophys. J.*, vol. 546, no. 2, pp. L123–L126, jan 2001. [Online]. Available: <https://doi.org/10.1086/318871>
- [34] A. M. Burkhardt, K. L. K. Lee, P. B. Changala, C. N. Shingledecker, I. R. Cooke, R. A. Loomis, H. Wei, S. B. Charnley, E. Herbst, M. C. McCarthy, and B. A. McGuire, “Discovery of the pure polycyclic aromatic hydrocarbon indene $\text{c-C}_9\text{H}_8$ with GOTHAM observations of TMC-1,” *Astrophys. J. Lett.*, vol. 913, no. 2, p. L18, may 2021. [Online]. Available: <https://doi.org/10.3847/2041-8213/abfd3a>
- [35] B. A. McGuire, “bmcguir2/astromol: 2021 Census Update Submission,” Jun. 2021. [Online]. Available: <https://doi.org/10.5281/zenodo.5046939>

- [36] L. M. Ziurys, “Interstellar Chemistry Special Feature: The chemistry in circumstellar envelopes of evolved stars: Following the origin of the elements to the origin of life,” *Proc. Nat. Acad. Sci.*, vol. 103, no. 33, pp. 12 274–12 279, Aug. 2006. [Online]. Available: <https://www.pnas.org/doi/full/10.1073/pnas.0602277103>
- [37] I. Cherchneff, “The formation of Polycyclic Aromatic Hydrocarbons in evolved circumstellar environments,” in *EAS Publications Series*, ser. EAS Publications Series, C. Joblin and A. G. G. M. Tielens, Eds., vol. 46, Mar. 2011, pp. 177–189. [Online]. Available: <https://doi.org/10.1051/eas/1146019>
- [38] B. Haynes and H. Wagner, “Soot formation,” *Prog. Energy Combust. Sci.*, vol. 7, no. 4, pp. 229–273, 1981. [Online]. Available: <https://www.sciencedirect.com/science/article/pii/0360128581900010>
- [39] J. Holdship, J. Rawlings, S. Viti, N. Balucani, D. Skouteris, and D. Williams, “Investigating the Efficiency of Explosion Chemistry as a Source of Complex Organic Molecules in TMC-1,” *Astrophys. J.*, vol. 878, no. 1, p. 65, jun 2019. [Online]. Available: <https://doi.org/10.3847/1538-4357/ab1f7b>
- [40] X. Lories, J. Vandooren, and D. Peeters, “Cycle formation from acetylene addition on C_4H_3 radicals,” *Phys. Chem. Chem. Phys.*, vol. 12, pp. 3762–3771, 2010. [Online]. Available: <http://dx.doi.org/10.1039/B921563H>
- [41] L. K. Madden, L. V. Moskaleva, S. Kristyan, and M. C. Lin, “Ab Initio MO Study of the Unimolecular Decomposition of the Phenyl Radical,” *J. Phys. Chem. A*, vol. 101, no. 36, pp. 6790–6797, Sep. 1997. [Online]. Available: <https://doi.org/10.1021/jp970723d>
- [42] J. P. Senosiain and J. A. Miller, “The reaction of n- and i- C_4H_5 radicals with acetylene.” *J. Phys. Chem. A*, vol. 111, pp. 3740–7, May 2007. [Online]. Available: <https://pubs.acs.org/doi/10.1021/jp0675126>

- [43] B. M. Jones, F. Zhang, R. I. Kaiser, A. Jamal, A. M. Mebel, M. A. Cordiner, and S. B. Charnley, "Formation of benzene in the interstellar medium," *Proc. Natl. Acad. Sci. U. S. A.*, vol. 108, no. 2, pp. 452–457, jan 2011. [Online]. Available: <https://www.pnas.org/content/108/2/452>
- [44] V. Vuitton, R. Yelle, and M. McEwan, "Ion chemistry and N-containing molecules in Titan's upper atmosphere," *Icarus*, vol. 191, no. 2, pp. 722–742, 2007. [Online]. Available: <https://www.sciencedirect.com/science/article/pii/S0019103507002709>
- [45] J. H. Waite, "Ion neutral mass spectrometer results from the first flyby of Titan," *Sci.*, vol. 308, no. 5724, pp. 982–986, may 2005. [Online]. Available: <https://science.sciencemag.org/content/308/5724/982>
- [46] M. L. Cable, S. M. Hörst, R. Hodyss, P. M. Beauchamp, M. A. Smith, and P. A. Willis, "Titan Tholins: Simulating Titan Organic Chemistry in the Cassini-Huygens Era," *Chem. Rev.*, vol. 112, no. 3, pp. 1882–1909, Mar. 2012. [Online]. Available: <https://doi.org/10.1021/cr200221x>
- [47] A. Ali, E. C. Sittler, Jr., D. Chornay, B. R. Rowe, and C. Puzzarini, "Organic chemistry in Titan's upper atmosphere and its astrobiological consequences: I. Views towards Cassini plasma spectrometer (CAPS) and ion neutral mass spectrometer (INMS) experiments in space," *Planet. Space Sci.*, vol. 109, pp. 46–63, MAY 2015. [Online]. Available: <https://doi.org/10.1016/j.pss.2015.01.015>
- [48] J. Cui, R. V. Yelle, V. Vuitton, J. H. Waite, W. T. Kasprzak, D. A. Gell, H. B. Niemann, I. C. Müller-Wodarg, N. Borggren, G. G. Fletcher, E. L. Patrick, E. Raaen, and B. A. Magee, "Analysis of Titan's neutral upper atmosphere from Cassini Ion Neutral Mass Spectrometer measurements," *Icarus*, vol. 200, no. 2, pp. 581–615, 2009. [Online]. Available: <http://dx.doi.org/10.1016/j.icarus.2008.12.005>
- [49] J. C. Loison, E. Hébrard, M. Dobrijevic, K. M. Hickson, F. Caralp, V. Hue, G. Gronoff, O. Venot, and Y. Bénilan, "The neutral photochemistry of nitriles,

- amines and imines in the atmosphere of Titan,” *Icarus*, vol. 247, pp. 218–247, 2015. [Online]. Available: <http://dx.doi.org/10.1016/j.icarus.2014.09.039>
- [50] S. M. Hörst, “Titan’s atmosphere and climate,” *J. Geophys. Res. E: Planets*, vol. 122, no. 3, pp. 432–482, 2017. [Online]. Available: <https://hal.archives-ouvertes.fr/tel-01925462v1/document>
- [51] H. Imanaka and M. A. Smith, “Formation of nitrogenated organic aerosols in the Titan upper atmosphere,” *Proc. Natl. Acad. Sci.*, vol. 107, no. 28, pp. 12 423–12 428, 2010. [Online]. Available: <https://www.pnas.org/doi/abs/10.1073/pnas.0913353107>
- [52] L. J. Allamandola, A. G. G. M. Tielens, and J. R. Barker, “Interstellar Polycyclic Aromatic Hydrocarbons: The Infrared Emission Bands, the Excitation/Emission Mechanism, and the Astrophysical Implications,” *Astro. J. Supp. Ser.*, vol. 71, p. 733, Dec. 1989. [Online]. Available: <https://ui.adsabs.harvard.edu/abs/1989ApJS...71..733A/abstract>
- [53] D. B. Rap, J. G. M. Schrauwen, A. N. Marimuthu, B. Redlich, and S. Brünken, “Low-temperature nitrogen-bearing polycyclic aromatic hydrocarbon formation routes validated by infrared spectroscopy,” *Nat. Astron.*, vol. 6, no. 9, pp. 1059–1067, 2022. [Online]. Available: <https://doi.org/10.1038/s41550-022-01713-z>
- [54] Peeters, E., Hony, S., Van Kerckhoven, C., Tielens, A. G. G. M., Allamandola, L. J., Hudgins, D. M., and Bauschlicher, C. W., “The rich 6 to 9 μm spectrum of interstellar PAHs,” *Astron. Astrophys.*, vol. 390, no. 3, pp. 1089–1113, 2002. [Online]. Available: <https://doi.org/10.1051/0004-6361:20020773>
- [55] C. M. Canelo, A. C. S. Friaça, D. A. Sales, M. G. Pastoriza, and D. Ruschel-Dutra, “Variations in the 6.2 μm emission profile in starburst-dominated galaxies: a signature of polycyclic aromatic nitrogen heterocycles (PANHs)?” *Mon. Not. R. Astron. Soc.*, vol. 475, no. 3, pp. 3746–3763, 01 2018. [Online]. Available: <https://doi.org/10.1093/mnras/stx3351>

- [56] A. Vats, A. Pathak, T. Onaka, M. Buragohain, I. Sakon, and I. Endo, “Theoretical study of infrared spectra of interstellar PAH molecules with N, NH, and NH₂ incorporation,” *Publ. Astron. Soc. Jpn.*, vol. 74, no. 1, pp. 161–174, 12 2021. [Online]. Available: <https://doi.org/10.1093/pasj/psab116>
- [57] A. Ricca, C. Boersma, and E. Peeters, “The 6.2 μm PAH Feature and the Role of Nitrogen: Revisited,” *Astrophys. J.*, vol. 923, no. 2, p. 202, dec 2021. [Online]. Available: <https://doi.org/10.3847/1538-4357/ac28fc>
- [58] C. Boersma, C. W. Bauschlicher, A. Ricca, A. L. Mattioda, J. Cami, E. Peeters, F. S. de Armas, G. P. Saborido, D. M. Hudgins, and L. J. Allamandola, “The NASA AMES PAH IR Spectroscopic Database Version 2.00: Updated Content, Web Site, and On(Off)line Tools,” *Astrophys. J. Suppl. Ser.*, vol. 211, no. 1, p. 8, feb 2014. [Online]. Available: <https://doi.org/10.1088/0067-0049/211/1/8>
- [59] C. Boersma, J. D. Bregman, and L. J. Allamandola, “Properties of Polycyclic Aromatic Hydrocarbons in the Northwest Photon Dominated Region of NGC 7023. I. PAH Size, Charge, Composition, and Structure Distribution,” *Astrophys. J.*, vol. 769, no. 2, p. 117, may 2013. [Online]. Available: <https://doi.org/10.1088/0004-637x/769/2/117>
- [60] J. M. Hayes, “Organic constituents of meteorites—a review,” *Geochim. Cosmochim. Acta*, vol. 31, no. 9, pp. 1395–1440, 1967. [Online]. Available: [https://doi.org/10.1016/0016-7037\(67\)90019-1](https://doi.org/10.1016/0016-7037(67)90019-1)
- [61] Z. Martins, “The nitrogen heterocycle content of meteorites and their significance for the origin of life,” *Life (Basel)*, vol. 8, no. 3, p. 28, jul 2018. [Online]. Available: <http://www.mdpi.com/2075-1729/8/3/28>
- [62] A. S. Burton, J. C. Stern, J. E. Elsila, D. P. Glavin, and J. P. Dworkin, “Understanding prebiotic chemistry through the analysis of extraterrestrial amino acids and nucleobases in meteorites,” *Chem. Soc. Rev.*, vol. 41, pp. 5459–5472, 2012. [Online]. Available: <http://dx.doi.org/10.1039/C2CS35109A>

- [63] Z. Martins, O. Botta, M. L. Fogel, M. A. Sephton, D. P. Glavin, J. S. Watson, J. P. Dworkin, A. W. Schwartz, and P. Ehrenfreund, “Extraterrestrial nucleobases in the Murchison meteorite,” *Earth Planet. Sci. Lett.*, vol. 270, no. 1-2, pp. 130–136, jun 2008. [Online]. Available: <https://www.sciencedirect.com/science/article/pii/S0012821X08001866?via=ihub>
- [64] K. Lodders, “Solar System Abundances and Condensation Temperatures of the Elements,” *Astrophys. J.*, vol. 591, no. 2, pp. 1220–1247, jul 2003. [Online]. Available: <https://doi.org/10.1086/375492>
- [65] S. Pizzarello, G. Cooper, and G. Flynn, *The nature and distribution of the organic material in carbonaceous chondrites and interplanetary dust particles*, Jul. 2006, pp. 625–652.
- [66] J. R. Cronin, S. Pizzarello, S. Epstein, and R. V. Krishnamurthy, “Molecular and isotopic analyses of the hydroxy acids, dicarboxylic acids, and hydroxydicarboxylic acids of the Murchison meteorite,” *Geochim. Cosmochim. Acta*, vol. 57, no. 19, pp. 4745–4752, oct 1993. [Online]. Available: <http://linkinghub.elsevier.com/retrieve/pii/0016703793901975>
- [67] J. C. Aponte, D. Whitaker, M. W. Powner, J. E. Elsila, and J. P. Dworkin, “Analyses of aliphatic aldehydes and ketones in carbonaceous chondrites,” *ACS Earth Space Chem.*, vol. 3, no. 3, pp. 463–472, 2019. [Online]. Available: <https://pubs.acs.org/doi/full/10.1021/acsearthspacechem.9b00006>
- [68] J. Hertzog, H. Naraoka, and P. Schmitt-Kopplin, “Profiling murchison soluble organic matter for new organic compounds with APPI- and ESI-FT-ICR MS,” *Life (Basel)*, vol. 9, no. 2, pp. 1–14, 2019. [Online]. Available: <https://www.mdpi.com/2075-1729/9/2/48>
- [69] Y. Huang, Y. Wang, M. R. Alexandre, T. Lee, C. Rose-Petruck, M. Fuller, and S. Pizzarello, “Molecular and compound-specific isotopic characterization

- of monocarboxylic acids in carbonaceous meteorites,” *Geochim. Cosmochim. Acta*, vol. 69, no. 4, pp. 1073–1084, 2005. [Online]. Available: <https://ui.adsabs.harvard.edu/abs/2005GeCoA..69.1073H/abstract>
- [70] O. Botta and J. L. Bada, “Extraterrestrial organic compounds in meteorites,” *Surv. Geophys.*, vol. 23, no. 5, pp. 411–467, 2002. [Online]. Available: <https://doi.org/10.1023/A:1020139302770>
- [71] M. P. Callahan, K. E. Smith, H. J. Cleaves, J. Ruzicka, J. C. Stern, D. P. Glavin, C. H. House, and J. P. Dworkin, “Carbonaceous meteorites contain a wide range of extraterrestrial nucleobases,” *Proc. Natl. Acad. Sci.*, vol. 108, no. 34, pp. 13 995–13 998, 2011. [Online]. Available: <https://www.pnas.org/doi/abs/10.1073/pnas.1106493108>
- [72] J. E. Elsila, J. C. Aponte, D. G. Blackmond, A. S. Burton, J. P. Dworkin, and D. P. Glavin, “Meteoritic Amino Acids: Diversity in Compositions Reflects Parent Body Histories,” *ACS Cent. Sci.*, vol. 2, no. 6, pp. 370–379, Jun. 2016. [Online]. Available: <https://doi.org/10.1021/acscentsci.6b00074>
- [73] H. Naraoka, M. Hashiguchi, Y. Sato, and K. Hamase, “New applications of high-resolution analytical methods to study trace organic compounds in extraterrestrial materials,” *Life (Basel)*, vol. 9, no. 3, 2019. [Online]. Available: <https://www.mdpi.com/2075-1729/9/3/62>
- [74] T. Nakamura, M. Matsumoto, K. Amano, Y. Enokido, M. E. Zolensky, T. Mikouchi, H. Genda, S. Tanaka, M. Y. Zolotov, K. Kurosawa, S. Wakita, R. Hyodo, H. Nagano, D. Nakashima, Y. Takahashi, Y. Fujioka, M. Kikui, E. Kagawa, M. Matsuoka, A. J. Brearley, A. Tsuchiyama, M. Uesugi, J. Matsuno, Y. Kimura, M. Sato, R. E. Milliken, E. Tatsumi, S. Sugita, T. Hiroi, K. Kitazato, D. Brownlee, D. J. Joswiak, M. Takahashi, K. Ninomiya, T. Takahashi, T. Osawa, K. Terada, F. E. Brenker, B. J. Tkalcec, L. Vincze, R. Brunetto, A. Aléon-Toppani, Q. H. S. Chan, M. Roskosz, J.-C. Viennet, P. Beck, E. E. Alp, T. Michikami, Y. Nagaashi,

T. Tsuji, Y. Ino, J. Martinez, J. Han, A. Dolocan, R. J. Bodnar, M. Tanaka, H. Yoshida, K. Sugiyama, A. J. King, K. Fukushi, H. Suga, S. Yamashita, T. Kawai, K. Inoue, A. Nakato, T. Noguchi, F. Vilas, A. R. Hendrix, C. Jaramillo-Correa, D. L. Domingue, G. Dominguez, Z. Gainsforth, C. Engrand, J. Duprat, S. S. Russell, E. Bonato, C. Ma, T. Kawamoto, T. Wada, S. Watanabe, R. Endo, S. Enju, L. Riu, S. Rubino, P. Tack, S. Takeshita, Y. Takeichi, A. Takeuchi, A. Takigawa, D. Takir, T. Tanigaki, A. Taniguchi, K. Tsukamoto, T. Yagi, S. Yamada, K. Yamamoto, Y. Yamashita, M. Yasutake, K. Uesugi, I. Umegaki, I. Chiu, T. Ishizaki, S. Okumura, E. Palomba, C. Pilorget, S. M. Potin, A. Alasli, S. Anada, Y. Araki, N. Sakatani, C. Schultz, O. Sekizawa, S. D. Sitzman, K. Sugiura, M. Sun, E. Dartois, E. D. Pauw, Z. Dionnet, Z. Djouadi, G. Falkenberg, R. Fujita, T. Fukuma, I. R. Gearba, K. Hagiya, M. Y. Hu, T. Kato, T. Kawamura, M. Kimura, M. K. Kubo, F. Langenhorst, C. Lantz, B. Lavina, M. Lindner, J. Zhao, B. Vekemans, D. Baklouti, B. Bazi, F. Borondics, S. Nagasawa, G. Nishiyama, K. Nitta, J. Mathurin, T. Matsumoto, I. Mitsukawa, H. Miura, A. Miyake, Y. Miyake, H. Yurimoto, R. Okazaki, H. Yabuta, H. Naraoka, K. Sakamoto, S. Tachibana, H. C. Connolly, D. S. Lauretta, M. Yoshitake, M. Yoshikawa, K. Yoshikawa, K. Yoshihara, Y. Yokota, K. Yogata, H. Yano, Y. Yamamoto, D. Yamamoto, M. Yamada, T. Yamada, T. Yada, K. Wada, T. Usui, R. Tsukizaki, F. Terui, H. Takeuchi, Y. Takei, A. Iwamae, H. Soejima, K. Shirai, Y. Shimaki, H. Senshu, H. Sawada, T. Saiki, M. Ozaki, G. Ono, T. Okada, N. Ogawa, K. Ogawa, R. Noguchi, H. Noda, M. Nishimura, N. Namiki, S. Nakazawa, T. Morota, A. Miyazaki, A. Miura, Y. Mimasu, K. Matsumoto, K. Kumagai, T. Kouyama, S. Kikuchi, K. Kawahara, S. Kameda, T. Iwata, Y. Ishihara, M. Ishiguro, H. Ikeda, S. Hosoda, R. Honda, C. Honda, Y. Hitomi, N. Hirata, N. Hirata, T. Hayashi, M. Hayakawa, K. Hatakeda, S. Furuya, R. Fukai, A. Fujii, Y. Cho, M. Arakawa, M. Abe, S. Watanabe, and Y. Tsuda, “Formation and evolution of carbonaceous asteroid Ryugu: Direct evidence from returned samples,” *Sci.*, vol. 0, no. 0, p. eabn8671, 2022. [Online]. Available:

<https://www.science.org/doi/abs/10.1126/science.abn8671>

- [75] Müller, Holger S. P., Walters, Adam, Wehres, Nadine, Belloche, Arnaud, Wilkins, Olivia H., Liu, Delong, Vicente, Rémi, Garrod, Robin T., Menten, Karl M., Lewen, Frank, and Schlemmer, Stephan, “Laboratory spectroscopic study and astronomical detection of vibrationally excited n-propyl cyanide,” *Astron. Astrophys.*, vol. 595, p. A87, 2016. [Online]. Available: <https://doi.org/10.1051/0004-6361/201629309>
- [76] Haykal, I., Carvajal, M., Tercero, B., Kleiner, I., López, A., Cernicharo, J., Motiyenko, R. A., Huet, T. R., Guillemin, J. C., and Margulès, L., “THz spectroscopy and first ISM detection of excited torsional states of ¹³C-methyl formate,” *Astron. Astrophys.*, vol. 568, p. A58, 2014. [Online]. Available: <https://doi.org/10.1051/0004-6361/201322937>
- [77] “Splatalogue,” 2022. [Online]. Available: <https://splatalogue.online/>
- [78] C. Puzzarini, J. F. Stanton, and J. Gauss, “Quantum-chemical calculation of spectroscopic parameters for rotational spectroscopy,” *Int. Rev. Phys. Chem.*, vol. 29, no. 2, pp. 273–367, apr 2010. [Online]. Available: <https://doi.org/10.1080/01442351003643401>
- [79] C. Puzzarini, “Rotational spectroscopy meets theory,” *Phys. Chem. Chem. Phys.*, vol. 15, pp. 6595–6607, 2013. [Online]. Available: <http://dx.doi.org/10.1039/C3CP44301A>
- [80] C. Puzzarini, M. Heckert, and J. Gauss, “The accuracy of rotational constants predicted by high-level quantum-chemical calculations. i. molecules containing first-row atoms,” *J. Chem. Phys.*, vol. 128, no. 19, p. 194108, 2008. [Online]. Available: <https://doi.org/10.1063/1.2912941>
- [81] J. F. Stanton, J. Gauss, L. Cheng, M. E. Harding, D. A. Matthews, and P. G. Szalay, “CFOUR, Coupled-Cluster techniques for Computational Chemistry,

- a quantum-chemical program package,” With contributions from A. Asthana, A.A. Auer, R.J. Bartlett, U. Benedikt, C. Berger, D.E. Bernholdt, S. Blaschke, Y. J. Bomble, S. Burger, O. Christiansen, D. Datta, F. Engel, R. Faber, J. Greiner, M. Heckert, O. Heun, M. Hilgenberg, C. Huber, T.-C. Jagau, D. Jonsson, J. Jusélius, T. Kirsch, M.-P. Kitsaras, K. Klein, G.M. Kopper, W.J. Lauderdale, F. Lipparini, J. Liu, T. Metzroth, L.A. Mück, D.P. O’Neill, T. Nottoli, J. Oswald, D.R. Price, E. Prochnow, C. Puzzarini, K. Ruud, F. Schiffmann, W. Schwalbach, C. Simmons, S. Stopkowicz, A. Tajti, J. Vázquez, F. Wang, J.D. Watts, C. Zhang, X. Zheng, and the integral packages MOLECULE (J. Almlöf and P.R. Taylor), PROPS (P.R. Taylor), ABACUS (T. Helgaker, H.J. Aa. Jensen, P. Jørgensen, and J. Olsen), and ECP routines by A. V. Mitin and C. van Wüllen. For the current version, see <http://www.cfour.de>. [Online]. Available: <http://www.cfour.de>
- [82] “SPFIT/SPCAT,” 2022. [Online]. Available: <http://www.ifpan.edu.pl/~kisiel/asym/pickett/crib.htm>
- [83] “PGOPHER, a program for rotational, vibrational and electronic spectra,” 2022. [Online]. Available: <http://pgopher.chm.bris.ac.uk/index.html>
- [84] K. L. K. Lee and M. McCarthy, “Bayesian Analysis of Theoretical Rotational Constants from Low-Cost Electronic Structure Methods,” *J. Phys. Chem. A*, vol. 124, no. 5, pp. 898–910, Feb. 2020. [Online]. Available: <https://doi.org/10.1021/acs.jpca.9b09982>
- [85] D. Agbaglo and R. C. Fortenberry, “The performance of explicitly correlated methods for the computation of anharmonic vibrational frequencies,” *Int. J. Quantum Chem.*, vol. 119, no. 11, p. e25899, 2019. [Online]. Available: <https://onlinelibrary.wiley.com/doi/abs/10.1002/qua.25899>
- [86] A. G. Watrous, B. R. Westbrook, M. C. Davis, and R. C. Fortenberry, “Vibrational and rotational spectral data for possible interstellar detection of AlH_3OH_2 , SiH_3OH ,

- and SiH_3NH_2 ,” *Mon. Not. R. Astron Soc.*, vol. 508, no. 2, pp. 2613–2619, 09 2021. [Online]. Available: <https://doi.org/10.1093/mnras/stab2683>
- [87] M. Heckert, M. Kállay, D. P. Tew, W. Klopper, and J. Gauss, “Basis-set extrapolation techniques for the accurate calculation of molecular equilibrium geometries using coupled-cluster theory,” *J. Chem. Phys.*, vol. 125, no. 4, p. 044108, 2006. [Online]. Available: <https://doi.org/10.1063/1.2217732>
- [88] D. E. Woon and T. H. Dunning, “Gaussian basis sets for use in correlated molecular calculations. V. Core-valence basis sets for boron through neon,” *J. Chem. Phys.*, vol. 90, no. 2, pp. 1007–1023, 1988. [Online]. Available: <https://doi.org/10.1063/1.470645>
- [89] J. Almlöf and P. R. Taylor, “Atomic natural orbital (ANO) basis sets for quantum chemical calculations,” *Adv. Quantum Chem.*, vol. 22, no. C, pp. 301–373, 1991. [Online]. Available: [https://doi.org/10.1016/S0065-3276\(08\)60366-4](https://doi.org/10.1016/S0065-3276(08)60366-4)
- [90] P.-O. Widmark, P.-r. Malmqvist, and B. O. Roos, “Density matrix averaged atomic natural orbital (ANO) basis set for correlated molecular wave functions,” *Theoretica chimica acta*, vol. 77, no. 5, pp. 291–306, 1990. [Online]. Available: <https://doi.org/10.1007/BF01120130>
- [91] M. Biczysko, J. Bloino, and C. Puzzarini, “Computational challenges in Astrochemistry,” *WIREs Comput. Mol. Sci.*, vol. 8, no. 3, p. e1349, 2018. [Online]. Available: <https://wires.onlinelibrary.wiley.com/doi/abs/10.1002/wcms.1349>
- [92] V. Barone, M. Biczysko, J. Bloino, and C. Puzzarini, “Accurate structure, thermodynamic and spectroscopic parameters from CC and CC/DFT schemes: the challenge of the conformational equilibrium in glycine,” *Phys. Chem. Chem. Phys.*, vol. 15, pp. 10 094–10 111, 2013. [Online]. Available: <http://dx.doi.org/10.1039/C3CP50439E>

- [93] M. Heckert, M. Kállay, and J. Gauss, “Molecular equilibrium geometries based on coupled-cluster calculations including quadruple excitations,” *Mol. Phys.*, vol. 103, no. 15-16, pp. 2109–2115, 2005. [Online]. Available: <https://doi.org/10.1080/00268970500083416>
- [94] A. M. Rosnik and W. F. Polik, “VPT2+K spectroscopic constants and matrix elements of the transformed vibrational Hamiltonian of a polyatomic molecule with resonances using Van Vleck perturbation theory,” *Mol. Phys.*, vol. 112, no. 2, pp. 261–300, 2014. [Online]. Available: <https://doi.org/10.1080/00268976.2013.808386>
- [95] J. K. G. Watson, “Determination of Centrifugal Distortion Coefficients of Asymmetric-Top Molecules. III. Sextic Coefficients,” *J. Chem. Phys.*, vol. 48, no. 10, pp. 4517–4524, 1967. [Online]. Available: <https://doi.org/10.1063/1.1668020>
- [96] G. Tarczay, P. G. Szalay, and J. Gauss, “First-principles calculation of electron spin-rotation tensors,” *J. Phys. Chem. A*, vol. 114, no. 34, pp. 9246–9252, 2010. [Online]. Available: <https://pubs.acs.org/doi/10.1021/jp103789x>
- [97] J. K. G. Watson, “Simplification of the molecular vibration-rotation hamiltonian,” *Mol. Phys.*, vol. 15, no. 5, pp. 479–490, 1968. [Online]. Available: <https://doi.org/10.1080/00268976800101381>
- [98] G. O. Sørensen, L. Mahler, and N. Rastrup-Andersen, “Microwave spectra of ^{15}N and ^{13}C pyridines, quadrupole coupling constants, dipole moment, and molecular structure of pyridines,” *Chemischer Informationsdienst*, vol. 5, no. 21, pp. 119–26, 1974. [Online]. Available: <https://onlinelibrary.wiley.com/doi/abs/10.1002/chin.197421081>
- [99] P. R. Franke, J. F. Stanton, and G. E. Douberly, “How to VPT2: Accurate and intuitive simulations of CH stretching infrared spectra using VPT2+K with large effective hamiltonian resonance treatments,” *J. Phys. Chem. A*, vol. 125, no. 6, pp. 1301–1324, 2021. [Online]. Available: <https://pubs.acs.org/doi/full/10.1021/acs.jpca.0c09526>

- [100] W. Gordy and R. L. Cook, *Microwave Molecular Spectra*, ser. Chemical applications of spectroscopy. Interscience Pub., 1970. [Online]. Available: https://books.google.com/books?id=_BF2xwEACAAJ
- [101] A. Duerden, F. E. Marshall, N. Moon, C. Swanson, K. M. Donnell, and G. Grubbs II, "A chirped pulse Fourier transform microwave spectrometer with multi-antenna detection," *J. Mol. Spectrosc.*, vol. 376, p. 111396, 2021. [Online]. Available: <https://www.sciencedirect.com/science/article/pii/S0022285220301648>
- [102] United States National Bureau of Standards, "Publications of the National Bureau of Standards," 1948. [Online]. Available: <https://search.library.wisc.edu/catalog/999632283402121>
- [103] W. E. Good, "The Inversion Spectrum of Ammonia," *Phys. Rev.*, vol. 69, pp. 539–539, May 1946. [Online]. Available: <https://link.aps.org/doi/10.1103/PhysRev.69.539>
- [104] G. G. Brown, B. C. Dian, K. O. Douglass, S. M. Geyer, S. T. Shipman, and B. H. Pate, "A broadband Fourier transform microwave spectrometer based on chirped pulse excitation," *Rev. Sci. Instrum.*, vol. 79, 2008. [Online]. Available: <https://aip.scitation.org/doi/10.1063/1.2919120>
- [105] D. Schmitz, V. Alvin Shubert, T. Betz, and M. Schnell, "Multi-resonance effects within a single chirp in broadband rotational spectroscopy: The rapid adiabatic passage regime for benzonitrile," *J. Mol. Spectrosc.*, vol. 280, pp. 77–84, 2012, broadband Rotational Spectroscopy. [Online]. Available: <https://www.sciencedirect.com/science/article/pii/S0022285212001488>
- [106] C. Abeysekera, B. Joalland, N. Ariyasingha, L. N. Zack, I. R. Sims, R. W. Field, and A. G. Suits, "Product branching in the low temperature reaction of CN with propyne by chirped-pulse microwave spectroscopy in a uniform supersonic flow," *J. Phys. Chem. Lett.*, vol. 6, no. 9, pp. 1599–1604, 2015, PMID: 26263320. [Online]. Available: <https://doi.org/10.1021/acs.jpcclett.5b00519>

- [107] T. J. Johnson, P. M. Aker, N. K. Scharko, and S. D. Williams, “Quantitative infrared and near-infrared gas-phase spectra for pyridine: Absolute intensities and vibrational assignments,” *J. Quant. Spectrosc. Radiat. Transfer*, vol. 206, pp. 355–366, 2018. [Online]. Available: <https://www.sciencedirect.com/science/article/pii/S0022407317306283>
- [108] R. D. Suenram, F. J. Lovas, W. Pereyra, G. T. Fraser, and A. R. H. Walker, “Rotational Spectra, Structure, and Electric Dipole Moments of Methyl and Ethyltert-Butyl Ether (MTBE and ETBE),” *J. Mol. Spectrosc.*, vol. 181, no. 1, pp. 67–77, 1997. [Online]. Available: <https://www.sciencedirect.com/science/article/pii/S0022285296971556>
- [109] D. Lide, R. Suenram, D. Johnson, and F. Lovas, “Evolution of Microwave Spectroscopy at the National Bureau of Standards (NBS) and the National Institute of Standards and Technology (NIST),” 2012-09-28 00:09:00 2012. [Online]. Available: https://tsapps.nist.gov/publication/get_pdf.cfm?pub_id=911001
- [110] T. Shouyuan, X. Zhining, F. Yujie, and G. Qian, “Applications and Techniques of Microwave Spectroscopy,” *Prog. Chem.*, vol. 21, no. 5, pp. 1060–1069, MAY 2009. [Online]. Available: <https://manu56.magtech.com.cn/progchem/EN/Y2009/V21/I05/1060>
- [111] L. Li, M. Sun, X.-H. Li, Z.-W. Zhao, H.-M. Ma, H.-Y. Gan, Z.-H. Lin, S.-C. Shi, and L. M. Ziurys, “Recent Advances on Rotational Spectroscopy and Microwave Spectroscopic Techniques,” *Chinese J. Anal. Chem.*, vol. 42, no. 9, pp. 1369–1378, 2014. [Online]. Available: <https://www.sciencedirect.com/science/article/pii/S1872204014607672>
- [112] A. Kraśnicki and Z. Kisiel, “Electric dipole moments of acrylonitrile and of propionitrile measured in supersonic expansion,” *J. Mol. Spectrosc.*, vol. 270, no. 1, pp. 83–87, 2011. [Online]. Available: <https://www.sciencedirect.com/science/article/pii/S0022285211002013>

- [113] J. M. Brown, S. P. Beaton, and K. M. Evenson, “Rotational Frequencies of Transition Metal Hydrides for Astrophysical Searches in the Far-Infrared,” *Astrophys. J. Lett.*, vol. 414, p. L125, Sep. 1993. [Online]. Available: <https://adsabs.harvard.edu/full/1993ApJ...414L.125B>
- [114] A. L. Steber, J. L. Neill, D. P. Zaleski, B. H. Pate, A. Lesarri, R. G. Bird, V. Vaquero-Vara, and D. W. Pratt, “Structural studies of biomolecules in the gas phase by chirped-pulse Fourier transform microwave spectroscopy,” *Faraday Discuss.*, vol. 150, pp. 227–242, 2011. [Online]. Available: <http://dx.doi.org/10.1039/C1FD00008J>
- [115] J. J. Pajski, M. D. Logan, K. O. Douglas, G. G. Brown, B. C. Dian, B. H. Pate, and R. D. Suenram, “Chirped-pulse Fourier transform microwave spectroscopy: A new technique for rapid identification of chemical agents.” *Int. J. High Speed Electron. Syst.*, vol. 18, no. 01, pp. 31–45, 2008. [Online]. Available: <https://doi.org/10.1142/S0129156408005114>
- [116] D. Patterson and J. M. Doyle, “Cooling molecules in a cell for FTMW spectroscopy,” *Mol. Phys.*, vol. 110, no. 15-16, pp. 1757–1766, 2012. [Online]. Available: <https://doi.org/10.1080/00268976.2012.679632>
- [117] G. B. Park and R. W. Field, “Perspective: The first ten years of broadband chirped pulse Fourier transform microwave spectroscopy,” *J. Chem. Phys.*, vol. 144, 2016. [Online]. Available: <https://aip.scitation.org/doi/10.1063/1.4952762>
- [118] G. B. Park, A. H. Steeves, K. Kuyanov-Prozument, J. L. Neill, and R. W. Field, “Design and evaluation of a pulsed-jet chirped-pulse millimeter-wave spectrometer for the 70–102 GHz region,” *J. Chem. Phys.*, vol. 135, no. 2, p. 024202, 2011. [Online]. Available: <https://doi.org/10.1063/1.3597774>
- [119] J. C. Santos, A. B. Rocha, and R. R. Oliveira, “Rotational spectrum simulations of asymmetric tops in an astrochemical context.” *Jour. Mol. Model.*, vol. 26, p. 278, Sep 2020. [Online]. Available: <https://doi.org/10.1007/s00894-020-04523-0>

- [120] C. Puzzarini, “Astronomical complex organic molecules: Quantum chemistry meets rotational spectroscopy,” *Int. J. Quantum Chem.*, vol. 117, no. 2, pp. 129–138, 2017. [Online]. Available: <https://onlinelibrary.wiley.com/doi/abs/10.1002/qua.25284>
- [121] J. M. Hollis, F. J. Lovas, A. J. Remijan, P. R. Jewell, V. V. Ilyushin, and I. Kleiner, “Detection of Acetamide (CH_3CONH_2): The Largest Interstellar Molecule with a Peptide Bond,” *Astrophys. J.*, vol. 643, no. 1, pp. L25–L28, may 2006. [Online]. Available: <https://doi.org/10.1086/505110>
- [122] B. Tercero, I. Kleiner, J. Cernicharo, H. V. L. Nguyen, A. López, and G. M. M. Caro, “Discovery of Methyl Acetate and Gauche Ethyl Formate in Orion,” *Astrophys. J.*, vol. 770, no. 1, p. L13, may 2013. [Online]. Available: <https://doi.org/10.1088/2041-8205/770/1/l13>
- [123] A. Potapov, A. Canosa, E. Jiménez, and B. Rowe, “Uniform Supersonic Chemical Reactors: 30 Years of Astrochemical History and Future Challenges,” *Angewandte Chemie International Edition*, vol. 56, no. 30, pp. 8618–8640, 2017. [Online]. Available: <https://onlinelibrary.wiley.com/doi/abs/10.1002/anie.201611240>
- [124] I. W. M. Smith, “Laboratory Astrochemistry: Gas-Phase Processes,” *Annu. Rev. Astron. Astrophys.*, vol. 49, no. 1, pp. 29–66, 2011. [Online]. Available: <https://doi.org/10.1146/annurev-astro-081710-102533>
- [125] H. S. Müller, F. Schlöder, J. Stutzki, and G. Winnewisser, “The Cologne Database for Molecular Spectroscopy, CDMS: a useful tool for astronomers and spectroscopists,” *J. Mol. Struct.*, vol. 742, no. 1, pp. 215–227, 2005, molecular Spectroscopy and Structure. [Online]. Available: <https://www.sciencedirect.com/science/article/pii/S0022286005000888>
- [126] F. Coester, “Bound states of a many-particle system,” *Nucl. Phys.*, vol. 7, pp. 421–424, 1958. [Online]. Available: <https://www.sciencedirect.com/science/article/pii/0029558258902803>

- [127] F. Coester and H. Kümmel, “Short-range correlations in nuclear wave functions,” *Nucl. Phys.*, vol. 17, pp. 477–485, 1960. [Online]. Available: <https://www.sciencedirect.com/science/article/pii/0029558260901401>
- [128] J. Čížek, “Origins of coupled cluster technique for atoms and molecules,” *Theoretica chimica acta*, vol. 80, no. 2, pp. 91–94, 1991. [Online]. Available: <https://doi.org/10.1007/BF01119616>
- [129] T. Helgaker, J. Gauss, P. Jørgensen, and J. Olsen, “The prediction of molecular equilibrium structures by the standard electronic wave functions,” *J. Chem. Phys.*, vol. 106, no. 15, pp. 6430–6440, 1997. [Online]. Available: <https://doi.org/10.1063/1.473634>
- [130] K. L. Bak, J. Gauss, P. Jørgensen, J. Olsen, T. Helgaker, and J. F. Stanton, “The accurate determination of molecular equilibrium structures,” *J. Chem. Phys.*, vol. 114, pp. 6548–6556, 2001. [Online]. Available: <https://aip.scitation.org/doi/10.1063/1.1357225>
- [131] S. Coriani, D. Marchesan, J. Gauss, C. Hättig, T. Helgaker, and P. Jørgensen, “The accuracy of ab initio molecular geometries for systems containing second-row atoms.” *J. Chem. Phys.*, vol. 123, p. 184107, Nov 2005. [Online]. Available: <https://aip.scitation.org/doi/10.1063/1.2104387>
- [132] R. Pio, “Euler angle transformations,” *IEEE Transactions on Automatic Control*, vol. 11, no. 4, pp. 707–715, 1966.
- [133] P. R. Bunker and P. Jensen, *Molecular Symmetry and Spectroscopy*. NRC Research Press, 2012.
- [134] H. Meyer, “The Molecular Hamiltonian,” *Ann. Phys. Chem.*, vol. 53, no. 1, pp. 141–172, 2002, pMID: 11972005. [Online]. Available: <https://doi.org/10.1146/annurev.physchem.53.082201.124330>

- [135] J. K. G. Watson, "The vibration-rotation hamiltonian of linear molecules," *Mol. Phys.*, vol. 19, no. 4, pp. 465–487, Jan. 1970. [Online]. Available: <http://dx.doi.org/10.1080/00268977000101491>
- [136] C. W. David, "The Tensor of the Moment of Inertia," *Chem. Ed. Mat.*, p. 21, 2006. [Online]. Available: https://opencommons.uconn.edu/chem_educ/21
- [137] R. N. Zare, *Angular Momentum: Understanding Spatial Aspects in Chemistry and Physics*, 1st ed. Wiley-Interscience, 1998.
- [138] S. A. Cooke and P. Ohring, "Decoding Pure Rotational Molecular Spectra for Asymmetric Molecules," *J. Spec.*, p. 10, 2013. [Online]. Available: <https://www.hindawi.com/journals/jspec/2013/698392/>
- [139] C. H. Townes, *Microwave spectroscopy*. New York: Dover Publications, 1975 - 1955.
- [140] P. F. Bernath, *Spectra of atoms and molecules*. Oxford university press, 1995.
- [141] J. K. G. Watson, *Vibrational spectra and structure*. Amsterdam: Elsevier, 1977, vol. 6, no. 2. [Online]. Available: <https://www.sciencedirect.com/science/article/pii/0022286078870409>
- [142] A. L. L. East, W. D. Allen, and S. J. Klippenstein, "The anharmonic force field and equilibrium molecular structure of ketene," *J. Chem. Phys.*, vol. 102, no. 21, pp. 8506–8532, 1995. [Online]. Available: <https://doi.org/10.1063/1.468842>
- [143] I. C. Bowater, J. M. Brown, and A. Carrington, "Microwave Spectrum of the HCO Free Radical," *J. Chem. Phys.*, vol. 54, pp. 4957–4958, 1971. [Online]. Available: <https://aip.scitation.org/doi/10.1063/1.1674776>
- [144] J. M. Brown and T. J. Sears, "A reduced form of the spin-rotation Hamiltonian for asymmetric-top molecules, with applications to HO₂ and NH₂," *J. Mol. Spectrosc.*, vol. 75, no. 1, pp. 111–133, 1979. [Online]. Available: <https://www.sciencedirect.com/science/article/pii/002228527990153X>

- [145] J. Vázquez and J. F. Stanton, “Treatment of Fermi resonance effects on transition moments in vibrational perturbation theory,” *Mol. Phys.*, vol. 105, no. 1, pp. 101–109, 2007. [Online]. Available: <https://doi.org/10.1080/00268970601135784>
- [146] B. T. Darling and D. M. Dennison, “The water vapor molecule,” *Phys. Rev.*, vol. 57, pp. 128–139, 1940. [Online]. Available: <https://doi.org/10.1103/PhysRev.57.128>
- [147] D. A. Matthews, J. Vázquez, and J. F. Stanton, “Calculated stretching overtone levels and Darling–Dennison resonances in water: a triumph of simple theoretical approaches,” *Mol. Phys.*, vol. 105, no. 19–22, pp. 2659–2666, 2007. [Online]. Available: <https://doi.org/10.1080/00268970701618424>
- [148] D. A. Matthews and J. F. Stanton, “Quantitative analysis of Fermi resonances by harmonic derivatives of perturbation theory corrections,” *Mol. Phys.*, vol. 107, no. 3, pp. 213–222, 2009. [Online]. Available: <https://doi.org/10.1080/00268970902769463>
- [149] P. Glarborg, A. D. Jensen, and J. E. Johnsson, “Fuel nitrogen conversion in solid fuel fired systems,” *Prog. Energy Combust. Sci.*, vol. 29, no. 2, pp. 89–113, 2003. [Online]. Available: <https://www.sciencedirect.com/science/article/pii/S036012850200031X>
- [150] P. Glarborg, J. A. Miller, B. Ruscic, and S. J. Klippenstein, “Modeling nitrogen chemistry in combustion,” *Prog. Energy Combust. Sci.*, vol. 67, pp. 31–68, 2018. [Online]. Available: <https://www.sciencedirect.com/science/article/pii/S0360128517301600>
- [151] P. Burchill and L. S. Welch, “Variation of nitrogen content and functionality with rank for some UK bituminous coals,” *Fuel*, vol. 68, no. 1, pp. 100–104, 1989. [Online]. Available: <https://www.sciencedirect.com/science/article/pii/0016236189900197>
- [152] S. C. Hill and D. L. Smoot, “Modeling of nitrogen oxides formation and destruction in combustion systems,” *Prog. Energy Combust. Sci.*, vol. 26, no. 4, pp.

- 417–458, 2000. [Online]. Available: <https://www.sciencedirect.com/science/article/pii/S0360128500000113>
- [153] Z. Tian, Y. Li, T. Zhang, A. Zhu, and F. Qi, “Identification of combustion intermediates in low-pressure premixed pyridine/oxygen/argon flames,” *J. Phys. Chem. A.*, vol. 112, no. 51, pp. 13 549–13 555, 2008. [Online]. Available: <https://doi.org/10.1021/jp8066537>
- [154] L.-N. Wu, Z.-Y. Tian, J.-J. Weng, D. Yu, Y.-X. Liu, D.-X. Tian, C.-C. Cao, J.-B. Zou, Y. Zhang, and J.-Z. Yang, “Experimental and kinetic study on the low-temperature oxidation of pyridine as a representative of fuel-N compounds,” *Combust. Flame*, vol. 202, pp. 394–404, 2019. [Online]. Available: <https://www.sciencedirect.com/science/article/pii/S001021801930046X>
- [155] E. Ikeda, P. Nicholls, and J. C. Mackie, “A kinetic study of the oxidation of pyridine,” *Proc. Combust. Inst.*, vol. 28, no. 2, pp. 1709–1716, jan 2000. [Online]. Available: <https://www.sciencedirect.com/science/article/pii/S0082078400805718>
<https://linkinghub.elsevier.com/retrieve/pii/S0082078400805718>
- [156] J. C. Mackie, M. B. Colket, and P. F. Nelson, “Shock tube pyrolysis of pyridine,” *J. Phys. Chem.*, vol. 94, no. 10, pp. 4099–4106, may 1990. [Online]. Available: <https://pubs.acs.org/doi/10.1021/j100373a040>
- [157] H. U. R. Memon, K. D. Bartle, J. M. Taylor, and A. Williams, “The shock tube pyrolysis of pyridine,” *Int. J. Energy Res.*, vol. 24, no. 13, pp. 1141–1159, 2000. [Online]. Available: [https://doi.org/10.1002/1099-114X\(20001025\)24:13<1141::AID-ER653>3.0.CO;2-S](https://doi.org/10.1002/1099-114X(20001025)24:13<1141::AID-ER653>3.0.CO;2-S)
- [158] N. R. Hore and D. K. Russell, “Radical pathways in the thermal decomposition of pyridine and diazines: a laser pyrolysis and semi-empirical study,” *J. Chem. Soc., Perkin Trans. 2*, no. 2, pp. 269–276, 1998. [Online]. Available: <http://xlink.rsc.org/?DOI=a706731c>

- [159] Z.-C. Wang, C. A. Cole, N. J. Demarais, T. P. Snow, and V. M. Bierbaum, “Reactions of azine anions with nitrogen and oxygen atoms: implications for Titan’s upper atmosphere and interstellar chemistry.” *J. Am. Chem. Soc.*, vol. 137, no. 33, pp. 10 700–10 709, aug 2015. [Online]. Available: <https://pubs.acs.org/doi/10.1021/jacs.5b06089>
- [160] T. Onaka, “Unidentified infrared bands in the diffuse interstellar medium,” in *Astrophysics of Dust*, ser. Astronomical Society of the Pacific Conference Series, Estes Park, Colorado, May 26–30, 2003, May, witt, A. N. and Clayton, G. C. and Draine, B. T., Eds.; 2004. [Online]. Available: <https://ui.adsabs.harvard.edu/abs/2004ASPC..309..163O/abstract>
- [161] T. Pino, E. Dartois, A. T. Cao, Y. Carpentier, T. Chamaillé, R. Vasque, A. P. Jones, L. D’Hendecourt, and P. Bréchnignac, “The 6.2 μm band position in laboratory and astrophysical spectra: A tracer of the aliphatic to aromatic evolution of interstellar carbonaceous dust,” *Astron. Astrophys.*, vol. 490, no. 2, pp. 665–672, 2008. [Online]. Available: <https://ui.adsabs.harvard.edu/abs/2008A&A...490..665P/abstract>
- [162] H. Alvaro Galué, O. Pirali, and J. Oomens, “Gas-phase infrared spectra of cationized nitrogen-substituted polycyclic aromatic hydrocarbons,” *Astron. Astrophys.*, vol. 517, p. A15, 2010. [Online]. Available: <https://doi.org/10.1051/0004-6361/201014050>
- [163] A. M. Burkhardt, R. A. Loomis, C. N. Shingledecker, K. L. K. Lee, A. J. Remijan, M. C. McCarthy, and B. A. McGuire, “Ubiquitous aromatic carbon chemistry at the earliest stages of star formation,” *Nat. Astron.*, vol. 5, no. 2, pp. 181–187, Feb. 2021. [Online]. Available: <https://doi.org/10.1038/s41550-020-01253-4>
- [164] J. Hendrix, P. P. Bera, T. J. Lee, and M. Head-Gordon, “Cation, anion, and radical isomers of $\text{C}_4\text{H}_4\text{N}$: Computational characterization and implications for astrophysical and planetary environments,” *J. Phys. Chem. A*, vol. 124, no. 10, pp. 2001–2013, 2020. [Online]. Available: <https://pubs.acs.org/doi/full/10.1021/acs.jpca.9b11305>

- [165] S. M. Hörst, R. V. Yelle, A. Buch, N. Carrasco, G. Cernogora, O. Dutuit, E. Quirico, E. Sciamma-O'Brien, M. A. Smith, À. Somogyi, C. Szopa, R. Thissen, and V. Vuitton, "Formation of amino acids and nucleotide bases in a Titan atmosphere simulation experiment," *Astrobiology*, vol. 12, no. 9, pp. 809–817, 2012. [Online]. Available: <https://doi.org/10.1089/ast.2011.0623>
- [166] M. J. Abplanalp, R. Frigge, and R. I. Kaiser, "Low-temperature synthesis of polycyclic aromatic hydrocarbons in Titan's surface ices and on airless bodies," *Sci. Adv.*, vol. 5, no. 10, p. eaaw5841, oct 2019. [Online]. Available: <https://advances.sciencemag.org/lookup/doi/10.1126/sciadv.aaw5841>
- [167] S. Soorkia, C. A. Taatjes, D. L. Osborn, T. M. Selby, A. J. Trevitt, K. R. Wilson, and S. R. Leone, "Direct detection of pyridine formation by the reaction of CH (CD) with pyrrole: A ring expansion reaction," *Phys. Chem. Chem. Phys.*, vol. 12, no. 31, pp. 8750–8758, 2010. [Online]. Available: <https://pubmed.ncbi.nlm.nih.gov/20463997/>
- [168] R. L. Levy, M. A. Grayson, and C. J. Wolf, "The organic analysis of the murchison meteorite," *Geochim. Cosmochim. Acta*, vol. 37, no. 3, pp. 467–483, mar 1973. [Online]. Available: <http://www.sciencedirect.com/science/article/pii/0016703773902123>
- [169] M. H. Engel, S. A. Macko, and J. A. Silfer, "Carbon isotope composition of individual amino acids in the Murchison meteorite," *Nat.*, vol. 348, no. 6296, pp. 47–49, 1990. [Online]. Available: <https://www.nature.com/articles/348047a0>
- [170] Z. Peeters, O. Botta, S. B. Charnley, Z. Kisiel, Y.-J. Kuan, and P. Ehrenfreund, "Formation and photostability of N-heterocycles in space - I. The effect of nitrogen on the photostability of small aromatic molecules," *Astron. Astrophys.*, vol. 433, no. 2, pp. 583–590, 2005. [Online]. Available: <https://doi.org/10.1051/0004-6361:20042443>
- [171] G. Yuen, N. Blair, D. J. Des Marais, and S. Chang, "Carbon isotope composition of low molecular weight hydrocarbons and monocarboxylic acids from Murchison

- meteorite,” *Nat.*, vol. 307, no. 5948, pp. 252–254, 1984. [Online]. Available: <https://doi.org/10.1038/307252a0>
- [172] H. Carrascosa, C. González Díaz, G. M. Muñoz Caro, P. C. Gómez, and M. L. Sanz, “Synthesis of the first nitrogen-heterocycles in interstellar ice analogues containing methylamine (CH_3NH_2) exposed to UV radiation: formation of trimethylentriamine (TMT, $\text{c}-(\text{-CH}_2\text{-NH})_3$) and hexamethylentetramine (HMT, $(\text{CH}_2)_6\text{N}_4$),” *Mon. Not. R. Astron. Soc.*, vol. 506, no. 1, pp. 791–805, 2021. [Online]. Available: <https://doi.org/10.1093/mnras/stab1710>
- [173] P. Recio, D. Marchione, A. Caracciolo, V. J. Murray, L. Mancini, M. Rosi, P. Casavecchia, and N. Balucani, “A crossed molecular beam investigation of the $\text{N}(^2\text{D}) + \text{pyridine}$ reaction and implications for prebiotic chemistry,” *Chem. Phys. Lett.*, vol. 779, p. 138852, 2021. [Online]. Available: <https://www.sciencedirect.com/science/article/pii/S0009261421005352>
- [174] R. T. Garrod, S. L. W. Weaver, and E. Herbst, “Complex chemistry in star-forming regions: An expanded gas-grain warm-up chemical model,” *Astrophys. J.*, vol. 682, no. 1, pp. 283–302, jul 2008. [Online]. Available: <http://stacks.iop.org/0004-637X/682/i=1/a=283https://iopscience.iop.org/article/10.1086/588035>
- [175] L. Zhao, M. Prendergast, R. I. Kaiser, B. Xu, W. Lu, M. Ahmed, A. Hasan Howlader, S. F. Wnuk, A. S. Korotchenko, M. M. Evseev, E. K. Bashkirov, V. N. Azyazov, and A. M. Mebel, “A molecular beam and computational study on the barrierless gas phase formation of (iso)quinoline in low temperature extraterrestrial environments,” *Phys. Chem. Chem. Phys.*, vol. 23, pp. 18 495–18 505, 2021. [Online]. Available: <http://dx.doi.org/10.1039/D1CP02169A>
- [176] P. H. Kasai and D. McLeod, “Generation of pyridyl radicals by dissociative electron capture in argon matrices,” *J. Am. Chem. Soc.*, vol. 92, no. 20, pp. 6085–6086, 1970. [Online]. Available: <https://doi.org/10.1021/ja00723a059>

- [177] P. H. Kasai and D. J. McLeod, "Electron spin resonance study of heterocycles. i. pyridyl radicals," *J. Am. Chem. Soc.*, vol. 94, no. 3, pp. 720–727, Feb. 1972. [Online]. Available: <https://doi.org/10.1021/ja00758a007>
- [178] K. Tsuji, H. Yoshida, and K. Hayashi, "ESR study of irradiated pyridine," *J. Chem. Phys.*, vol. 45, no. 8, pp. 2894–2897, 1966. [Online]. Available: <https://doi.org/10.1063/1.1728043>
- [179] H. J. Bower, J. A. McRae, and M. C. R. Symons, "Unstable intermediates. Part LVI. An electron spin resonance study of the radicals formed by γ -irradiation of pyridine and some of its derivatives," *J. Chem. Soc. A*, pp. 2696–2699, 1968. [Online]. Available: <http://dx.doi.org/10.1039/J19680002696>
- [180] J. E. Bennett and B. Mile, "Electron spin resonance spectra of some σ -type aromatic radicals," *J. Phys. Chem.*, vol. 75, no. 22, pp. 3432–3437, 1971. [Online]. Available: <https://pubs.acs.org/doi/10.1021/j100691a005>
- [181] K. Sakaguchi and K. Inuzuka, "Properties of phenyl radical and pyridyl radicals in ground-state," *Nippon Kagaku Kaishi*, vol. 1976, no. 9, pp. 1343–1348, 1976.
- [182] O. Kikuchi, Y. Hondo, K. Morihashi, and M. Nakayama, "An ab initio molecular orbital study of pyridyl radicals," *Bull. Chem. Soc. Jpn.*, vol. 61, no. 1, pp. 291–292, 1988. [Online]. Available: <https://doi.org/10.1246/bcsj.61.291>
- [183] X. Cheng, L. Niu, Y. Zhao, and Z. Zhou, "Vibrational analysis for multi-channel decomposition reactions of *o*-pyridyl radical based on DFT methods," *Spectrochim. Acta, Part A*, vol. 60, no. 4, pp. 907–914, mar 2004. [Online]. Available: <https://linkinghub.elsevier.com/retrieve/pii/S1386142503003184>
- [184] M. Lucas, J. Minor, J. Zhang, and C. Brazier, "Ultraviolet photodissociation dynamics of the *o*-pyridyl radical," *J. Phys. Chem. A*, vol. 117, no. 46, pp. 12 138–12 145, nov 2013. [Online]. Available: <https://pubs.acs.org/doi/10.1021/jp4057237>

- [185] X. Cheng, Y. Y. Zhao, and Z. Y. Zhou, “Theoretical studies on *p*-pyridyl radical decomposition reactions,” *J. Mol. Struct. THEOCHEM*, vol. 678, no. 1-3, pp. 17–21, jun 2004. [Online]. Available: <https://linkinghub.elsevier.com/retrieve/pii/S016612800400137X>
- [186] M. Lucas, J. Minor, J. Zhang, and C. Brazier, “H-atom dissociation channels in ultraviolet photochemistry of *m*-pyridyl radical,” *Chin. J. Chem. Phys.*, vol. 27, no. 6, p. 621, 2014. [Online]. Available: <https://doi.org/10.1063/1674-0068/27/06/621-627>
- [187] X. Cheng, “Reaction mechanism of decomposition system of *m*-pyridyl radical: A theoretical investigation,” *J. Mol. Struct. THEOCHEM*, vol. 731, no. 1-3, pp. 89–99, oct 2005. [Online]. Available: <https://linkinghub.elsevier.com/retrieve/pii/S0166128005005889>
- [188] A. Korte, A. Mardyukov, and W. Sander, “Pyridyl- and pyridylperoxy radicals – a matrix isolation study,” *Aust. J. Chem.*, vol. 67, pp. 1324–1329, 2014. [Online]. Available: <https://www.publish.csiro.au/ch/CH14149>
- [189] J. A. Devine, M. C. Babin, K. Blackford, and D. M. Neumark, “High-resolution photoelectron spectroscopy of the pyridinide isomers,” *J. Chem. Phys.*, vol. 151, no. 6, p. 064302, 2019. [Online]. Available: <https://doi.org/10.1063/1.5115413>
- [190] D. A. Matthews, L. Cheng, M. E. Harding, F. Lipparini, S. Stopkowicz, T.-C. Jagau, P. G. Szalay, J. Gauss, and J. F. Stanton, “Coupled-cluster techniques for computational chemistry: The CFOUR program package,” *J. Chem. Phys.*, vol. 152, no. 21, p. 214108, 2020. [Online]. Available: <https://doi.org/10.1063/5.0004837>
- [191] J. Gauss and J. F. Stanton, “Analytic CCSD(T) second derivatives,” *Chem. Phys. Lett.*, vol. 276, no. 1-2, pp. 70–77, 1997. [Online]. Available: [https://doi.org/10.1016/S0009-2614\(97\)88036-0](https://doi.org/10.1016/S0009-2614(97)88036-0)

- [192] H. M. Pickett, "The fitting and prediction of vibration-rotation spectra with spin interactions," *J. Mol. Spectrosc.*, vol. 148, no. 2, pp. 371–377, 1991. [Online]. Available: <https://www.sciencedirect.com/science/article/pii/002228529190393O>
- [193] C. Sah, L. Jacob, M. Saraswat, and S. Venkataramani, "Does a nitrogen lone pair lead to two centered–three electron (2c–3e) interactions in pyridyl radical isomers?" *J. Phys. Chem. A*, vol. 121, no. 19, pp. 3781–3791, may 2017. [Online]. Available: <http://pubs.acs.org/doi/10.1021/acs.jpca.7b01501>
- [194] F. Mata, M. J. Quintana, and G. O. Sørensen, "Microwave spectra of pyridine and monodeuterated pyridines. Revised molecular structure of pyridine," *J. Mol. Struct.*, vol. 42, no. C, pp. 1–5, dec 1977. [Online]. Available: <https://linkinghub.elsevier.com/retrieve/pii/002228607787021X>
- [195] S. A. Peebles and R. A. Peebles, "Determination of the heavy atom structure of bromobenzene by rotational spectroscopy," *J. Mol. Struct.*, vol. 657, no. 1, pp. 107–116, 2003. [Online]. Available: <https://www.sciencedirect.com/science/article/pii/S0022286003003909>
- [196] G. O. Sørensen, "Centrifugal distortion analysis of microwave spectra of asymmetric top molecules. the microwave spectrum of pyridine," *J. Mol. Spectrosc.*, vol. 22, no. 1, pp. 325–346, 1967. [Online]. Available: <https://www.sciencedirect.com/science/article/pii/0022285267901798>
- [197] L. Liang and V. A. Rassolov, "Fermi contact spin density calculations of aromatic radicals," *J. Phys. Chem. C*, vol. 114, no. 48, pp. 20 648–20 658, 2010. [Online]. Available: <https://doi.org/10.1021/jp105511a>
- [198] J. A. Pople, D. L. Beveridge, and P. A. Dobosh, "Approximate self-consistent molecular-orbital theory. V. Intermediate neglect of differential overlap," *J. Chem. Phys.*, vol. 47, no. 6, pp. 2026–2033, 1967. [Online]. Available: <https://doi.org/10.1063/1.1712233>

- [199] J. M. L. Martin, T. J. Lee, P. R. Taylor, and J. François, “The anharmonic force field of ethylene, C₂H₄, by means of accurate ab initio calculations,” *J. Chem. Phys.*, vol. 103, no. 7, pp. 2589–2602, 1995. [Online]. Available: <https://doi.org/10.1063/1.469681>
- [200] J. I. Steinfeld, *Laser and coherence spectroscopy*. Plenum Press New York, 1978.
- [201] F. Bloch, “Nuclear induction,” *Physica*, vol. 17, no. 3, pp. 272–281, 1951. [Online]. Available: <https://www.sciencedirect.com/science/article/pii/0031891451900687>
- [202] J. P. Porterfield, L. Satterthwaite, S. Eibenberger, D. Patterson, and M. C. McCarthy, “High sensitivity microwave spectroscopy in a cryogenic buffer gas cell,” *Rev. Sci. Instrum.*, vol. 90, no. 5, p. 053104, 2019. [Online]. Available: <https://doi.org/10.1063/1.5091773>
- [203] F. J. Lovas and R. D. Suenram, “Pulsed beam Fourier transform microwave measurements on OCS and rare gas complexes of OCS with Ne, Ar, and Kr,” *J. Chem. Phys.*, vol. 87, no. 4, pp. 2010–2020, 1987. [Online]. Available: <https://doi.org/10.1063/1.453176>
- [204] M. Patel, J. Thomas, and H. C. Joshi, “Flow characterization of supersonic gas jets: Experiments and simulations,” *J. Vac.*, vol. 192, p. 110440, oct 2021. [Online]. Available: <https://doi.org/10.1016%2Fj.vacuum.2021.110440>
- [205] H. Beijerinck, R. Van Gerwen, E. Kerstel, J. Martens, E. Van Vliembergen, M. Smits, and G. Kaashoek, “Campargue-type supersonic beam sources: Absolute intensities, skimmer transmission and scaling laws for mono-atomic gases He, Ne and Ar,” *Chem. Phys.*, vol. 96, no. 1, pp. 153–173, 1985. [Online]. Available: <https://www.sciencedirect.com/science/article/pii/0301010485802019>
- [206] F. Sherman, “Technical report: Fluid mechanics 6-90-63-61,” *Lockheed Missiles and Space Co., Sunnyvale, California*, 1963.

- [207] R. M. Gurusinghe, N. Dias, R. Krueger, and A. G. Suits, “Uniform supersonic flow sampling for detection by chirped-pulse rotational spectroscopy,” *J. Chem. Phys.*, vol. 156, no. 1, p. 014202, 2022. [Online]. Available: <https://doi.org/10.1063/5.0073527>
- [208] M. Gaveau, D. Boscher, and J. Martin, “Shape and width of IR absorption lines across supersonic free jets,” *Chem. Phys. Lett.*, vol. 107, no. 1, pp. 31–34, 1984. [Online]. Available: <https://www.sciencedirect.com/science/article/pii/0009261484853506>
- [209] B. M. Hays, T. Guillaume, T. Hearne, I. R. Cooke, D. Gupta, O. Abdelkader Khedaoui, S. D. Le Picard, and I. R. Sims, “Design and performance of an E-band chirped pulse spectrometer for kinetics applications OCS – He pressure broadening,” *J. Quant. Spec. Rad. Trans.*, vol. 250, p. 107001, Jul. 2020. [Online]. Available: <https://hal-univ-rennes1.archives-ouvertes.fr/hal-02638438>
- [210] T. J. Ronningen and F. C. De Lucia, “Helium induced pressure broadening and shifting of HCN hyperfine transitions between 1.3 and 20 K,” *J. Chem. Phys.*, vol. 122, no. 18, p. 184319, 2005. [Online]. Available: <https://doi.org/10.1063/1.1895905>
- [211] C. D. Ball, M. Mengel, F. C. De Lucia, and D. E. Woon, “Quantum scattering calculations for H₂S–He between 1–600 K in comparison with pressure broadening, shift, and time resolved double resonance experiments,” *J. Chem. Phys.*, vol. 111, no. 19, pp. 8893–8903, 1999. [Online]. Available: <https://doi.org/10.1063/1.480234>
- [212] J. L. Neill, B. J. Harris, A. L. Steber, K. O. Douglass, D. F. Plusquellic, and B. H. Pate, “Segmented chirped-pulse Fourier transform submillimeter spectroscopy for broadband gas analysis,” *Opt. Express*, vol. 21, no. 17, pp. 19 743–19 749, Aug 2013. [Online]. Available: <http://opg.optica.org/oe/abstract.cfm?URI=oe-21-17-19743>
- [213] M. Fatima, C. Pérez, B. E. Arenas, M. Schnell, and A. L. Steber, “Benchmarking a new segmented K-band chirped-pulse microwave spectrometer and its application to the conformationally rich amino alcohol isoleucinol,” *Phys. Chem. Chem. Phys.*, vol. 22, pp. 17 042–17 051, 2020. [Online]. Available: <http://dx.doi.org/10.1039/D0CP01141J>

- [214] I. A. Finneran, D. B. Holland, P. B. Carroll, and G. A. Blake, “A direct digital synthesis chirped pulse Fourier transform microwave spectrometer,” *Rev. Sci. Instrum.*, vol. 84, no. 8, p. 083104, 2013. [Online]. Available: <https://doi.org/10.1063/1.4818137>
- [215] L. Zou, R. A. Motiyenko, L. Margulès, and E. A. Alekseev, “Millimeter-wave emission spectrometer based on direct digital synthesis,” *Rev. Sci. Instrum.*, vol. 91, p. 063104, 2020. [Online]. Available: <https://doi.org/10.1063/5.0004461>
- [216] (2022, Oct.) Everything RF. Raghav Kapur. RF. [Online]. Available: <https://www.everythingrf.com/products/microwave-rf-amplifiers/rf-lambda/567-89-rflupa0618ga>
- [217] (2022, Oct.) Spectrum Instrumentation. 401 Hackensack Ave, 4th Floor, Hackensack, NJ 07601, USA. [Online]. Available: http://www.applsys.com/pulse_twt.html
- [218] (2022, Oct.) Applied Systems Engineering, Inc. 7510 Benbrook Parkway, Fort Worth, TX 76126. [Online]. Available: <http://www.applsys.com/contact.html>
- [219] (2022, Oct.) Tektronix. 14150 SW Karl Braun Drive, P.O. Box 500 Beaverton, OR 97077, USA. [Online]. Available: <https://www.tek.com/en/products/arbitrary-waveform-generators>
- [220] (2013) Analog devices, inc. [Online]. Available: http://www.analog.com/static/imported-files/data_sheets/AD9914.pdf
- [221] Y. Hou, C. Li, and S. Tang, “An Accurate DDS Method Using Compound Frequency Tuning Word and Its FPGA Implementation,” *Electronics*, vol. 7, no. 11, 2018. [Online]. Available: <https://www.mdpi.com/2079-9292/7/11/330>
- [222] E. Murphy and C. Slattery, “Ask the application engineer-33: All about direct digital synthesis,” *Analogue Dialogue*, vol. 38-08, Aug. 2004. [Online]. Available: <https://www.analog.com/en/analog-dialogue/articles/all-about-direct-digital-synthesis.html>
- [223] “Department of Labor Logo United States Department of Labor,” 2022-22-21 00:09:00 2022. [Online]. Available: <https://www.osha.gov/chemicaldata/119>

- [224] Z. Kisiel, L. Pszczółkowski, B. J. Drouin, C. S. Brauer, S. Yu, J. C. Pearson, I. R. Medvedev, S. Fortman, and C. Neese, “Broadband rotational spectroscopy of acrylonitrile: Vibrational energies from perturbations,” *J. Mol. Spectrosc.*, vol. 280, pp. 134–144, 2012, broadband Rotational Spectroscopy. [Online]. Available: <https://www.sciencedirect.com/science/article/pii/S0022285212001038>
- [225] “Department of Labor Logo United States Department of Labor,” 2022-22-21 00:09:00 2022. [Online]. Available: <https://www.osha.gov/chemicaldata/57>
- [226] D. Proch and T. Trickl, “A high-intensity multi-purpose piezoelectric pulsed molecular beam source,” *Rev. Sci. Instrum.*, vol. 60, no. 4, pp. 713–716, 1989. [Online]. Available: <https://doi.org/10.1063/1.1141006>
- [227] R. D. Nelson Jr, D. R. Lide Jr, and A. A. Maryott, “Selected values of electric dipole moments for molecules in the gas phase,” National Standard Reference Data System, Tech. Rep., 1967.
- [228] E. Ye, R. P. Bettens, F. C. De Lucia, D. T. Petkie, and S. Albert, “Millimeter and submillimeter wave rotational spectrum of pyridine in the ground and excited vibrational states,” *J. Mol. Spectrosc.*, vol. 232, no. 1, pp. 61–65, 2005. [Online]. Available: <https://www.sciencedirect.com/science/article/pii/S0022285205000378>
- [229] A. Maris, L. B. Favero, R. Danieli, P. G. Favero, and W. Caminati, “Vibrational relaxation in pyridine upon supersonic expansion,” *J. Chem. Phys.*, vol. 113, no. 19, pp. 8567–8573, 2000. [Online]. Available: <https://doi.org/10.1063/1.1318224>
- [230] M. J. Fadden and C. M. Hadad, “Rearrangement pathways of arylperoxy radicals. I. The azabenzenes,” *J. Phys. Chem. A*, vol. 104, no. 25, pp. 6088–6094, jun 2000. [Online]. Available: <https://pubs.acs.org/doi/10.1021/jp0008492>